Technical Physics Letters, Vol. 26, No. 10, 2000, pp. 849–850. Translated from Pis'ma v Zhurnal Tekhnicheskoĭ Fiziki, Vol. 26, No. 19, 2000, pp. 1–5.

Low-Frequency Dielectric Relaxation in 5TsB Liquid Crystals Controlled by the Ion Adsorption–Desorption Processes

A. V. Koval'chuk

Institute of Physics, National Academy of Sciences of Ukraine, Kiev, Ukraine
e-mail: akoval@iop.kiev.ua
Received January 28, 2000

Abstract—Stable liquid-crystalline states with various ε' and ρ values were obtained in planar-oriented 5TsB liquid crystals by exposure to constant and alternating electric fields. The initial portion of the low-frequency dispersion of ε' and ε" obeys the Debye equation for both strictly planar and nonplanar ("oblique") orientation of molecules. *© 2000 MAIK "Nauka/Interperiodica".*

It was demonstrated [1–4] that measurements of the frequency dependence (dispersion) of ε' and ε" of weak electrolytes (liquid crystals [1–3], glycerol [4], immersion oil [5]) in a low-frequency range ($f < 10$ Hz) offer an effective means for investigating the parameters and structure of electric double layers. In most cases, the initial portion of the low-frequency dispersion of ε' and ε" can be approximated by the Debye equation in the Cole–Cole modification.

Previously [1], we showed for the first time that the initial portion of the low-frequency dispersion of ε' and ε" in a liquid-crystalline ZhK 1282 mixture with planar orientation obeys the Debye equation. Our subsequent investigations confirmed that this dispersion law is observed only in nematic liquid crystals with planar orientation. However, it was still unclear whether the low-frequency dispersion of ε' and ε" obeying the Debye equation will be observed in samples with an orientation deviating from strictly planar.

The purpose of this work was to find a means of controlling the orientation of molecules relative to the electrode surface and to study the effect of orientation on the parameters characterizing the initial portion of the low-frequency dispersion of ε' and ε". The measurements were performed on 5TsB samples using an experimental setup and procedures similar to those described in [1, 2].

Our previous experiments [4, 6] showed that prolonged (above 1 h) exposure of the immersion oil [6] or glycerol [4, 6] to a constant or alternating electric field transforms the samples into a new stable state with a higher or lower conductivity. It was suggested that the transition is related to the adsorption and/or desorption of ions in the near-electrode region. In liquid crystals, the ion adsorption or desorption may affect both the conductivity and the orientation of molecules.

Table 1 gives the designation of and describes the conditions for the obtaining of states with different conductivities and molecular orientations. Note that the states of the system (except for state 0) are not strictly "fixed", each state does not reflect a specific internal structure of a sample. The parameters of state are characterized by the type and duration of the external action.

Table 2 lists the values of ε', the specific resistance ρ, and the parameters characterizing the initial portion of the dispersion of ε' and ε". The measurements of ε' and ρ were performed at a sufficiently high frequency

Table 1. Conditions for the obtaining of states with various ρ and ε' values in 5TsB samples

State	Voltage type	*U*, V	*T*, K	Exposure time, h
0		0	295	4
1	ac (100 Hz)	2.5	330	2
2	dc	14	295	3
3	dc	14	330	1

Table 2. The values of ρ, ε', and the parameters characterizing the initial portion of the low-frequency dispersion of ε' and ε" for 5TsB samples in various states ($d = 40$ μm; $T = 295$ K)

State	ε_∞	$\rho \times 10^{-7}$, Ω m	τ, s	ε_s	*W*, μm
0	7.2	1.71			
1	5.2	1.36	0.26	2270	0.21
2	6.6	1.93	0.36	2210	0.28
3	10	2.90	0.54	2220	0.42

1063-7850/00/2610-0849$20.00

($f > 100$ Hz) where the low-frequency dispersion was not manifested. The thickness W of a near-electrode layer featuring relaxation processes described by the Debye equation was determined by the equation [1–6]

$$W = 2d\frac{\varepsilon_\infty}{\varepsilon_s}, \quad (1)$$

where d is the sample thickness and ε_∞ and ε_s are the dielectric permittivities for $f = \infty$ and 0, respectively ($\varepsilon_\infty = \varepsilon'$ in the frequency interval free of dispersion).

As seen from Table 2, the transition from state 0 to 1 is accompanied by a decrease in both ε' and ρ. Note that in the latter state $\varepsilon' = \varepsilon_\perp$, while all the subsequent transitions induced by the alternating field lead to an increase in both ε' and ρ.

The time variation of ρ (curve *1*) and ε' (curve *2*) during and upon exposure of the samples to the external field (the switch-off time indicated by the vertical arrow) is depicted in the figure. As seen from these data, the application of the field leads to a more than tenfold increase in the ρ value (at maximum). When the field is switched off, ρ drops to a certain stationary level (about 2.3 times that in state 1). The irreversibility is more pronounced for the ε' value.

The increase in ρ and ε' values in states 2 and 3 can be explained by the adsorption of ions on the electrode surface. As seen from the kinetic data (figure), the amount of ions adsorbed during the field application is greater than that retained upon relaxation into state 3. A large reversible component in the kinetic of ρ confirms the hypothesis that changes in the ρ and ε' values under the action of various external factors are actually related to the adsorption and desorption of ions.

As seen from the obtained data, the initial portion of the low-frequency dispersion of ε' and ε'' in all states of the sample obeys the Debye equation

$$\varepsilon^* = \varepsilon_\infty + \frac{\varepsilon_s - \varepsilon_\infty}{1 + i\omega\tau}, \quad (2)$$

where ε^* is the complex permittivity, $\omega = 2\pi f$ is the circular frequency, and τ is the dielectric relaxation time. This result leads to a very important conclusion that the low-frequency dispersion of ε' and ε'' described by the Debye equation is observed for both strictly planar and nonplanar ("oblique") orientation of molecules.

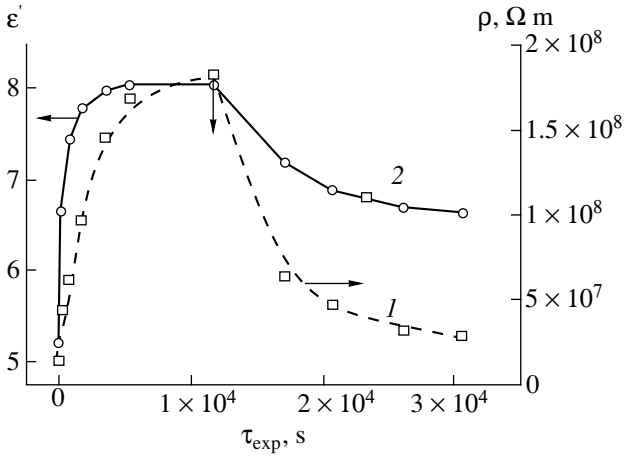

The kinetics of ρ (curve *1*) and ε' (curve *2*) for the transition from state 1 to 2 in a 40-μm-thick 5TsB sample at T = 295 K.

The data in Table 2 indicate that τ is proportional to ρ and that the W value increases with ρ. It is important to note that W increases at the expense of ε_∞ characterizing the dielectric permittivity averaged over the sample thickness. Actually, Eq. (1) must contain the value of permittivity in the near-surface region. In a strongly inhomogeneous structure (especially in state 3), the value of permittivity near the electrode may significantly differ from ε_∞.

Acknowledgments. The work was supported by the STCU grant no. 637.

REFERENCES

1. O. V. Koval'chuk, Ukr. Fiz. Zh. **41** (10), 991 (1996).
2. O. V. Koval'chuk, Ukr. Fiz. Zh. **41** (11/12), 1093 (1996).
3. Shuichi Murakami, Hironori Iga, and Hiroyoshi Naito, J. Appl. Phys. **80** (11), 396 (1996).
4. A. V. Koval'chuk, J. Chem. Phys. **108** (5), 8190 (1998).
5. O. V. Koval'chuk, Ukr. Fiz. Zh. **44** (11), 1376 (1999).
6. A. V. Koval'chuk, Funct. Mater. **5** (3), 426 (1998).

Translated by P. Pozdeev

Technical Physics Letters, Vol. 26, No. 10, 2000, pp. 851–853. Translated from Pis'ma v Zhurnal Tekhnicheskoĭ Fiziki, Vol. 26, No. 19, 2000, pp. 6–9.

A New Method of Layer Deposition

S. G. Psakh'e, K. P. Zol'nikov, and T. Yu. Uvarov

Institute of Strength Physics and Materials Science, Siberian Division, Russian Academy of Sciences, Tomsk, 634055 Russia

Received March 27, 2000

Abstract—A new approach to layer-by-layer film deposition is developed based on the data of molecular dynamics modeling. The proposed deposition method makes use of a nonlinear pulse interaction with a free material (source) surface. It is shown that, provided the pulse amplitude is sufficiently large, an atomic plane is detached from the surface. Impinging on a target (substrate), the detached plane forms a monolayer coating. Combining various source materials, it is possible to obtain multilayer films with complicated compositions and structures. © *2000 MAIK "Nauka/Interperiodica".*

Investigation of the behavior of various materials under the action of high-energy pulses showed that nonlinear waves, including solitary compression pulses (SCPs) [1–6], may form in crystals. The SCP properties are much like those of solitons: SCPs represent nonlinear plane waves with a wavelength on the order of a few lattice constants. In a defect-free crystal, these waves propagate without energy dissipation and retain both shape and amplitude. It was demonstrated that interaction of an SCP with a free crystallite surface leads to stretching of the near-surface region, after which either the SCP is reflected from this surface back to the bulk

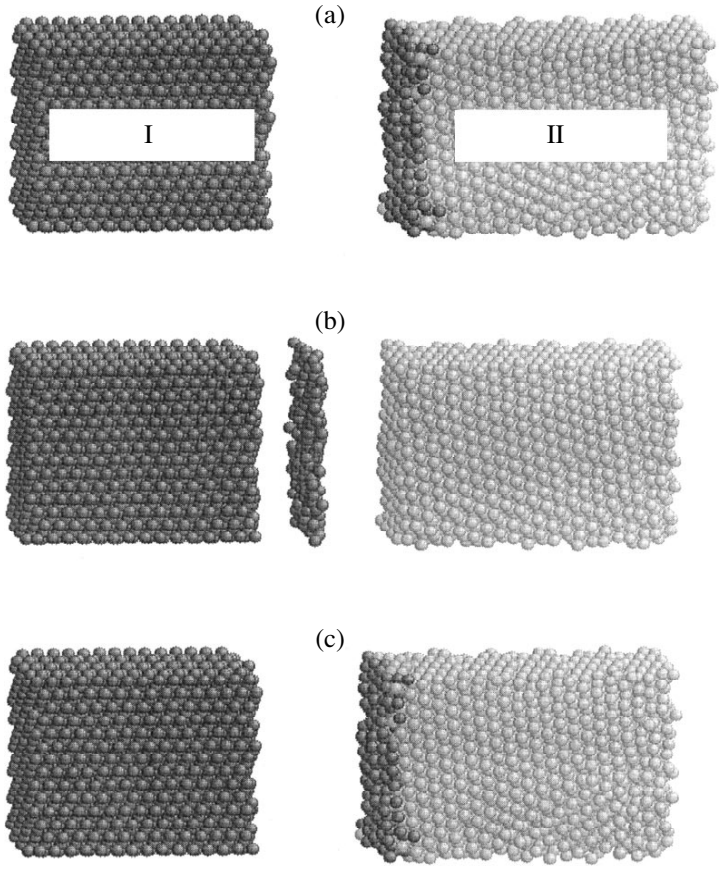

Fig. 1. Schematic diagrams illustrating the model system: (a) initial state; (b) detachment of a monolayer fragment from the rear surface of crystallite I; (c) monolayer deposit on crystallite II.

1063-7850/00/2610-0851$20.00 © 2000 MAIK "Nauka/Interperiodica"

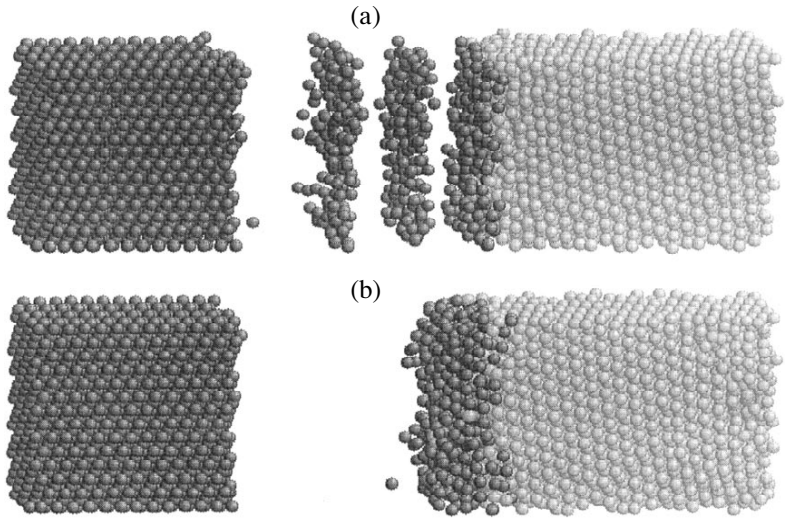

Fig. 2. Schematic diagrams illustrating (a) sequential detachment of three monolayer fragments from the rear surface of crystallite I and (b) the final structure of a deposit formed on crystallite II upon collisions with the three fragments.

or the near-surface layers detach to move away at a velocity reaching up to several km/s. Because of a small wavelength corresponding to SCPs, the detached fragment may have a thickness from one to a few atomic monolayers (interplanar spacings).

The purpose of this work was to theoretically study the possibility of using the previously described effect of nanoscopic layer detachment for the development of a new approach to the deposition of complex thin-layer coatings.

The calculations were performed using a molecular dynamics formalism described previously [7, 8], based on the atomic interaction potentials determined within the framework of the embedded atom method [9, 10]. The model comprised two copper crystallites (I and II) having the same total cross section but different crystallographic orientations (Fig. 1a), each crystallite containing more than 3000 atoms. The SCPs with an amplitude of 2600 m/s were generated in crystallite I by the scheme proposed in [7]. The amplitude was selected so as to satisfy the condition of SCP-induced fragment detachment from the rear surface of crystallite I (Fig. 1b).

The results of our calculations showed that a collision between the detached fragment and the free surface of crystallite II results in the SCP generation. Upon termination of the corresponding relaxation processes, the region of crystallite II in contact with the impinging fragment almost completely restores the initial crystal structure with the deposited layer built into the target crystallite (Fig. 1c).

The process character significantly changes when a packet of three or more SCPs is generated in the source (crystallite I) so that the time period between collisions of the detached fragments with the target are shorter than the characteristic time of the relaxation processes in crystallite II. Figure 2a shows the modeled system with three fragments detached from crystallite I sequentially striking crystallite II. As seen from Fig. 2b, a structure formed in the near-surface region of the target differs significantly from the initial structure of crystallite II and contains a large number of vacancy complexes and other structural defects. The structure of the layer deposited was found to depend on the time interval between the target collisions with impinging fragments.

Based on the results of our model calculations, it is concluded that the effect of nanoscopic layer detachment induced by the interaction of nonlinear pulses with the free material surface may serve a base for the new method of multilayer film deposition. It should be noted that technological parameters of the process, such as the pulse amplitude, interval between pulses, angle of incidence, etc., may be evaluated using the molecular dynamics modeling techniques. The proposed method opens the way to form multilayer sandwich films with a preset order of the component layers. This is achieved by using preliminarily selected source (dopant) materials corresponding to the preset structure.

REFERENCES

1. M. Toda, *Theory of Non-Linear Lattices* (Springer-Verlag, Heidelberg, 1981; Mir, Moscow, 1984).
2. B. L. Holian and G. K. Straub, Phys. Rev. **18** (4), 1593 (1978).
3. J. Batteh and J. Powell, J. Appl. Phys. **49** (7), 3933 (1978).

4. S. G. Psakh'e, K. P. Zol'nikov, and S. Yu. Korostelev, Pis'ma Zh. Tekh. Fiz. **21** (13), 1 (1995) [Tech. Phys. Lett. **21**, 489 (1995)].
5. S. G. Psakh'e, K. P. Zol'nikov, and D. Yu. Saraev, Pis'ma Zh. Tekh. Fiz. **24** (3), 42 (1998) [Tech. Phys. Lett. **24**, 99 (1998)].
6. S. G. Psakh'e, K. P. Zol'nikov, R. I. Kadyrov, *et al.*, Pis'ma Zh. Tekh. Fiz. **25** (6), 7 (1999) [Tech. Phys. Lett. **25**, 209 (1999)].
7. S. G. Psakh'e, K. P. Zol'nikov, R. I. Kadyrov, *et al.*, Fiz. Goreniya Vzryva **35** (4), 106 (1999).
8. K. P. Zol'nikov, T. Yu. Uvarov, A. G. Lipnitskiĭ, *et al.*, Pis'ma Zh. Tekh. Fiz. **25** (23), 22 (1999) [Tech. Phys. Lett. **25**, 936 (1999)].
9. A. V. Berch, A. G. Lipnitskiĭ, and E. V. Chulkov, Poverkhnost', No. 6, 23 (1994).
10. S. V. Eremeev, A. G. Lipnitskiĭ, A. I. Potekaev, and E. V. Chulkov, Phys. Low-Dimens. Semicond. Struct., No. 3/4, 127 (1997).

Translated by P. Pozdeev

Technical Physics Letters, Vol. 26, No. 10, 2000, pp. 854–856. Translated from Pis'ma v Zhurnal Tekhnicheskoĭ Fiziki, Vol. 26, No. 19, 2000, pp. 10–15.

A Self-Excited Hydromagnetic Dynamo Effect Can Take Place in Astrobleme Impact Melts

A. I. Grigor'ev

Yaroslavl State University, Yaroslavl, Russia

e-mail: grig@uniar.ao.ru

Received March 7, 2000

Abstract—A self-excited hydromagnetic dynamo effect may take place in the lake of an impact melt with a volume on the order of a hundred cubic kilometers and a temperature of 2000–3000 K formed upon collision of a large meteorite (or asteroid) with a planet. The high temperature results in large electric conductivity and low viscosity of the medium. This circumstance provides explanation for the magnetic anomalies related to the Earth astroblemes. © *2000 MAIK "Nauka/Interperiodica".*

The collision of a large meteorite (or an asteroid) with the surface of the Earth or another planet results in the formation of a depression (astrobleme) in the region of collision. The depression has a diameter from a few kilometers to several hundreds of kilometers, depending on the cosmic body size and velocity, and is partly filled with a high-temperature impact melt comprising a mixture of the asteroid substance and the planet's rock at the impact site [1–3]. The velocities of large meteorites striking the Earth fall within the range from the second cosmic velocity ($\approx 1.1 \times 10^4$ m/s) up to 10^5 m/s (a maximum velocity relative to the Earth possible at this distance from the sun).

For example, the Puchezh-Katunkskaya astrobleme (Nizhniĭ Novgorod region), having a diameter of about 80 km, could have been formed, according to estimates made in [2], upon a collision of the Earth and an asteroid with a diameter of ~4 km and a velocity of $\approx 2.5 \times 10^4$ km/s. The resulting strong shockwave led to the formation of an impact melt with a volume of ≈590 km^3, of which about two-thirds remained in the impact crater. The molten lava, having a tendency to fill the dips, formed a lake in the crater. Assuming that dips account for about one-tenth of the crater area, the thickness H of the molten lava layer in the Puchezh-Katunkskaya astrobleme can be estimated at ≈0.8 km.

According to the petrographic estimates [4], the impact melt temperature may reach up to T = 2800–3300 K. The lifetime of the impact melt in the liquid state, with the melt volume amounting to hundreds of cubic kilometers and the cooling proceeding by heat exchange through the lava lake surface (for certainty, this surface can be considered as covered with a layer of boiling water and, hence, occurring at a constant temperature), was evaluated as ten thousand years [2]. This estimate is obviously overstated. However, even assuming that the heat is removed from the lava lake surface by the radiative mechanism and obeys the law $\sim\varepsilon T^4$ (ε is the Stefan–Boltzmann constant), the characteristic time of cooling down to a temperature of rock melting ($T_* \approx 1100$ K) will be on the order of several years.

Thus, the impact crater contains for a long period of time a large volume of high-temperature impact melt at the bottom. The dynamic viscosity of liquids η increases with the temperature according an exponential law [5]:

$$\eta = \eta_0 \exp(E_0/kT), \quad (1)$$

where E_0 is a constant that can be approximately determined as the melting heat divided by the Avogadro number, k is the Boltzmann constant, and the factor η_0 has the dimensionality of viscosity and a characteristic value on the order of a typical gas viscosity at the corresponding temperature [5]. Taking into account that $E_0 \sim 1$ eV for most oxides entering into the composition of rocks [6], we will assume in the following estimates that the impact melt viscosity satisfies the relationship (1) with $\eta_0 = 10^{-2}$ Pa s and $E_0 = 1$ eV. This approximation yields the impact melt viscosity values in agreement with the results of measurements of the properties of molten silicate magmas, the viscosity of which amounts to ~1 Pa s at $T \approx 1900$–2100 K [7].

Low values of the impact melt viscosity at high temperature gradients developed in the lava lake favor intensive convective motions in the impact melt. Alekseev and Gusev [8] showed that the order of magnitude of the velocity of convective flows in liquids can be estimated using the relationship

$$U \sim 0.25(\gamma f d/2\eta)^{1/2}, \quad (2)$$

where γ is the efficiency of energy conversion from mechanical (convective motions) to thermal, f is the thermal energy flux density in the molten lava, and d is a characteristic linear scale of the convective motions.

1063-7850/00/2610-0854$20.00

According to [8], the efficiency of conversion of the thermal energy into the mechanical work of convection weakly depends on the special features of heat supply to a system and can be estimated for most of the natural processes as $\gamma \sim 0.1$. The thermal flux f can be evaluated using the Fourier law by introducing an effective thermal conductivity coefficient λ_* taking into account the convective heat transfer. The λ_* value is approximately two orders of magnitude higher than the molecular thermal conductivity [9]:

$$|\mathbf{f}| \approx \lambda_* |\nabla T| \sim \lambda_* \Delta T/(0.5H). \quad (3)$$

The rocks are known to behave as strongly compensated semiconductors with an electric conductivity of the mixed type, which implies the presence of both donor and acceptor impurities at nearly equal concentrations [10]. The conductivity activation energies do not exceed one electronvolt [10]. For comparison, a pure aluminum oxide Al_2O_3 contained in large amounts in the rocks has a bandgap width exceeding 5 eV; however, these data refer to solid rocks. On meting and subsequent heating, the electric conductivity of semiconductors increases by the exponential law [11]:

$$\sigma = \sigma_* \exp(-E_*/kT), \quad (4)$$

where E_* is the activation energy, k is the Boltzmann constant, T is the absolute temperature, and σ_* is a constant characterizing the electric conductivity at infinite temperatures (for various semiconductors, this factor falls within 10^5–10^7 S/m). The activation energy depends on the particular mechanism of conductivity (in noncrystalline semiconductors, several competitive conductivity mechanism may be operative) and varies from a few tenths to several electronvolts [11]. At a sufficiently high temperature ($T \approx 2000$–3000 K), the conductivity of semiconductors becomes comparable with that of liquid metals. For the subsequent estimates, we will assume that σ of the impact melt at $T \approx 2000$–3000 K obeys the relationship (4) with $\sigma_* = 10^7$ S/m and $E_* = 1$ eV.

The conditions (temperatures, electric conductivity, viscosity, convective flow rates) established in the impact lava lake with a characteristic linear size on the order of kilometers allow for the realization of the self-excited hydromagnetic dynamo effect. According to the modern cosmological concepts [12, 13], this effect accounts for the existence of magnetic fields of planets and stars. As a result, the impact lava lake occurring at the center of any large astrobleme would possess a magnetic field of its own. A criterion for the possible realization of the self-excited hydromagnetic dynamo effect in a conducting medium is as follows [12, 13]:

$$\mathrm{Re}_m = \mu_0 \sigma H U \geq 10, \quad (5)$$

where Re_m is the magnetic Reynolds number and μ_0 is the magnetic constant.

Taking into account relationships (1)–(4), condition (5) can be written as

$$\mathrm{Re}_m = 0.125\mu_0\sigma_* H\left(\frac{\gamma\lambda_*\Delta T}{2\eta_0}\right)^{1/2} \times \exp\left(-\frac{E_0 + 0.5E_*}{kT}\right) \geq 10. \quad (6)$$

Upon substituting $\lambda_* \approx 250$ W/(m K), $H = 800$ m, and $\Delta T \sim T = 2000$–3000 K into this expression, we may conclude that condition (5) holds, leaving a wide margin (several orders of magnitude) that may partly compensate for a rather arbitrary selection of the transfer coefficients and constants in the approximated relationships (justified by the lack of data on the properties of impact melt).

A seeding magnetic field necessary for realization of the self-excited hydromagnetic dynamo effect may be provided by the Earth's magnetic field. The lifetime of the source of magnetic field in an astrobleme is determined by the time of the lava lake cooling down to a temperature level where the temperature- and viscosity-dependent electric conductivity and the velocity of convective motions in the lava would decrease so that condition (5) ceases to hold. According to a rough estimate obtained assuming that the impact lava represents a spherical body irradiating heat by the Stefan–Boltzmann law, the characteristic time of the lava lake cooling exceeds one year. In fact, the characteristic time of lava cooling to a temperature at which condition (5) fails to be valid ($T \approx 1500$ K) will be greater by one–two orders of magnitude. However, even one year is sufficient for the intrinsic self-excited hydromagnetic dynamo operative in an impact lava lake to magnetize up to a maximum level the rocks in the vicinity of the lake, where the rocks were demagnetized by the shockwave generated upon collision of the planet with a meteorite (asteroid) [14]. As a result, the rocks surrounding the impact crater will acquire a magnetization different from that at large distances from the collision site (the place where the asteroid stroke the Earth surface). In other words, the astrobleme becomes the center of a magnetic anomaly.

Conclusion. Collisions of large meteorites (asteroids) with a planet surface lead the formation of lake of high-temperature conducting low-viscosity impact lava at the astrobleme bottom. This lava lake may feature the self-excited hydromagnetic dynamo effect providing for the appearance of an intrinsic magnetic field of the lake. Prolonged existence of this field in the vicinity of the astrobleme leads to magnetization of the rocks demagnetized by a shockwave generated upon collision of the cosmic body with the planet. This approach allows us to explain the appearance of magnetic anomalies related to the known astroblemes on the Earth surface.

REFERENCES

1. A. T. Bazilevskiĭ and B. A. Ivanov, in *News of the Science Abroad, Mechanics*, Vol. 12: *Mechanics of Crater Formation upon Impact and Explosion* (Mir, Moscow, 1977), pp. 172–227.
2. K. B. Broberg, *On the Formation of the Siljan Crater*, Preprint of the Lund Institute of Technology (Sweden, 1985); in *News of the Science Abroad, Mechanics*, Vol. 42: *Nonlinear Wave Processes* (Mir, Moscow, 1987), pp. 235–272.
3. H. J. Melosh, *Impact Cratering: a Geologic Process* (Clarendon, New York, 1989; Mir, Moscow, 1994).
4. V. I. Fel'dman, *Impactite Petrology* (Mosk. Gos. Univ., Moscow, 1990).
5. R. C. Reid and T. K. Sherwood, *Properties of Gases and Liquids* (McGraw-Hill, New York, 1966; Khimiya, Moscow, 1971).
6. *The Oxide Handbook*, Ed. by G. V. Samsonov (Metallurgiya, Moscow, 1969; Plenum, New York, 1973).
7. V. S. Popov, Sorosov. Obraz. Zh., No. 1, 74 (1995).
8. V. V. Alekseev and A. M. Gusev, Usp. Fiz. Nauk **141** (2), 311 (1983) [Sov. Phys. Usp. **26**, 906 (1983)].
9. A. V. Lykov, *Heat Exchange: A Reference Book* (Énergiya, Moscow, 1972).
10. U. I. Moiseenko, L. S. Sokolova, and V. E. Istomin, *Electrical and Thermal Properties of Rock Minerals* (Nauka, Novosibirsk, 1970).
11. N. F. Mott and É. A. Davis, *Electronic Processes in Non-Crystalline Materials* (Clarendon, Oxford, 1971; Mir, Moscow, 1974).
12. B. M. Yanovskiĭ, *Earth Magnetism* (Leningrad. Gos. Univ., Leningrad, 1978).
13. *Advances in Solar System Magnetohydrodynamics*, Ed. by E. R. Priest and A. W. Wood (Cambridge Univ., Cambridge, 1991; Mir, Moscow, 1995).
14. R. N. Keeler and E. B. Royce, in *Physics of High Energy Density: Proceedings of the International School of Physics "Enrico Fermi,"* Ed. by P. Caldirola and H. Knoepfel (Academic, New York, 1971; Mir, Moscow, 1974).

Translated by P. Pozdeev

Technical Physics Letters, Vol. 26, No. 10, 2000, pp. 857–860. Translated from Pis'ma v Zhurnal Tekhnicheskoĭ Fiziki, Vol. 26, No. 19, 2000, pp. 16–23.

Bipartition of a Strongly-Charged Droplet during Nonlinear Oscillations

S. O. Shiryaeva, A. I. Grigor'ev, and D. F. Belonozhko

Yaroslavl State University, Yaroslavl, Russia

Received March 23, 2000

Abstract—The nonlinear analysis of oscillations of a liquid droplet bearing a charge slightly below the critical value shows that, provided a sufficiently large even-mode amplitude of the initial virtual deformation, the droplet exhibits a tendency to split into two equal parts. © *2000 MAIK "Nauka/Interperiodica".*

The laws of partition of a strongly charged droplet as a result of its own charge instability development were extensively studied by both experimental and theoretical methods (see, e.g., [1–3] and references therein). As is known [1–5], the droplet partition may proceed, depending on the viscosity, via different channels, specifically, by ejecting a large number of strongly charged small daughter droplets (for a small viscosity) or by splitting into two–three parts of comparable size (for a large viscosity). The first channel was investigated in sufficient detail both experimentally and theoretically, while our knowledge of the second channel (leading to a droplet splitting into comparable parts) is still unsatisfactory. For example, despite an obvious symmetry of the problem of a viscous charged droplet partition induced by a symmetric virtual deformation (whereby we might expect that the daughter droplets would possess comparable charges and dimensions), the results of theoretical calculations performed within the framework of a linear approach [4, 5] indicate an asymmetric distribution of both mass and charge of the daughter droplets.

In connection with this, the purpose of our work was to perform a nonlinear analysis of the possible trends in the droplet splitting into two parts. Note that a nonlinear analysis of the capillary oscillations of a charged droplet performed by analytical [6] and numerical [7] methods showed indirect evidence for the possibility of symmetric bipartition.

Let us consider a droplet of the ideal perfectly conducting liquid with a density ρ and a surface tension γ bearing a charge Q. Let the droplet shape deviation from spherical at the initial time instant be described by a small perturbation ε in the amplitude of the nth linear capillary oscillation mode; the velocity field is assumed to be zero. The volume of the initial droplet is represented by the volume of a perfect sphere with the radius R. The task of calculating the shape of axisymmetric capillary oscillations of the droplet is solved by a multiscale method in a quadratic approximation with respect to the amplitude of the initial perturbation of the equilibrium spherical surface. The problem is formulated in terms of dimensionless variables defined so that $R = \rho = \gamma = 1$. The mathematical formalism is analogous to that described previously [8].

A routine calculation procedure involving cumbersome transformations leads to the following expressions describing the droplet shape at an arbitrary time instant t in the second-order approximation with respect to a small perturbation with the amplitude $\sim\varepsilon$ introduced into the main ($n = 2$), third ($n = 3$), fourth ($n = 4$) or fifth ($n = 5$) modes:

$$r = 1 - \frac{\varepsilon^2}{5}\cos^2(\omega_2 t) + \varepsilon\cos(\omega_2 t)P_2(\mu)$$

$$+ \frac{\varepsilon^2}{\omega_2^2}(\chi_1 - (\chi_1 + \chi_2)\cos(\omega_2 t) + \chi_2\cos(2\omega_2 t))P_2(\mu) \quad (1)$$

$$+ \frac{18}{35}\varepsilon^2(\chi_3 - (\chi_3 + \chi_4)\cos(\omega_4 t) + \chi_4\cos(2\omega_2 t))P_4(\mu);$$

$$r = 1 - \frac{\varepsilon^2}{7}\cos^2(\omega_3 t) + \varepsilon\cos(\omega_3 t)P_3(\mu)$$

$$+ \frac{\varepsilon^2}{21\omega_2^2}(\chi_5 + \chi_6\cos(\omega_2 t) - \chi_7\cos(2\omega_3 t))P_2(\mu)$$

$$+ \frac{\varepsilon^2}{77\omega_4^2}(\chi_8 + \chi_9\cos(\omega_4 t) + \chi_{10}\cos(2\omega_3 t))P_4(\mu) \quad (2)$$

$$+ \frac{5\varepsilon^2}{231\omega_6^2}(\chi_{11} + \chi_{12}\cos(\omega_6 t) + \chi_{13}\cos(2\omega_3 t))P_6(\mu);$$

$$r = 1 - \frac{\varepsilon^2}{9}\cos^2(\omega_4 t) + \varepsilon\cos(\omega_4 t)P_4(\mu)$$

1063-7850/00/2610-0857$20.00

$$+\frac{25\varepsilon^2}{2772\omega_2^2}(\chi_{14}+\chi_{15}\cos(\omega_2 t)-\chi_{16}\cos(2\omega_4 t))P_2(\mu)$$

$$+\frac{108\varepsilon^2}{1001\omega_4^2}(-\chi_{17}+\chi_{18}\cos(\omega_4 t)+\chi_{19}\cos(2\omega_4 t))P_4(\mu) \quad (3)$$

$$+\frac{15\varepsilon^2}{198\omega_6^2}(\chi_{20}+\chi_{21}\cos(\omega_6 t)-\chi_{22}\cos(2\omega_4 t))P_6(\mu)$$

$$+\frac{35\varepsilon^2}{2574\omega_8^2}(-\chi_{23}+\chi_{24}\cos(\omega_8 t)+\chi_{25}\cos(2\omega_4 t))P_8(\mu);$$

$$r = 1-\frac{\varepsilon^2}{11}\cos^2(\omega_7 t)+\varepsilon\cos(\omega_5 t)P_5(\mu)$$

$$+\frac{5\varepsilon^2}{2574\omega_2^2}(\chi_{26}+\chi_{27}\cos(\omega_2 t)-\chi_{28}\cos(2\omega_5 t))P_2(\mu)$$

$$+\frac{6\varepsilon^2}{143\omega_4^2}(\chi_{29}+\chi_{30}\cos(\omega_4 t)-\chi_{31}\cos(2\omega_5 t))P_4(\mu) \quad (4)$$

$$+\frac{4\varepsilon}{2805\omega_6^2}(\chi_{32}+\chi_{33}\cos(\omega_6 t)-\chi_{34}\cos(2\omega_5 t))P_6(\mu)$$

$$+\frac{7\varepsilon^2}{8151\omega_8^2}(\chi_{35}+\chi_{36}\cos(\omega_8 t)+\chi_{37}\cos(2\omega_5 t))P_8(\mu)$$

$$+\frac{441\varepsilon^2}{46189\omega_{10}^2}(\chi_{38}+\chi_{39}\cos(\omega_{10} t)-\chi_{40}\cos(2\omega_5 t))P_{10}(\mu),$$

where

$$\mu\equiv\cos(\theta);\quad W\equiv\frac{Q^2}{4\pi};\quad \omega_n^2\equiv n(n-1)[(n+2)-W];$$

$$\chi_1\equiv\frac{44-5W}{14};\quad \chi_2\equiv\frac{23W-116}{42};\quad \chi_3\equiv\frac{36-5W}{\omega_4^2};$$

$$\chi_4\equiv\frac{12+W}{4(10-W)};\quad \chi_5\equiv 2(44-3W);$$

$$\chi_6\equiv 4\frac{(3W^2+136W-784)}{(56-11W)};$$

$$\chi_7\equiv w_2^2\frac{(224-39W)}{(56-11W)};\quad \chi_8\equiv 12(101-4W);$$

$$\chi_9\equiv 24(251-59W+5W^2)\omega_2^{-2};$$

$$\chi_{10}\equiv 2(151-14W)\omega_2^{-2};$$

$$\chi_{11}\equiv 30(104-9W);\quad \chi_{12}\equiv 60\frac{(23W^2-68W-1120)}{(20-W)};$$

$$\chi_{13}\equiv 5\omega_6^2\frac{(11W-4)}{(20-W)};\quad \chi_{14}\equiv 26(22-W);$$

$$\chi_{15}\equiv\frac{32}{(140-23W)};$$

$$\chi_{16}\equiv\omega_2^2\frac{(2194-331W)}{(140-23W)};\quad \chi_{17}\equiv 0.25(1236+3W);$$

$$\chi_{18}\equiv(4+17W);$$

$$\chi_{19}\equiv 0.25(602-65W);\quad \chi_{20}\equiv(610-11W);$$

$$\chi_{21}\equiv 240\frac{(1010-37W-3W^2)}{(8-3W)};$$

$$\chi_{22}\equiv\omega_6^2\frac{(526+3W)}{6(8-3W)};$$

$$\chi_{23}\equiv 56(220-13W);$$

$$\chi_{24}\equiv 28\frac{(2620+796W-95W^2)}{(34-W)};$$

$$\chi_{25}\equiv\omega_8^2\frac{7(32-29W)}{(34-W)};\quad \chi_{26}\equiv 6(524-17W);$$

$$\chi_{27}\equiv 20\frac{(-12304+1688W+5W^2)}{(92-13W)};$$

$$\chi_{28}\equiv\omega_2^2\frac{(5396-713W)}{(92-13W)};$$

$$\chi_{29}\equiv 12(36+W);\quad \chi_{30}\equiv\frac{2(-738-151W+34W^2)}{(122-17W)};$$

$$\chi_{31}\equiv\omega_4^2\frac{36(162-17W)}{(122-17W)};\quad \chi_{32}\equiv 30(1028+21W);$$

$$\chi_{33}\equiv\frac{60(6416-1876+209W^2)}{(32-5W)};$$

$$\chi_{34}\equiv\omega_6^2\frac{(5716-313W)}{(32-5W)};$$

$$\chi_{35}\equiv 56(724-7W);$$

$$\chi_{36}\equiv\frac{560(-2422-340W+35W^2)}{W};$$

$$\chi_{37}\equiv\omega_8^2\frac{7(346-47W)}{W};\quad \chi_{38}\equiv 90(396-17W);$$

$$\chi_{39}\equiv\frac{180(-4464-2816W+239W^2)}{(52-W)};$$

$$\chi_{40}\equiv\omega_{10}^2\frac{9(108-55W)}{(52-W)}.$$

The envelope shapes calculated by Eqs. (1)–(4) are presented in the figure where the horizontal axis coincides with the droplet symmetry axis. The envelopes a–d

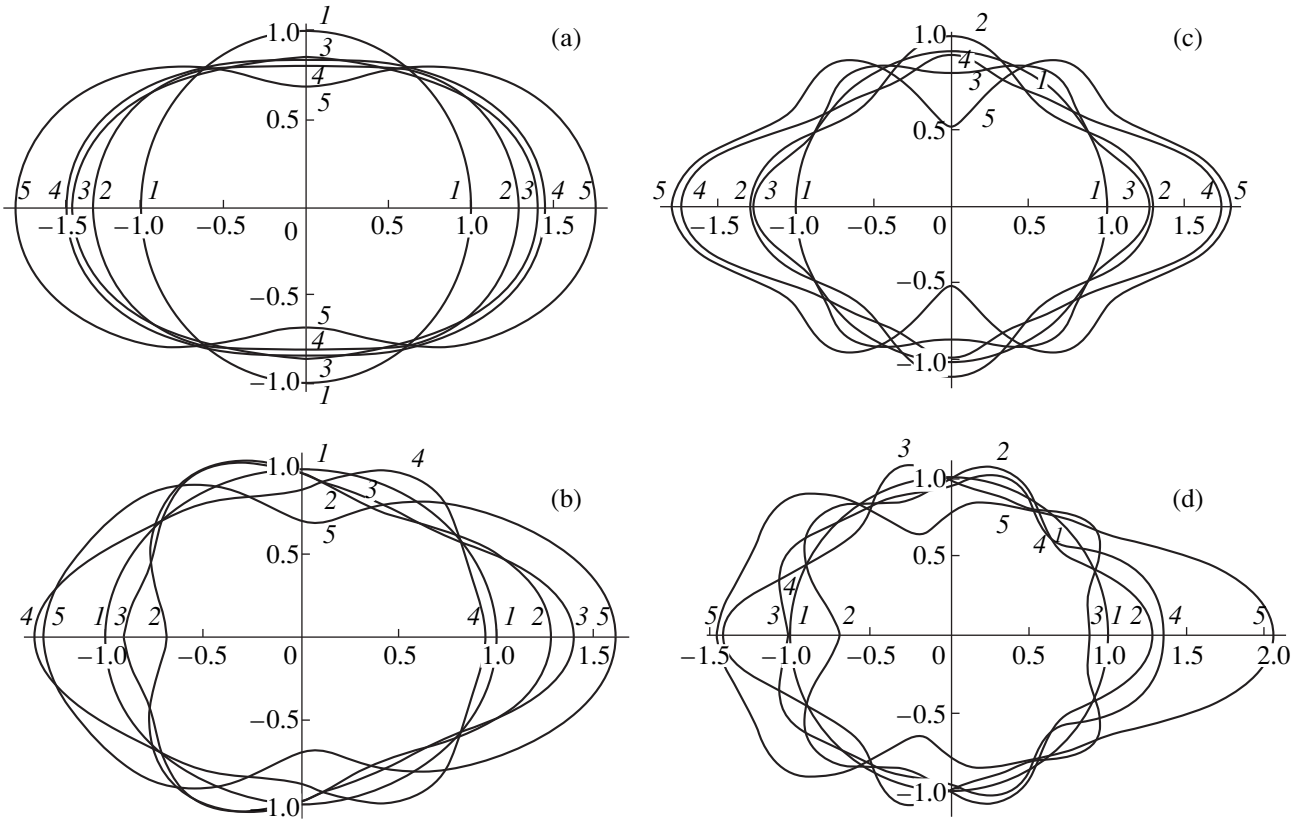

Fig. 1. Evolution of the envelope contours calculated at various time instants t for a droplet with the initial equilibrium spherical shape (curves *1*) perturbed at the initial time instant by introducing a virtual deformation representing various modes (curves *2*) of the type $\varepsilon P_n(\cos\theta)$ with the amplitude $\varepsilon = 0.3$ ($n = 2$–5): (a) $n = 2$, $W = 3.9$; $t = 0.14\varepsilon^{-1}$ (*3*), $0.28\varepsilon^{-1}$ (*4*), $0.56\varepsilon^{-1}$ (*5*); (b) $n = 3$, $W = 3.8$; $t = 0.065\varepsilon^{-1}$ (*3*), $0.26\varepsilon^{-1}$ (*4*), $0.585\varepsilon^{-1}$ (*5*); (c) $n = 4$, $W = 3.8$; $t = 0.24\varepsilon^{-1}$ (*3*), $0.36\varepsilon^{-1}$ (*4*), $0.57\varepsilon^{-1}$ (*5*); (d) $n = 5$, $W = 3.8$; $t = 0.1\varepsilon^{-1}$ (*3*), $0.2\varepsilon^{-1}$ (*4*), $0.475\varepsilon^{-1}$ (*5*).

were determined at various dimensionless time instants and the Rayleigh parameters $W = Q^2/4\pi$ close to the critical level (the critical W value determined for the onset of instability of a spherical droplet was $W_* = 4$); the initial perturbation of the equilibrium spherical shape corresponded to various modes with n = 2–5, respectively. It should be noted that the domain of uniform validity of Eqs. (1)–(4) is determined, according to the perturbation theory concepts, by the condition $t < \varepsilon^{-1}$. In fact, the restriction with respect to time t is even more rigid, as is clearly illustrated by data presented in the figure, where curves *4* correspond to a boundary of the domain of validity of the uniform expansion. This follows from a comparison of the amplitudes of the final deviations of the droplet surface from the initial shape (cf. curves *4* and *2*) and is manifested by the obvious lack of conservation of the initial droplet volume for the envelopes depicted by curves *4*.

As can be readily seen, once the initial perturbation in the equilibrium droplet shape is determined by even Legendre's polynomials (see Fig. 1), the droplet envelope at any time instant is determined by the even polynomials as well and is symmetric relative to the origin. For a sufficiently large t (close to the boundary of the domain of solution uniformity with respect to variable t), the drop exhibits a tendency to split into two equal parts.

Should the initial perturbation be determined by the odd Legendre's polynomials (see Fig. 1), the droplet shape at any time instant is asymmetric relative to the origin (despite the fact that the mode interaction for the second-order perturbation ε only gives rise to the even modes). In this case, the drop exhibits a tendency to split asymmetrically.

According to the general physical considerations, it is obvious that taking into account the viscosity (ignored above) would lead to the decay of all modes. However, the decrement of higher modes being greater compared to that of lower modes, the amplitude of an initially perturbed high odd mode may drop to zero faster than amplitudes of the excited lower even modes. As a result, the subsequent oscillations of the droplet and its possible bipartition pattern will be symmetric.

Conclusion. Symmetric bipartition of an unstable strongly charged droplet with the formation of two parts having comparable charges and masses must

actually take place. The results of previous descriptions of the droplet partition by analytical and numerical methods, showing no evidence of this channel, are apparently explained by models that are too rough. As seen from Eqs. (1)–(4), the droplet surface oscillations take place (irrespective of the initial perturbation symmetry) in the vicinity of a certain spheroidal figure determined by time-independent terms in these equations rather than in the vicinity of a sphere.

REFERENCES

1. A. I. Grigor'ev and S. O. Shiryaeva, Zh. Tekh. Fiz. **61** (3), 19 (1991) [Sov. Phys. Tech. Phys. **36**, 258 (1991)].
2. A. I. Grigor'ev and S. O. Shiryaeva, Izv. Akad. Nauk, Mekh. Zhidk. Gaza, No. 3, 3 (1994).
3. A. I. Grigor'ev, Zh. Tekh. Fiz. **70** (5), 22 (2000) [Tech. Phys. **45**, 543 (2000)].
4. V. A. Koromyslov, A. I. Grigor'ev, and S. O. Shiryaeva, Zh. Tekh. Fiz. **68** (8), 31 (1998) [Tech. Phys. **43**, 904 (1998)].
5. S. I. Shchukin and A. I. Grigor'ev, Zh. Tekh. Fiz. **70** (4), 1 (2000) [Tech. Phys. **45**, 381 (2000)].
6. J. A. Tsamopoulos, T. R. Akilas, and R. A. Brawn, Proc. R. Soc. London, Ser. A **401**, 67 (1985).
7. N. A. Pelekasis, J. A. Tsamopoulos, and G. D. Manolis, Phys. Fluids A **2** (8), 1328 (1990).
8. D. F. Belonozhko and A. I. Grigor'ev, Pis'ma Zh. Tekh. Fiz. **25** (15), 41 (1999) [Tech. Phys. Lett. **25**, 610 (1999)].

Translated by P. Pozdeev

Technical Physics Letters, Vol. 26, No. 10, 2000, pp. 861–863. Translated from Pis'ma v Zhurnal Tekhnicheskoĭ Fiziki, Vol. 26, No. 19, 2000, pp. 24–29.

Resonance in the Efficiency of the Conduction-State Formation in Ion-Bombarded Crystalline Quartz

V. F. Pichugin* and T. S. Frangul'yan

Tomsk Polytechnical University, Tomsk, 634034 Russia

** e-mail: pichugin@oasis.cctpu.edu.ru*

Received April 10, 2000

Abstract—A resonance in the ion conductivity as function of the bombarding-ion mass number was observed in ion-irradiated crystalline quartz. The resonance is observed at the optimum ratio of the energy losses for the nuclear and electron stopping of the impinging ions interacting with crystalline quartz in the range of ion mass numbers from 35 to 45 amu. © *2000 MAIK "Nauka/Interperiodica".*

One of the most pronounced effects observed in the interaction of ion beams with dielectric materials (in particular, quartz) is a dramatic increase in the electric conductivity of the target material [1, 2]. Ion bombardment changes the quartz conductivity from 10^{-17} up to $10^3\ \Omega^{-1}\ cm^{-1}$, that is, by a factor of 10^{20}. The practical use of this effect requires the development of special methods for controlling the relevant properties. The present study deals with the efficiency of ion beams of various chemical elements inducing the conduction state in quartz.

Polished 0.1-mm-thick quartz plates (AT-cuts) were irradiated with stationary and frequency-modulated pulsed beams of the following ions with diverse properties: H^+, He^+, C^+, O^+, Al^+, Si^+, Ar^+, Cu^+, Cd^+, and Pb^+. The bombarding ion energies varied from 20 to 100 keV, the irradiation dose being 10^{16} ion/cm^2 in all cases. The microscopic examination of the ion-bombarded quartz specimens showed that irradiation caused no changes in the surface relief. An important role of the postimplantation thermal treatment of quartz plates is well known [2]; therefore, all the ion-irradiated specimens were heated in vacuum up to a temperature of 600 K in order to stabilize the effect of elevated conductivity. Then, the specimens were cooled to room temperature to measure their conductivity.

It is well known that quartz in the initial (unirradiated) state possesses conductivity of the ionic type [3]. The bombardment of quartz specimens with various ions resulted in qualitatively the same effect—an increase in the conductivity by a factor ranging from 10^5 to 10^{20} depending on the mass number of the bombarding ions (Fig. 1). The increase in conductivity was accompanied by lowering the electron transfer activation energy from 1.5 eV (characteristic of unirradiated specimens) to a value on the order of 0.03 eV (for irradiated specimens).

To compare the effects of bombardment with ions of different masses and energies, we computed the volume conductivity σ_v of ion-modified layers using the bombarding ion projection ranges calculated by the TRIM program [4]. Our previous studies [2] showed that the irradiation-induced conduction state of quartz was determined by a considerable structural rearrangement of the lattice. This rearrangement was caused mainly by the ion bombardment process and was almost independent of the chemical nature of implanted ions. Thus, the mechanism of electron transfer in ion-

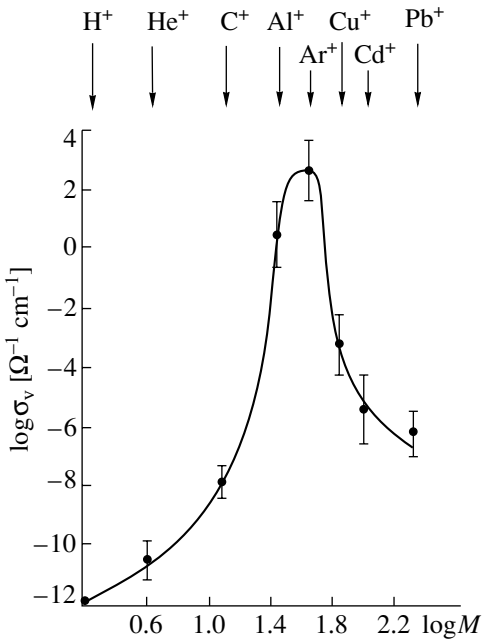

Fig. 1. Volume conductivity σ_v of crystalline quartz specimens versus the implanted ion mass number M (irradiation dose $D = 1 \times 10^{16}$ ion/cm^2; bombarding ion energy E = 100 keV).

1063-7850/00/2610-0861$20.00 © 2000 MAIK "Nauka/Interperiodica"

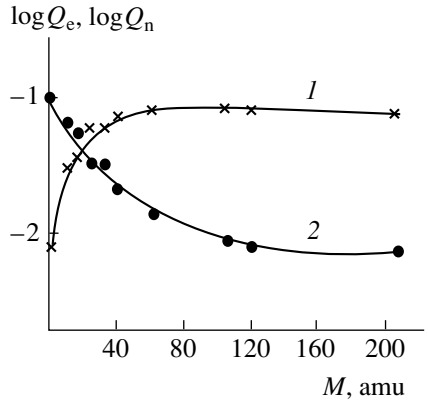

Fig. 2. Energy losses for the (*1*) nuclear Q_n, and (*2*) electron Q_e stopping versus the bombarding ion mass number M (ion energy E = 100 keV; target material, silicon dioxide SiO_2).

modified layers of quartz crystals can be called "universal" since it is independent of the implanted ion nature.

The conductivity of ion-implanted layers depends on the atomic mass of an implanted chemical element. Figure 1 shows the plot of the volume conductivity (σ_v) of ion-bombarded quartz layers versus the mass number (M) of these ions, $\sigma = f(M)$. It is seen that σ_v dramatically (by more than 14 orders of magnitude) increases with the mass number M of the implanted ions in the range from 1 to 40 amu. A further increase of the bombarding ion mass from 40 up to 207 amu results in a sharp decrease in σ_v of the ion-irradiated layers. The experimental curve $\sigma = f(M)$ shows that the efficiency of the conduction state formation in ion-irradiated crystalline quartz is a function of the mass number M of the bombarding ions and has a resonance with the maximum at M = 40 amu. Obviously, this dependence is determined by features of the structural rearrangement and the chemical changes occurring at the crystal surface interacting with particles of various masses.

To interpret the experimentally observed extremum in the curve of $\log\sigma_v = f(M)$, we considered the interactions between impinging ions and the crystal. The energy of high-energy ions interacting with a solid is dissipated mainly via two channels. A part of the ion energy is dissipated in elastic collisions with the target nuclei, which results in the displacements of target atoms from regular sites in the crystal lattice. The other part of the ion energy is dissipated in inelastic interactions with the electron subsystem. Our computations provided an evaluation of the ratio of these two types of energy losses. The computation of the nuclear and electron stopping powers, $S_n(E)$ and $S_e(E)$, was performed within the framework of the Lindhard theory. The interaction potential $V(r)$ was a conventional Coulomb potential, while the screening function was also used in the form suggested by Lindhard [5]. The nuclear (Q_n) and electron (Q_e) stopping losses were computed by the algorithm described in [6] based on the model in which the target was assumed to be homogeneous and isotropic, the channeling effect was ignored, and the nuclear and electron stopping powers were assumed to be independent. The energy losses were computed in the one-particle approximation.

The results of the numerical computations (Fig. 2) show that, with an increase in the mass number of the bombarding ions, the energy losses for the nuclear stopping increase, whereas the energy losses caused by the electron stopping processes decrease. In the range of the bombarding ion mass numbers from 30 to 40 amu, the energy losses for the nuclear and electron stopping are equal. Thus, it is mainly the process of nuclear stopping (accompanied by atomic displacements in the lattice) that is responsible for the disturbance of the long-range order and the surface amorphization. Quartz belongs to the materials with mainly covalent bonding and is amorphized at low irradiation doses: on the order of 10^{15} ion/cm^2.

The experimental conditions of our study allowed us to assume that the irradiation-modified quartz layers are in the amorphous state, which differs from the crystalline state by the fact that the formation of the "defect structure" of amorphous layers caused by the ion irradiation is strongly dependent on electron excitations capable of generating defects by a subthreshold mechanism that requires much lower energies [7–9]. The electron excitations are responsible for the formation of defects of the dangling bond type leading, in turn, to the appearance of weakly bound bridging oxygen atoms. The probability of desorption of these weakly bound bridging oxygens from the surface increases due to the bond excitation. The electron processes are mainly responsible for the preferential removal of oxygen atoms from the quartz surface [10–12] and the surface enrichment with excess silicon participating in the formation of a system of localized states caused by bond "switching."

As the impinging ion mass M grows, the fraction of elastically scattered energy increases as well (Fig. 2, curve *1*). This, in turn, promotes the transition of the surface layer into an amorphous state because of the increase in the number of displaced ions. However, this is a necessary but not sufficient condition for the formation of a system of energy states determining the electron transfer. It seems that the formation of these states depends mainly on the electron excitation processes, the efficiency of which decreases with an increasing ion mass number M (Fig. 2, curve *2*). It is a superposition of these processes, with the optimum ratio being observed at M = 40 amu, that gives rise to the resonance in the ion-induced conductivity dependent on the bombarding ion mass number.

REFERENCES

1. V. F. Pichugin, A. N. Feodorov, and A. I. Shmyrin, Phys. Res. **13**, 337 (1989).

2. V. F. Pichugin, T. S. Frangul'yan, V. A. Tishkina, *et al.*, Available from VINITI, No. 08-66/878, 1993.
3. S. Lazzari, M. Martini, *et al.*, Nucl. Instrum. Methods Phys. Res. B **32**, 299 (1988).
4. J. F. Ziegler, J. P. Biersack, and K. Littmark, *Stopping and Ranges of Ions in Matter* (Pergamon, New York, 1985).
5. J. Lindhard, Usp. Fiz. Nauk **99**, 249 (1969).
6. V. P. Krivobokov and O. V. Pashchenko, Zh. Tekh. Fiz. **61** (3), 188 (1991) [Sov. Phys. Tech. Phys. **36**, 367 (1991)].
7. H. Fischer, G. Gotz, and H. Karge, Phys. Status Solidi A **76**, 493 (1983).
8. U. Yarkulov, Zh. Tekh. Fiz. **54** (11), 2222 (1984) [Sov. Phys. Tech. Phys. **29**, 1302 (1984)].
9. J. J. Comer, C. Bergeron, and L. F. Lowe, Mater. Res. Bull. **8**, 505 (1973).
10. R. G. Makcaulay-Newcomber, D. A. Thompson, *et al.*, Nucl. Instrum. Methods Phys. Res. B **46**, 180 (1990).
11. L. I. Pranyavichyus, S. I. Tamulevichyus, and A. P. Matyukas, Pis'ma Zh. Tekh. Fiz. **11** (24), 1512 (1985) [Sov. Tech. Phys. Lett. **11**, 624 (1985)].
12. P. V. Pavlov, Dokl. Akad. Nauk SSSR **258** (3), 617 (1981) [Sov. Phys. Dokl. **26**, 464 (1981)].

Translated by L. Man

Technical Physics Letters, Vol. 26, No. 10, 2000, pp. 864–866. Translated from Pis'ma v Zhurnal Tekhnicheskoĭ Fiziki, Vol. 26, No. 19, 2000, pp. 30–38.

The Effect of Fullerenes on the Dynamic Characteristics of Liquid Crystal Systems

N. V. Kamanina* and L. N. Kaporskiĭ

Vavilov Optical Institute, State Scientific Center of the Russian Federation, St. Petersburg, 190164 Russia

** e-mail: kamanin@ffm.ioffe.rssi.ru*

Received April 25, 2000

Abstract—Time and modulation characteristics of the electrically controlled liquid crystal cells (conventional nematic or containing a polymer-dispersed layer) with fullerene-modified orienting coatings are studied as being dependent on the amplitude and repetition rate of applied electric pulses. A substantial decrease in the switching time of the liquid crystal systems with fullerene-containing orienting layers is demonstrated. The effect of data storage controlled by variable electric pulse duration is observed in fullerene-containing polymer-dispersed liquid crystal systems. © *2000 MAIK "Nauka/Interperiodica".*

Nematic liquid crystals, offering a unique model system enabling one to verify physical models describing the dynamics of electrooptical effects in the liquid-crystal line mesophases, are widely used in science, display technology, and medicine. The liquid crystals (LCs) used in laser shutters, light modulators, and other real-time devices must provide a fast response, high contrast, and good modulation characteristics. All these tasks can be solved by optimizing the applied voltage, minimizing the LC thickness, varying the electrooptical layer viscosity, and appropriately orienting LC molecules at the substrate surface by properly selecting the orienting coatings. The latter factor influences the electrooptical response kinetics in LCs [1, 2] and related light modulators [3], which is explained by difference in the physical conditions at the solid–LC interface.

The purpose of this work was to use the fullerene-containing orienting coatings based on thin polyimide films to improve the switching and modulation characteristics of the nematic LC cells and polymer-dispersed systems.

Experiments were performed using the S-type cells with an initial planar orientation. The electrooptical layer employed standard nematic LC systems with a positive optical and dielectric anisotropy: NZhK 1282 ($\Delta n = 0.164$, $\Delta\varepsilon = 9.9$), NZhK 1289 ($\Delta n = 0.168$, $\Delta\varepsilon = 10$), and E7 BDH ($\Delta n = 0.224$, $\Delta\varepsilon > 0$). The thickness of the LC layers was 10 μm. The polymer-dispersed systems used 2-cyclooctylamino-5-nitropyridine (COANP) as a photosensitive component. The refractive index of this substance at room temperature is close to that of the studied LC systems (ordinary wave). The ratio of the photosensitive and electrooptical components was 1 : 2. Nonphotosensitive 81A polyimide was used as a plasticizer. Note that the COANP structure was preliminarily sensitized by fullerene C_{70} at a concentration of 5 wt % relative to pure COANP in order to shift the COANP absorption spectrum toward the excitation laser wavelength (633 nm). Previously [4], it was demonstrated that the absorption spectrum of a fullerene-containing COANP can be readily shifted from 430 to 710–800 nm by varying the fullerene concentration.

The LC-orienting films with a thickness of about 0.5 μm were deposited onto transparent conducting underlayers (indium and tin oxides) on K8 glass substrates. To ensure orientation of the LC molecules, we used 2.5–3% solutions of 81A and 81B polyimides in tetrachloroethane with fullerene additives (C_{60} and C_{70}) at a concentration of 0.1–0.5 wt % relative to the polyimide dry weight. Note that tetrachloroethane is a good solvent for both polyimides and fullerene clusters [5], which makes it possible to obtain sufficiently uniform thin orienting layers. The orienting agent was deposited onto a substrate by centrifuging, dried for 8–12 h to complete solvent evaporation, and rubbed by a flannel fabric.

Power to the cells was supplied by rectangular electric pulses with an amplitude of A = 10–60 V, a duration of τ_{sup} = 5–100 ms, and a repetition rate of $1/T$ = 0.5–35 Hz. We used a He–Ne laser (λ = 633 nm) to measure changes in the transmittance of a cell placed between crossed polarizers. The experimental arrangement was similar to that described in [6]. We studied the characteristic build-up time of the electrooptical response using the first transmittance oscillation and accurately detected a transition into the neighboring extreme position in the S-curve corresponding to the phase shift by π. Relaxation of the polymer-dispersed systems to the initial state could be observed in the same oscilloscope scale, whereas the conventional LC cells exhibit longer characteristic times. Note that the

1063-7850/00/2610-0864$20.00

pulsed voltage makes it possible to avoid a substantial influence of the polarization effects on the time characteristics that plays a negative role in the case of measurements using dc supply voltage. The latter factor can also induce dissociation of the LC molecules leading to an uncontrolled modulation of the LC director.

Figure 1 shows the plots of the characteristic time of the LC cell activation (t_{on}) versus the electric pulse amplitude measured at τ_{sup} = 30 ms and $1/T$ = 0.5 Hz. The activation time is defined as a time of the electrooptical response build-up from 0.1 to 0.9 of the maximum value. The deactivation time (t_{off}) is defined as the time of the response relaxation from its maximum value down to the 0.1 level. All the LC cells studied exhibit a decrease in the activation time with the pulse amplitude increasing from 15–20 to 60 V. This behavior is in good agreement with the inverse square dependence of the liquid-crystal line nematic mesophase relaxation time on the applied voltage and agrees with the activation time values theoretically determined for the given thickness of the electrically controlled layer and standard values of the viscosity and the coefficient of elasticity [7].

We emphasize a substantial decrease in the activation time upon variation of the boundary conditions related to the use of the fullerene-containing orienting coating. The use of the fullerene-containing orienting agent in the conventional nematic LC structures and in the polymer-dispersed cells leads to a decrease in the activation time by 50–100 and 20%, respectively (compare curve *1* to curve *2* and curve *3* to curve *4* in Fig. 1). The experimental results showed no clear influence of the fullerene molecular structure (C_{60} or C_{70}) on the switching time range.

Note that the conventional nematic LC cells exhibit activation at the applied pulse voltage of 12–15 V, whereas the polymer-dispersed systems start working only at 20–25 V. In addition, the latter systems exhibit a virtually symmetric response (e.g., the cell with a fullerene-free orienting agent characterized by curve *3* in Fig. 1 shows the ratio of the activation and deactivation times t_{on}/t_{off} = 3.5/4 ms at A = 55 V and τ_{sup} = 30 ms) and a stronger dependence of the time characteristics on the applied pulse duration. These features allow us to conclude that the polymer-dispersed fullerene-containing structures can exhibit some kind of a memory effect. Figure 2 shows the corresponding plot of the data storage time t_s (electrooptical response evolves during the time interval t_{on}, remains constant during the time interval t_s, and decays during the time interval t_{off}) versus the supply voltage pulse duration at A = 55 V and the repetition rate $1/T$ = 0.5 Hz. A slight tendency to saturation observed at a pulse duration of 70–90 ms is also pronounced for τ_{sup} increased to 100–300 ms. We did not make measurements at longer pulse durations to avoid dissociation of LC molecules under quasi-continuous operation conditions.

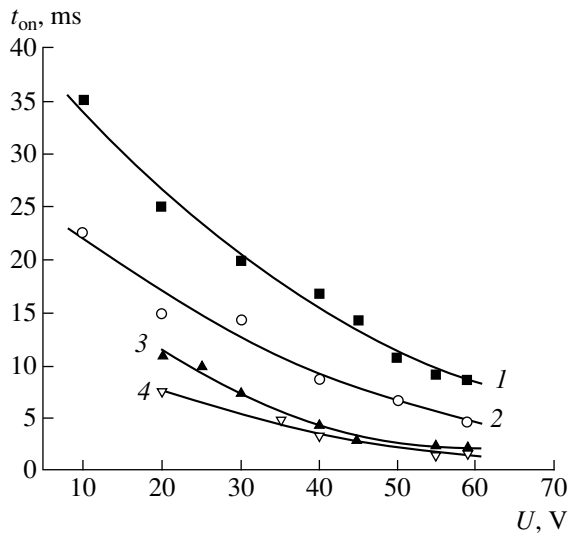

Fig. 1. Plots of the activation time (t_{on}) versus the supply voltage pulse amplitude for (*1*, *2*) nematic LC cells and (*3*, *4*) polymer-dispersed LC structures with (*1*, *3*) fullerene-free orienting agent and (*2*, *4*) fullerene-containing orienting coating.

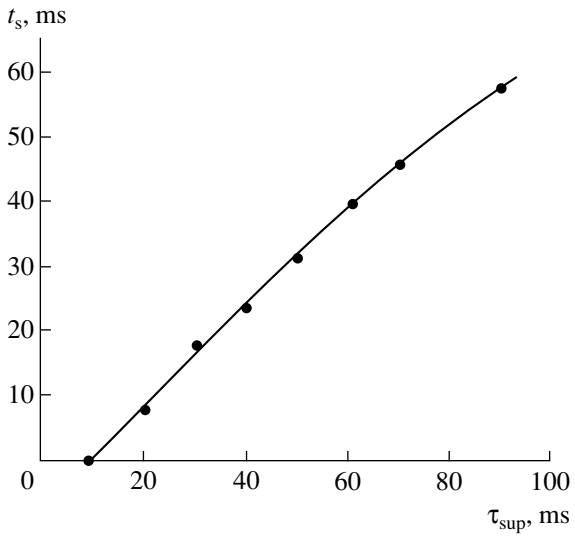

Fig. 2. A plot of the data storage time versus the electric pulse duration for a polymer-dispersed LC cell with a fullerene-free orienting agent (representing curve *3* in Fig. 1).

A physical reason for the memory effect in a polymer-dispersed cell is quite simple and can be explained as follows [8, 9]. Effective light scattering due to a refractive index gradient at the LC–polymer interfaces accounts for low transmittance in the initial state. An electric or magnetic field orients the nematic and leads to a leveling of the refractive indices of LC and polymer. The orientation is retained even after termination of the field action due to a strong adhesion of the nematic molecules to the surface of dispersed polymer drops. The memory effect at a high supply voltage is

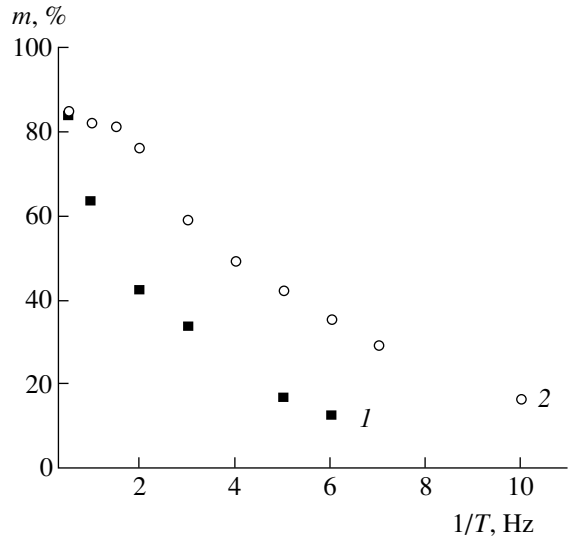

Fig. 3. Plots of the modulation amplitude *m* versus the repetition rate of the electric pulses for nematic LC cells with (*1*) fullerene-free orienting agent and (*2*) fullerene-containing orienting coating (representing curves *1* and *2* in Fig. 1).

related to the orientation of the LC molecules along the electric field strength vector ($\Delta\varepsilon > 0$ for LCs with positive anisotropy of the dielectric constant) and to the increase in motility of the polymer matrix molecules capable of changing the anisotropy of the surface forces (determined by the balance of the elastic and adhesive forces at the nematic–polymer interface).

Barannik *et al.* [9] demonstrated that the characteristic time of the polymer-dispersed system relaxation after termination of the electric field action can be as long as 15–20 min. In our experiments, the data storage time is comparable with the electric pulse duration. The system loses memory and relaxes to the initial state in a few milliseconds. This is apparently related to the influence of the fullerene admixture present in the photosensitive component, which leads to a partial orientation and clarification of the cell in the initial state (zero voltage) and decreasing the deactivation time. However, the effect of data storage controlled by variable electric pulse duration can be used in the development of liquid-crystal displays with new photoactive molecules and can be helpful in the studies of the optical confinement of laser radiation in a polymer-dispersed medium, since this effect may substantially change the kinetics of the absorption saturation and influence the level of the optical confinement.

Figure 3 shows a plot of the modulation amplitude in the nematic LC cells (see curves *1* and *2* in Fig. 1) versus the repetition rate of the electric pulses. Note that fullerene additives modifying the orienting layer and sensitizing the photosensitive component of the polymer-dispersed system lead to the extension of a nonlinear part of the modulation curves and increase the cell operation rate (to 35 Hz in the polymer-dispersed LC system). A decrease in the modulation level (to 80%) in the polymer-dispersed cells as compared to standard nematic LC cells (about 85%) is related to the aforementioned clarification effect in the initial state (at zero applied voltage) possibly due to additional orientation of the LC molecules by fullerenes.

Thus, we studied the time characteristics and demonstrated a substantial decrease in the activation time of nematic LC cells and polymer-dispersed LC systems with fullerene-containing orienting coatings. The polymer-dispersed LC systems based on a nematic LC and COANP with fullerenes exhibit the memory effect controlled by variable electric pulse duration. The results can be used in the development of the novel real-time LC display systems and the analysis of complicated kinetic processes of the laser radiation saturation confinement in a polymer-dispersed LC medium.

The authors are grateful to B. V. Kotova and V. I. Berendyaeva (Karpov Institute of Physical Chemistry, State Scientific Center, Moscow) for providing dry nonphotosensitive polyimides 81A and 81B, to O. D. Lavrentovich (Kent State University, Ohio, USA) for providing E7 (BDH) LC, and to A. Leyderman and A. Barrientos (Department of Physics, University of Puerto Rico, USA) for the opportunity to study the photosensitive COANP molecules. The third-year students of the St. Petersburg State University L. P. Rakcheeva and M. M. Mikhaĭlova took part in the experiments.

This work was supported by the State Program "Optoelectronic and Laser Technologies."

REFERENCES

1. E. S. Luk'yanchenko, V. A. Kozunov, and V. I. Grigos, Usp. Khim. **54** (2), 214 (1985).
2. V. S. Myl'nikov and E. A. Morozova, Zh. Tekh. Fiz. **54** (10), 1980 (1984) [Sov. Phys. Tech. Phys. **29**, 1163 (1984)].
3. N. V. Kamanina and N. A. Vasilenko, Opt. Quantum Electron. **29**, 1 (1997).
4. N. Kamanina, A. Barrientos, A. Leyderman, *et al.*, Mol. Mater. **13** (1–4), 275 (2000).
5. R. S. Ruoff, D. S. Tse, R. Malhotra, and D. S. Lorents, J. Phys. Chem. **97**, 3379 (1993).
6. N. V. Kamanina and V. I. Berendyaev, Proc. SPIE **3292**, 154 (1998).
7. L. M. Blinov, *Electro-Optical and Magneto-Optical Properties of Liquid Crystals* (Nauka, Moscow, 1978; Wiley, New York, 1983).
8. G. M. Zharkova and A. S. Sonin, *Liquid-Crystalline Composites* (Nauka, Novosibirsk, 1994).
9. A. V. Barannik, S. L. Smorgon, V. Ya. Zyryanov, and V. F. Shabanov, Opt. Zh. **64** (5), 99 (1997) [J. Opt. Technol. **64**, 486 (1997)].

Translated by A. Chikishev

Technical Physics Letters, Vol. 26, No. 10, 2000, pp. 867–869. Translated from Pis'ma v Zhurnal Tekhnicheskoĭ Fiziki, Vol. 26, No. 19, 2000, pp. 39–45.

Modeling of the Internal Circulation Constraint Formation in the FT-2 Tokamak

S. P. Voskoboĭnikov, S. I. Lashkul, A. Yu. Popov, and V. A. Rozhanskiĭ

Ioffe Physicotechnical Institute, Russian Academy of Sciences, St. Petersburg, 194021 Russia

St. Petersburg State Technical University, St. Petersburg, 195251 Russia

Received May 24, 2000

Abstract—A change in the heat transfer conditions and a mechanism of the internal circulation constraint formation were modeled using a self-consistent BATRAC code. It is demonstrated that conditions favoring a sharp drop in the heat transfer may arise in experiments on the FT-2 tokamak as a result of the ion temperature rise from 100 to 300 eV at the center of the plasma column caused by the effective lower hybrid heating power absorption by the ions. A key point in this phenomenon is related to a growth in the radial electric field strength and the poloidal rotation velocity shear. © *2000 MAIK "Nauka/Interperiodica".*

Introduction. Experiments carried out on the FT-2 tokamak (R = 55 cm; a = 8 cm; I_{pl} = 22 kA; B_T = 2.2 T) with an additional lower hybrid HF heating (P_{HF} = 100 kW; f = 920 MHz) gave evidence of the internal circulation constraint (ICC) formation [1]. As a result of the effective HF power absorption, the ion temperature T_i starts increasing immediately upon switching on the additional hating. At the same time, a sharp growth in the electron temperature (T_e) and density (n_e) at the center of the plasma column begins 1–2 ms after the HF heating onset. The T_e and n_e profiles obtained by the Thompson scattering diagnostics [2] exhibit the characteristic regions of large gradient at r = 3 and 6 cm, respectively, which is indicative of the ICC formation. This was accompanied by an 8- to 10-fold drop in the effective electron heat transfer coefficient (approaching the neoclassical values) at the center of the plasma column. The fact that the T_e and n_e growth was mostly due to the improved plasma confinement conditions in the column is confirmed by these parameters being retained and even increased in the post-heating stage.

In order to explain the ICC formation, we suggested that the effective central heating (with the T_i increased from 100 to 300 eV) leads to a change in the radial electric field profile and, hence, in the poloidal velocity shear. This process may play a key role in suppressing the heat transfer in the plasma. Therefore, experimental verification of the hypothesis about the additional radial field production and an additional shear in the poloidal plasma rotation velocity (ω_s) affecting the heat transfer conditions is an important part of the plasma experiment.

It should be noted that a mechanism of the heat transfer suppression at the expense of an increased poloidal rotation velocity shear, explaining a transition to the improved plasma confinement regime, was previously put forward and experimentally confirmed in some large-scale setups [3, 4] where the ICC formation was due to an additional heating caused by the neutral ion beams (NBI) or HF fields (IBW). Despite certain progress in elucidating the physical mechanisms responsible for the anomalous heat transfer suppression, reliable reconstruction of the real pattern of events requires using numerical modeling based on a self-consistent code.

Below, we present the results of numerical calculations performed using a self-consistent BATRAC transport code [5]. In this code, evolution of the plasma parameters (and the ICC formation) is controlled by the transfer coefficients that are assumed to be functions of the ω_s value. The radial electric field profile E_r at a given time instant is reconstructed using the profiles of n_e, T_i, and E_ϕ (the toroidal electric field strength) determined by numerical calculation. The results of modeling showed that the central heating of ions may in fact play a key role in suppression of the turbulent transport of particles and heat, as well as in the ICC formation.

Theoretical model. The BATRAC transport code includes a self-consistent set of equations describing dynamics of the concentration, temperature, and poloidal field strength profiles:

$$\frac{\partial n}{\partial t} - \frac{1}{r}\frac{\partial}{\partial r}\left[rD(\omega_s)\frac{\partial n}{\partial r} - V(\omega_s)n \right] = S, \tag{1}$$

$$\frac{3}{2}n\left(\frac{\partial T_{e,i}}{\partial t} + \frac{\mathbf{\Gamma}}{n}\nabla T_{e,i}\right) + nT_{e,i}\nabla\frac{\mathbf{\Gamma}}{n} - \frac{1}{r}\frac{\partial}{\partial r}\left[r\frac{3}{2}n\chi(\omega_s)\frac{\partial T_{e,i}}{\partial r} \right] = Q_{e,i}, \tag{2}$$

$$\frac{\partial B_\vartheta}{\partial t} = \frac{\partial}{\partial r}\left[\frac{c^2}{4\pi\sigma_\parallel r}\frac{\partial}{\partial r}(rB_\vartheta) \right], \tag{3}$$

where $\sigma_\parallel$ is the neoclassical conductivity.

1063-7850/00/2610-0867$20.00

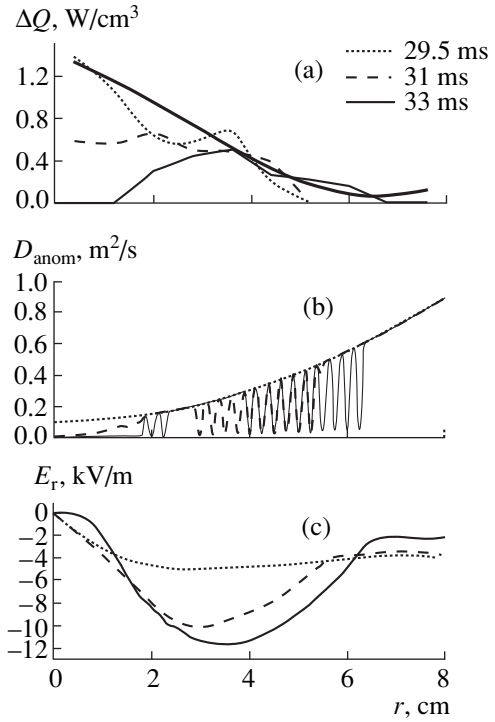

Fig. 1. Radial profiles of (a) the density ΔQ of sources of the additional ion heating, (b) anomalous diffusion coefficient D_{anom}, and (c) radial electric field strength E_r calculated using the experimental data for three different time instants: (dotted curves) 29.5 ms; (dashed cures) 31 ms; (thin solid curves) 33 ms. Thick solid curve (a) represents the source of ion heating used in the numerical calculation.

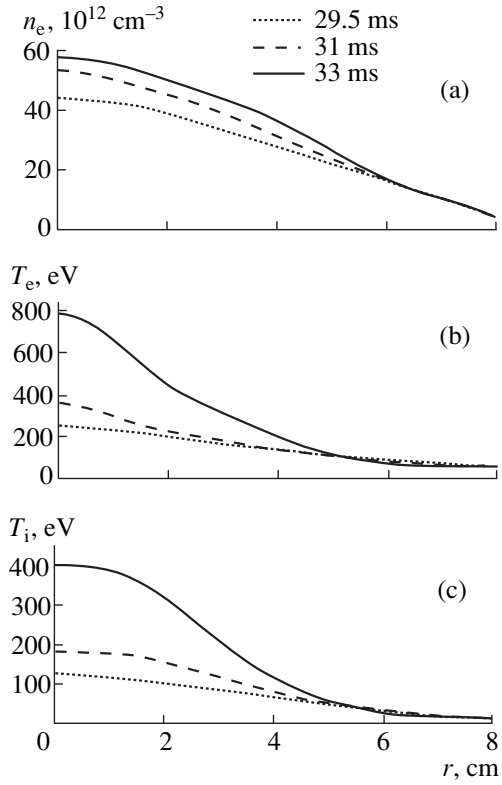

Fig. 2. Radial profiles of (a) electron concentration n_e, (b) electron temperature T_e, and (c) ion temperature T_i calculated for three different time instants: (dotted curves) 29.5 ms; (dashed cures) 31 ms; (thin solid curves) 33 ms.

The code assumes that the transfer coefficients depend only on the poloidal rotation velocity shear ω_s [4]

$$\omega_s = \frac{RB_\vartheta}{B}\frac{\partial}{\partial r}\left(\frac{E_r}{RB_\vartheta}\right), \tag{4}$$

while the toroidal rotation of plasma related to the anomalous viscosity is ignored. The radial electric field in Eq. (4) is given by the following expression [5]:

$$E_r = E_r^{(\text{STAND})} - \frac{2.3en\sqrt{\varepsilon}E_\phi}{(1+\nu_e^*\varepsilon^{3/2})(1+\nu_e^{*1/3}+\nu_e^*)\sigma_\perp^{\text{apprax}}B_\vartheta}, \tag{5}$$

where

$$E_r^{(\text{STAND})} = \frac{T_i}{e}\left[\frac{d\ln n}{dr} + (1-k)\frac{d\ln T_i}{dr}\right] + B_\vartheta \bar{u}_\phi,$$

$$\sigma_\perp^{\text{apprax}} = \frac{\sigma_\perp^b}{1+\nu_i^*}, \tag{6}$$

$$\nu_i^* = \frac{qR\nu_i}{\sqrt{2T_i/m_i}\varepsilon^{3/2}}, \quad \sigma_\perp^b = \frac{3}{2}\frac{\sqrt{\varepsilon}m_i n\nu_i}{B_\vartheta^2}.$$

Results of numerical modeling. The model calculations showed that the main reason of the E_r profile variation in the plasma is a threefold increase in the ion temperature $T_i(0)$ taking place within the first millisecond of the lower hybrid heating. The numerical calculation allowed a density profile of the heat source Q_i, entering into the right-hand part of Eq. (2) describing the ion temperature, to be selected in good agreement with the experimental data (Fig. 1a). Equations (1)–(4) form a closed set. The calculations are performed upon selecting the profiles of heat and particle sources. In choosing the profile of neutral atoms (or the particle source), we took into account that charged particles may form from both hydrogen and an impurity since $Z_{\text{eff}} \approx 3$ [6].

An important point in the model calculation is selecting a proper character of dependence of the transport coefficient on the ω_s value. The initial $D(\omega_s)$ value was chosen so that the patterns of evolution of the concentration (n_e) and temperature ($T_{e,i}$) profiles would agree with the relevant experimental data [1]. The threshold values $\omega_{s1} = 1.2 \times 10^5$ s^{-1} and $\omega_{s2} = 2.5 \times 10^5$ s^{-1} corresponding to a jumplike drop in the transfer coefficients were selected as described in [5] based on the criterion of coincidence with experiment.

Figure 1b shows three profiles of the anomalous diffusion coefficient $D(\omega_s)$ determined at different moments of time: (*1*) at the initial instant in the stage of ohmic heating (29.5 ms) and (*2*) 1.5 and (*3*) 3.5 ms after the beginning of heating (31 and 33 ms, respectively). Figure 1c presents the E_r profiles, and Fig. 2 displays evolution of the n_e and $T_{e,i}$ profiles calculated for the same times (29.5, 31, and 33 ms). As seen from these data, the initial growth of the ion temperature within the first $\propto$1.5 ms after the beginning of the HF heating pulse leads eventually to a change in E_r at the plasma column center and to a sharp decrease in the diffusion coefficient, which results in the appearance of bending points in the $T_e(r)$ and $n_e(r)$ profiles at r = 3 and 5 cm, respectively.

Conclusions. 1. Self-consistent BATRAC code is well suited to model the process of ICC formation under the additional lower hybrid heating conditions in the FT-2 tokamak.

2. The ICC formation observed in experiment is due to the heating of ions at the center of the plasma column.

Acknowledgments. The work was supported by the Russian Foundation for Basic Research, project no. 98-02-18346.

REFERENCES

1. S. I. Lashkul *et al.*, in *Proceedings of the ICPP and 26th EPS Conference on Controlled Fusion and Plasma Physics, Maastricht, 1999*, Vol. 22C, p. 1729.
2. M. Yu. Kantor *et al.*, in *Proceedings of the 25th EPS Conference on Controlled Fusion and Plasma Physics, Praha, 1998*, p. 1566.
3. H. Biglari, P. H. Daimond, and P. W. Terry, Phys. Fluids B **2**, 1 (1990).
4. E. Syniakowsky, Plasma Phys. Controlled Fusion **40**, 597 (1998).
5. V. Rozhansky, A. Popov, and S. Voskoboynikov, in *Proceedings of the ICPP and EPS Conference on Controlled Fusion and Plasma Physics, Praha, 1998*, Vol. 22C, p. 1876.
6. S. I. Lashkul *et al.*, Zh. Prikl. Spektrosk. **54** (6), 887 (1991).

Translated by P. Pozdeev

Technical Physics Letters, Vol. 26, No. 10, 2000, pp. 870–872. Translated from Pis'ma v Zhurnal Tekhnicheskoĭ Fiziki, Vol. 26, No. 19, 2000, pp. 46–51.

A Diagram of the Stable Secular Motion of Ions Trapped in an RF Quadrupole Field in the Presence of Additional Harmonic Quadrupole Excitation

M. Yu. Sudakov

Ryazan State Radio Engineering Academy, Ryazan, Russia

e-mail: sudakov@qms.sotcom.ru

Received April 25, 2000

Abstract—The motion of ions trapped in an RF quadrupole field and subjected to an additional quadrupole excitation by a low-frequency harmonic signal was theoretically studied. A general diagram of the stable secular motion of these ions in the high-frequency regime was constructed for the three-dimensional and linear ion traps. © *2000 MAIK "Nauka/Interperiodica".*

Introduction. The motion of ions trapped in a periodic quadrupole field is characterized by a discrete spectrum of frequencies not representing simple harmonics of the fundamental or minimum frequency. The excitation of oscillations at these frequencies provides for an additional means of controlling the motion of trapped ions. The method of resonance excitation is used in the quadrupole mass spectrometry to separate undesired ions, excite endothermal reactions of trapped ions, and scan over the mass spectrum.

A recent theoretical study [1] showed that a resonance observed for the quadrupole excitation with an additional harmonic signal exhibits a parametric character. For this reason, the resonance takes place only for certain frequencies of the harmonic signal representing different orders of the parametric resonance. High-order resonances predicted in [1] were recently experimentally observed by Collings and Douglas [2] at frequencies close to the theoretical values.

According to [1], the additional quadrupole excitation changes the conditions for the stable motion of ions in the quadrupole field. The presence parametric resonances of various orders leads to splitting the stable motion domain into several bands of stability. In the case of additional excitation with a low-frequency harmonic signal, the splitting is most probable at the boundaries of the first band corresponding to the stability parameter $\beta = 0$ and $\beta = 1$. Small values of the parameter β correspond to the initial part of the stability diagram. Therefore, investigation of the splitting of the stability boundary $\beta = 0$ is of fundamental importance from the standpoint of ion confinement in the quadrupole field.

The purpose of this work was to develop a theoretical model describing the motion of ions trapped in a quadrupole field at small values of the stability parameter under conditions of an additional quadrupole excitation by a low-frequency harmonic field. The results were used to construct a diagram of stability for the motion of ions in the three-dimensional and linear ion traps [3] in the so-called high-frequency (HF) regime, in which no dc supply voltage is applied to the system.

Equation of the secular motion of ions. The oscillatory motion of an ion along the coordinate axis u in a quadrupole field in the presence of additional quadrupole excitation is described by the following equation:

$$\frac{d^2u}{d\xi^2} + [a + 2q\cos 2\xi + 2q'\cos(2\nu\xi + \alpha)]u = 0. \quad (1)$$

Here, $\xi = \Omega t/2$ is the time in dimensionless units; $\nu = \omega/\Omega$ is the ratio of the excitation frequency to that of the main RF field; α is the phaseshift between the two fields; and the dimensionless parameters a, q, and q' are functions of the coordinate, ion parameters, supply voltage, and electrode geometry in the trap. In particular, for a linear ion trap, these quantities can be expressed as

$$a_x = -a_y = \frac{8eU}{M\Omega^2 r_0^2}, \quad q_x = -q_y = \frac{4eV}{M\Omega^2 r_0^2}, \quad q'_x = -q'_y = \frac{4eV'}{M\Omega^2 r_0^2}; \quad (2.A)$$

for a three-dimensional trap, as

$$a_z = -2a_r = \frac{16eU}{M\Omega^2 r_0^2}, \quad q_z = -2q_r = \frac{8eV}{M\Omega^2 r_0^2}, \quad q'_z = -2q'_r = \frac{8eV'}{M\Omega^2 r_0^2}, \quad (2.B)$$

where $M = m_{ion}/Z$ is the ion mass to charge ratio (mass number), r_0 is the main geometric parameter of the

electrode system (field radius), U is the dc voltage, V is the ac component amplitude (0-peak) of the main supply voltage with the circular frequency Ω, and V' is the amplitude (0-peak) of the additional quadrupole excitation field with the circular frequency ω.

Variation of the quadrupole field by the low-frequency excitation is a slow process in comparison to the main RF supply voltage oscillations. The additional field can be considered as a slow variation of the parameter a. For small values of the dimensionless Mathieu parameters a and q, the ion oscillations are well described by a theory of the particle motion in a rapidly oscillating field [4]. The motion can be considered as a superposition of the small-amplitude oscillations $h(\xi)$ at the main RF frequency and a slow averaged (secular) motion $X(\xi)$:

$$u(\xi) = X(\xi) + h(\xi), \quad h(\xi) = \frac{q}{2}X(\xi)\cos 2\xi. \quad (3)$$

For the averaged motion, Eq. (1) yields the approximate equation

$$\frac{d^2X}{d\xi^2} + \left[a + \frac{q^2}{2} + 2q'\cos(2\nu\xi + \alpha)\right]X = 0, \quad (4)$$

which describes the secular oscillations of ions representing a slow motion with respect to the rapid quadrupole potential variations related the RF supply voltage.

Upon changing the time variable in Eq. (4) to the new value defined by the relationship $2\eta = 2\nu\xi + \alpha$, we arrive at an equation of Mathieu's type:

$$\frac{d^2X}{d\eta^2} + (A + 2Q\cos 2\eta)X = 0, \quad A = \frac{1}{\nu^2}\left(a + \frac{q^2}{2}\right), \quad Q = \frac{q'}{\nu^2}. \quad (5)$$

A diagram of stability for the solutions of Eq. (5) constructed on the plane of parameters (A, Q) represents the well-known Mathieu diagram [5].

Diagram of stability for the HF regime. The conditions of stable motion for ions in the presence of the additional excitation depend on the parameters a, q, and q'. Both linear and three-dimensional ion traps hold ions in the HF regime for which $a = 0$. In this case, the stability conditions are determined only by the values of q and q' or, according to Eq. (5), by the parameters $A = q^2/2\nu^2$ and $Q = q'/\nu^2$. The task of this work was to analyze the conditions of stable motion for a set of ions possessing different mass numbers.

As seen from Eq. (2), variation of the A and Q values for various ions is described by a parabola, which is not convenient in practice. A more convenient representation can be found taking into account that, while the A and Q values change with the mass number, the ratio

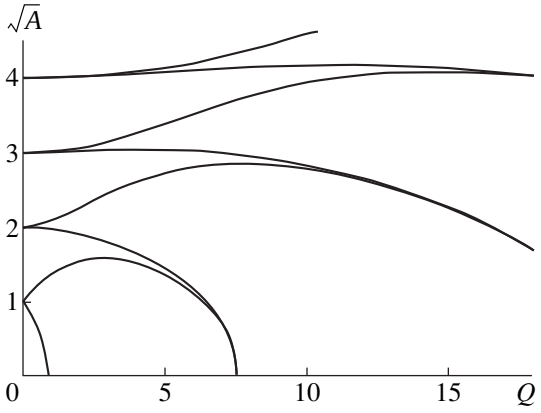

Fig. 1. A diagram of stable secular ion motion in the HF regime in the presence of additional low-frequency quadrupole excitation.

$\sqrt{A}/Q$ remains constant. According to Eq. (5), the slope of the "working" straight line is

$$\frac{\sqrt{A}}{Q} = \frac{q\nu}{q'\sqrt{2}} = \frac{\omega V}{\Omega V'\sqrt{2}}. \quad (6)$$

Thus, the working diagram is conveniently constructed in the plane of parameters (A, Q). An example of such a diagram is presented in Fig. 1, in which the working line may take any position. Although the ratio ω/Ω is small, the slope determined by Eq. (6) may acquire arbitrary positive values.

The diagram presented in Fig. 1 describes stable secular motion only in one coordinate. In the case of a linear ion trap, the dimensionless parameters q and q' for the oscillations along X and Y axes differ in sign. The sign does not influence the conditions of stable ion motion, since the parameter q enters into Eq. (5) as a square term. The negative sign of q' is equivalent to a change in the phase of $\cos 2\eta$ by π and reduces essentially to a change in the origin of time count. Thus, the diagrams of stable secular ion motion in a linear trap coincide for the oscillations in both transverse directions. Therefore, Fig. 1 presents the general diagram of stability for the HF regime in a linear trap.

In a three-dimensional trap, the values of q and q' for the radial oscillations of ions are twice as small as the axial parameters. For the HF regime in this trap, Eqs. (5) and (2) yield

$$A_z \approx 4A_r, \quad Q_z = 2Q_r. \quad (7)$$

Once the diagram of stable axial oscillations in the plane of parameters ($\sqrt{A_z}$, Q_z) is constructed, a diagram for the radial oscillations can be obtained by double expansion in both axes. This diagram is depicted by dashed curves in Fig. 2. Fully stable secular motions are represented by points in the regions of intersection

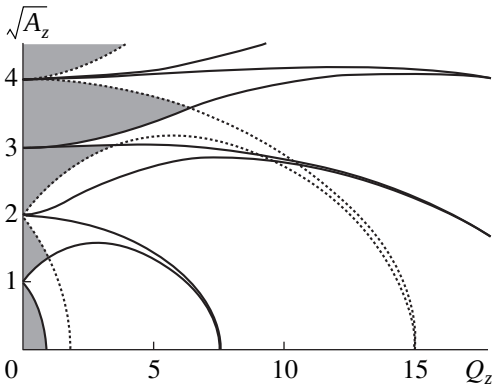

Fig. 2. A joint diagram of stable secular ion motion in a three- dimensional trap. The regions to full stability in all coordinates are indicated by cross-hatching.

of the stability domains for the axial and radial oscillations.

Conclusion. The HF regime is the main working mode for the ion trap operation. An additional harmonic quadrupole excitation at a frequency $\omega = \Omega/3$ is used in some commercial three-dimensional traps in order to increase the working mass range. Investigation of the conditions of stable ion motion in the presence of additional low-frequency quadrupole excitation is an important point in the context of extensive investigation of the linear ion trap [3]. The diagram of stability of a secular motion of ions in the HF regime obtained in this work is as convenient as the conventional Mathieu diagram is for ions in a quadrupole field. This knowledge opens up possibilities for the practical implementation of the quadrupole excitation of various types in novel devices for quadrupole mass spectrometry.

REFERENCES

1. M. Sudakov, N. Konenkov, D. J. Douglas, and T. Glebova, J. Am. Soc. Mass Spectrom. **11**, 10 (2000).
2. B. A. Collings and D. J. Douglas, Rapid Commun. Mass Spectrom. **14** (2000) (submitted).
3. J. M. Campbell, B. A. Collings, and D. J. Douglas, Rapid Commun. Mass Spectrom. **12**, 1463 (1998).
4. L. D. Landau and E. M. Lifshitz, *Course of Theoretical Physics*, Vol. 1: *Mechanics* (Nauka, Moscow, 1982; Pergamon, New York, 1988).
5. N. W. McLachlan, *Theory and Applications of Mathieu Functions* (Oxford Univ., Oxford, 1974).

Translated by P. Pozdeev

Technical Physics Letters, Vol. 26, No. 10, 2000, pp. 873–875. Translated from Pis'ma v Zhurnal Tekhnicheskoĭ Fiziki, Vol. 26, No. 19, 2000, pp. 52–58.

A Change in the Characteristics of Fluctuations of the Boundary Plasma Parameters in the FT-2 Tokamak upon Transition to the Improved Plasma Confinement Regime

E. O. Vekshina, P. R. Goncharov, S. V. Shatalin, V. N. Budnikov, L. A. Esipov, E. R. Its, and S. I. Lashkul

St. Petersburg State Technical University, St. Petersburg, 195251 Russia

Ioffe Physicotechnical Institute, Russian Academy of Sciences, St. Petersburg, 194021 Russia

Received May 24, 2000

Abstract—Processes in the boundary (near-wall) plasma of the FT-2 tokamak upon transition into an improved plasma confinement regime under the action of lower hybrid heating were studied by a refined plasma diagnostic method using multielectrode Langmuir probes. The experimental data show evidence of suppression of the correlation and coherency of fluctuations in the plasma density and the electric field strength as well as a reduction in the transverse particle transfer caused by the fluctuational drift flows. © *2000 MAIK "Nauka/Interperiodica".*

The results of numerous experiments indicate that peripheral wideband microscopic fluctuations are a common property of toroidal devices employing magnetic-field-confined plasma. Various methods of the plasma diagnostics reveal oscillations in the particle density, potential, and the electric and magnetic field strength, the character of these fluctuations (localization at the plasma column periphery, frequency range, relative intensity level, etc.) being rather similar in various systems. It is the microscopic turbulence development in the plasma that is commonly related to anomalous energy losses in tokamaks [1].

Experimental investigations of the peripheral processes in the tokamak plasma serve as a database necessary to create a reliable theoretical model describing anomalous transverse particles and energy transfer in tokamaks. These instigations are especially interesting in the context of the discovery and extensive study of the so-called improved plasma confinement conditions (H-regimes). This phenomenon confirmed a close relationship between peripheral processes (in particular, microturbulent behavior and related peripheral particle flows) and the plasma parameters in the main tokamak volume (see, e.g. [2]).

In the FT-2 tokamak (R = 55 cm; a = 0.08 m; B_{tor} = 2.2 T; I_{pl} = 22 kA), a transition to the improved plasma confinement regime was observed in experiments with additional HF plasma heating by electromagnetic waves in the lower hybrid frequency range (f = 920 MHz; $P_{HF} \le 150$ kW). The transition was especially clearly pronounced upon switching off the lower hybrid heating (LHH) [3].

The purpose of this work was to gain experimental data on the peripheral processes accompanying the transition to the improved plasma confinement regime in the FT-2 tokamak. Special attention was paid to the behavior of the fluctuational particle drift flows and to the evolution of the fluctuation characteristics.

The total particle flux in the boundary (near-wall) tokamak plasma is the sum of the diffusion flux with the density $\mathbf{\Gamma}_D = -D\mathrm{grad}n$ (D is the effective diffusion coefficient, n is the particle density) and the flux related to the drift of charged particles in crossed electric (**E**) and magnetic (**B**) fields. The latter flux can be represented as the sum of the quasistationary component $\mathbf{\Gamma}_0(t) = cn(t)[\mathbf{E}_0(t), \mathbf{B}]/B^2$ and the fluctuational component. The fluctuational fluxes can be related to correlated oscillations in the plasma density $n^{(\sim)}$ and electric field strength $\mathbf{E}^{(\sim)}$:

$$\mathbf{\Gamma}_{fl}(t) = \frac{c}{B^2}[\langle n^{(\sim)}(t)\mathbf{E}^{(\sim)}(t)\rangle, \mathbf{B}], \qquad (1)$$

where the angular brackets indicate averaging with respect to time.

The fluctuational flows represent one of the major mechanisms of the transverse transfer of particles in the peripheral region of toroidal setups. In particular, experiments on the FT-2 tokamak showed that these flows in the ohmic regime may account for up to 60–100% of the integral radial flux of particles [4]. Investigation of the characteristics of fluctuations in the boundary (near-wall) plasma, determination of the parameters of particle flows, and evaluation of their relative contribution to the total radial transfer under the LHH conditions required using a new diagnostic method, representing a refined probing technique described in [4].

1063-7850/00/2610-0873$20.00 © 2000 MAIK "Nauka/Interperiodica"

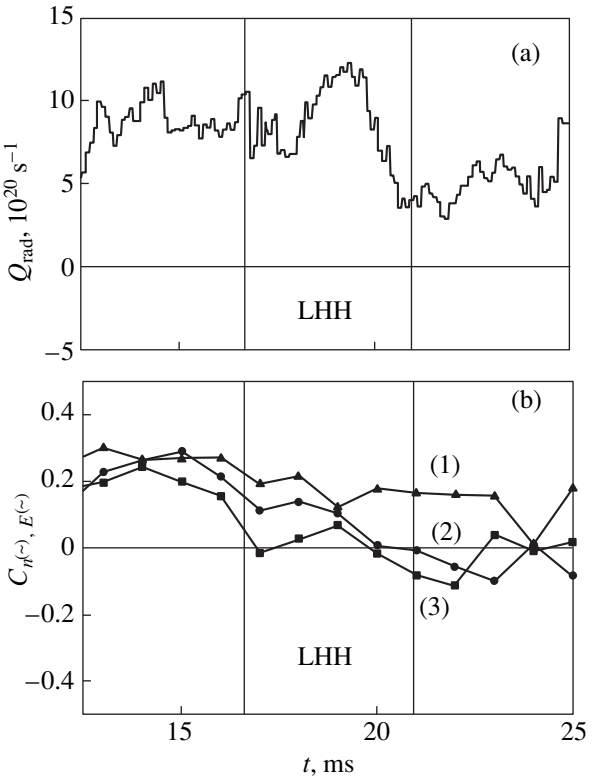

Fig. 1. Time evolution of (a) the integral radial fluctuational flux Q_{rad} of particles and (b) the correlation coefficient of the $n^{(\sim)}$ and $\mathbf{E}^{(\sim)}$ fluctuations in the region of diaphragm shadow measured for three angular positions Θ = 0 (*1*); 60° (*2*); 30° (*3*) (the poloidal angle Θ is measured from the outer tore contour in the direction of toroidal drift of electrons). Solid vertical lines indicate the period of lower hybrid heating pulse action.

The refined measuring system satisfied important requirements, including a wide working frequency range and the possibility of taking reliable measurements during the LHH pulse. The diagnostic method was based on using three mobile five-electrode Langmuir probes [4, 5] arranged in the same transverse cross section of the chamber so as to obtain data in the region of the diaphragm shadow fully covering the poloidal contour of the tore. The noise stability of the measuring circuit during the LHH pulse was ensured by the thorough symmetrization matching of the input impedances and by using wideband differential amplifier stages. The probe diagnostics allowed us to study the time evolution of local values of the electron temperature, plasma density, and potential; to measure fluctuations of these parameters in the frequency band of up to 500 kHz; and to determine the local densities of both quasistationary and fluctuational drift flows. The fluctuational flux component could be measured using either analog or digital equipment. The analog signal processing unit multiplied the fluctuational components of the saturated ion current to the probe and the potential difference between two symmetrically arranged floating electrodes, followed by averaging of product. The digital equipment was used to record the initial signals at a master clock frequency of 1 MHz.

During the experiments, we measured the local densities of fluctuational drift fluxes at an angular step of 20°–30° with respect to the poloidal angle and with a 1-mm step along the small radius *r*. The main body of data was gained with the analog equipment. Figure 1a shows the integral radial flux Q_{rad} calculated using these data for r = 8 cm. As is seen, the transition to the improved plasma confinement regime upon switching on the LHH is accompanied by a decrease in the fluctuational flux approximately by half as compared to that in the ohmic heating regime. An approximate twofold increase in the energy lifetime in the improved plasma confinement regime with LHH as compared to the ohmic heating was previously reported in [6]. A decrease in the fluctuational flows is probably an important factor responsible for the observed effects.

The spectral and correlation characteristics of fluctuations in the plasma density and electric field strength were studied with the aid of the digital equipment. By these data, we have calculated the statistical correlation coefficient $C_{n^{(\sim)}E^{(\sim)}}$ for the oscillations of these parameters, which characterizes time evolution of the fluctuational flow of particles, and the mutual coherency function $\gamma^2(f)$ describing contributions of various frequencies:

$$C_{n^{(\sim)}, E^{(\sim)}} = \frac{\langle n^{(\sim)}E^{(\sim)}\rangle - \langle n^{(\sim)}\rangle\langle E^{(\sim)}\rangle}{\sqrt{\langle n^{(\sim)2}\rangle - \langle n^{(\sim)}\rangle^2}\sqrt{\langle E^{(\sim)2}\rangle - \langle E^{(\sim)}\rangle^2}}, \quad (2)$$

$$\gamma^2(f) = \frac{\left|n^{(\sim)}(f)E^{(\sim)}(f)\right|^2}{\left|n^{(\sim)}(f)\right|^2\left|E^{(\sim)}(f)\right|^2}, \quad (3)$$

where $n^{(\sim)}(f)$ and $E^{(\sim)}(f)$ are the Fourier components of fluctuations in the plasma density and the electric fields strength.

The $C_{n^{(\sim)}E^{(\sim)}}$ and $\gamma^2(f)$ values were calculated using the results of measurements of the fluctuations $n^{(\sim)}$ and $\mathbf{E}^{(\sim)}$ in the frequency band from 10 to 500 kHz. The measurements were performed on the outer side of the toroidal plasma column at a 30° step within a poloidal angle interval (±60°) symmetric relative to the equatorial plane. Figure 1b illustrates the behavior of the correlation coefficient. The correlation coefficient of fluctuations in the plasma density and electric field strength for the ohmic regime has a characteristic value of about 0.3 and virtually drops to zero upon the LHH pulse. This trend is manifested at all values of the poloidal angle for which the measurements were taken.

Behavior of the coherency function in the space region probed exhibits similar trends. For example, Fig. 2 shows the time evolution of this function at a point on the outer equatorial line of the tore. In the stationary stage of discharge in the ohmic regime, the

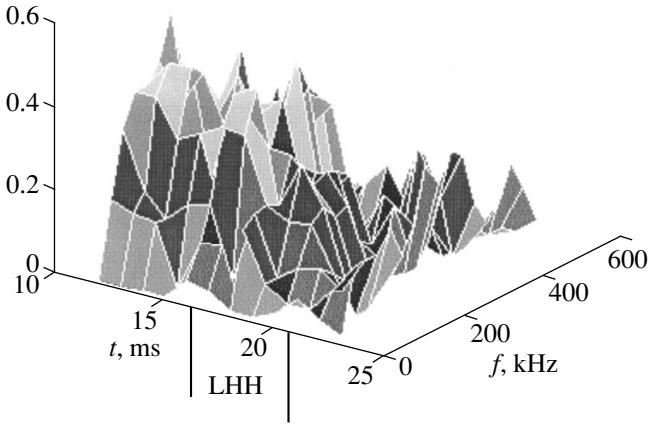

Fig. 2. Time evolution of the local coherency spectrum of the $n^{(\sim)}$ and $\mathbf{E}^{(\sim)}$ fluctuations measured in the region of diaphragm shadow for $\Theta = 0$.

coherency function has a typical value of 0.5 in the 10- to 200-kHz frequency band and drops to 0.1–0.2 for the harmonics above 200 kHz. A transition to the improved plasma confinement regime upon the LHH pulse is accompanied by a drop of the coherency function to 0.1 in the entire frequency range.

The results of our experiments demonstrated some decrease in the fluctuations of plasma parameters in the H-regime, but this effect was observed not for values of the poloidal angle. The inner poloidal contour showed a considerable decrease in the level of fluctuations, whereas the amplitude of fluctuations on the outer side of the tore exhibited no significant changes and even increased at some points. It should be noted that this behavior of the peripheral turbulence upon switching off the LHH pulse was also revealed by reflectometric data [7]. Therefore, the effect of the fluctuation suppression has a local character, while a decrease in the coherency function and the correlation coefficient was observed at all points in the probed region.

Thus, a transition to the improved plasma confinement regime in the FT-2 tokamak upon switching off the LHH pulse is accompanied by a significant decrease in the transverse particle transfer by the fluctuational drift flows in the peripheral region. This decrease is related primarily to the phenomenon of the suppressed correlation of the plasma density and electric field strength fluctuations and to a decrease in the coherency of fluctuations. The experimental observations suggest that these effects play an important role in the mechanism of transition to the improved plasma confinement regime.

Acknowledgments. This work was supported by the Ministry of Higher and Professional Education of the Russian Federation (grant upon the 1997 year competition) and by the Russian Foundation for Basic Research (project no. 97-02-18119).

REFERENCES

1. P. C. Liewer, Nucl. Fusion **25** (5), 543 (1985).
2. P. E. Stott and The JET Team, J. Nucl. Mater. **162**–**164**, 3 (1989).
3. V. N. Budnikov, V. V. D'yachenko, L. A. Esipov, *et al.*, Pis'ma Zh. Éksp. Teor. Fiz. **59** (10), 651 (1994) [JETP Lett. **59**, 685 (1994)].
4. L. A. Esipov, I. E. Sakharov, E. O. Chechik, *et al.*, Zh. Tekh. Fiz. **67** (4), 48 (1997) [Tech. Phys. **42**, 367 (1997)].
5. A. N. Levitskiĭ, I. E. Sakharov, and S. V. Shatalin, Prib. Tekh. Éksp. **5**, 153 (1992).
6. V. N. Budnikov, V. V. D'yachenko, L. A. Esipov, *et al.*, Pis'ma Zh. Tekh. Fiz. **23** (1), 52 (1997) [Tech. Phys. Lett. **23**, 32 (1997)].
7. V. N. Budnikov, V. V. D'yachenko, L. A. Esipov, *et al.*, Fiz. Plazmy **21** (10), 865 (1995) [Plasma Phys. Rep. **21**, 817 (1995)].

Translated by P. Pozdeev

Technical Physics Letters, Vol. 26, No. 10, 2000, pp. 876–878. Translated from Pis'ma v Zhurnal Tekhnicheskoĭ Fiziki, Vol. 26, No. 19, 2000, pp. 59–65.

Special Features of the Effect of Oversized Impurities on the Cascade Development in α-Iron Alloys Containing Special Carbides

V. V. Rybin, Yu. V. Trushin, F. Yu. Fedorov, and V. S. Kharlamov

"Prometeĭ" Central Research Institute

Ioffe Physicotechnical Institute, Russian Academy of Sciences, St. Petersburg, 194021 Russia

St. Petersburg State Technical University, St. Petersburg, 195251 Russia

Received June 8, 2000

Abstract—We consider the behavior of an α-iron alloy containing special molybdenum and tungsten carbides (MoC and WC) and oversized impurity atoms (Mo and W) in the solid solution. The effects of molybdenum and tungsten on the development of ballistic (cascade) processes in the alloy under reactor irradiation conditions have been studied by computer simulation methods to assess the possibility of substituting W for Mo in the alloy to obtain low-activated steels. © *2000 MAIK "Nauka/Interperiodica".*

In order to develop low-activated steels for various units of radiation equipment, it is necessary to replace alloying elements forming long-living radioactive isotopes (e.g., Mo having a halflife longer than that of iron isotopes) with different atoms (e.g., tungsten) of comparable atomic radius (R_{Mo} = 1.245 Å against R_W = 1.255 Å) producing isotopes cooling faster than the iron isotopes under the same irradiation conditions. Previously [1], we studied the effect of oversized impurities on the radiation resistance of α-iron alloys. The investigation of various stages in the radiation damage development in these alloys needs a more detailed analysis of the ballistic (cascade development) processes, the effects of Mo and W in this stage of irradiation, and the consequences of interaction between the atomic collision cascades with molybdenum and tungsten carbides.

Although atoms of the two refractory metals, molybdenum and tungsten, possess almost equal dimensions, their atomic weights (m_W = 183.8 amu against m_{Mo} = 95.94 amu) differ by a factor of m_W/m_{Mo} = 1.916, which results in a considerable (almost twofold) difference in the energy transferred in the atomic collision events with iron atoms or neutrons during the reactor irradiation of steels containing molybdenum or tungsten admixtures.

However, there is another physical factor also significantly influencing behavior of these metals. As is known, the interaction cross section of colliding particles is determined by the dependence of the interatomic interaction potential on the distance between particles [2]. These calculations may be based on the so-called universal Ziegler–Biersack–Littmark (ZBL) potential [3]. Figure 1 shows the pairwise ZBL potentials for the Fe–Mo, Fe–W, Mo–Mo, and W–W interactions, which can be used to estimate the characteristic radii $r_{Fe, K}$ for the interaction of iron with molybdenum (K = Mo) or tungsten (K = W) in the collision cascades. As seen from Fig. 1, this radius (determining the interaction cross section $\sigma_{Fe, K} = \pi r_{Fe, K}^2$) at various energies is always greater for the interaction of iron with tungsten than with molybdenum.

Thus, the efficiency of defect formation in the stage of cascade development in iron alloys with W or Mo is determined by the interplay of two opposite factors: (i) the greater atomic weight of tungsten in comparison with molybdenum (implying less favorable energy transfer to the former) and (ii) the greater cross section for the iron interaction with tungsten than with molybdenum (implying a greater probability of the iron interaction with tungsten).

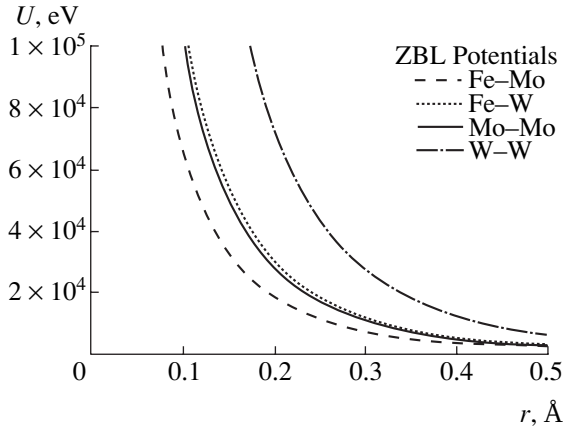

Fig. 1. The ZBL potentials for Fe–Mo, Fe–W, Mo–Mo, and W–W interactions.

1063-7850/00/2610-0876$20.00 © 2000 MAIK "Nauka/Interperiodica"

Let us evaluate the number of defects N^K (KC) per unit volume of carbide (KC) formed in a steel containing impurity atoms K = W, Mo:

$$N^K(KC) = \rho_{nc}^K(KC)\varphi_{Fe}(E_{Fe})(\pi r_{Fe,K}^2)\nu_K(E_K), \quad (1)$$

where $\rho_{nc}^K(KC)$ is the nuclear density of metal K in the carbide KC; $\varphi_{Fe}(E_{Fe})$ is the fraction of Fe atoms with the energy E_{Fe}; and $\nu_K(E_K)$ is the cascade function for the atoms of metal K in the corresponding carbide, with the kinetic energy E_K transferred to atom K. The cascade function can be expressed by the Kinchin–Pease formula [4]

$$\nu_K(E_K) = \frac{E_K}{2\varepsilon_d^K}, \quad (2)$$

where ε_d^K is a threshold energy for the displacement of atom K in the corresponding carbide. The energy E_K can be estimated using an expression for the maximum energy [2] transferred to the K atom upon collision with the Fe atom possessing the kinetic energy E_{Fe}:

$$E_K = \frac{4m_{Fe}m_K}{(m_{Fe}+m_K)}E_{Fe} = \lambda_K E_{Fe}. \quad (3)$$

Let us use Eqs. (1)–(3) to determine a ratio of the number of defects formed by Fe atoms moving with the energy E_{Fe} in the tungsten carbide $N^W(WC)$ to the number of defects formed by the same Fe atoms in the molybdenum carbide $N^{Mo}(MoC)$:

$$\frac{N^W(WC)}{N^{Mo}(MoC)} = \frac{\rho_{nc}^W(WC)}{\rho_{nc}^{Mo}(MoC)}\frac{\varepsilon_d^{Mo}}{\varepsilon_d^W}\frac{r_{Fe,W}^2}{r_{Fe,Mo}^2}\frac{\lambda_W}{\lambda_{Mo}}, \quad (4)$$

where $\lambda_W/\lambda_{Mo} = 0.714$. Let us introduce the notation $\beta = (r_{Fe,W}^2/r_{Fe,Mo}^2)(\lambda_W/\lambda_{Mo})$ and determine this parameter using the Fe–W and Fe–Mo interaction radii estimated from Fig. 1 for various energies. Table 1 gives the β values calculated for three kinetic energies E_{Fe}. Assuming that the ratios of nuclear densities and displacement threshold energies are on the order of unity, we may conclude from these estimates for β that the level of defect formation in steels containing tungsten is higher than in steels with molybdenum.

In order to study special features of the effect of Mo and W on the properties of steel under reactor irradiation conditions, we have performed a computer simulation of the atomic collision cascades produced by the primary knock-on Fe atoms with an energy of 1 MeV in the following targets: (i) homogeneous $Fe_{0.9}Mo_{0.1}$ and $Fe_{0.9}W_{0.1}$ alloys and (ii) three-layer Fe/carbide/Fe structures representing iron containing a 500-Å-thick carbide (MoC or WC) layer. The modeling was performed using a TRIRS program package [5, 6] intended for calculating the distribution of point defects produced by the atomic collisions cascades in multilayer targets. The program implements the Monte Carlo simulation method in the pairwise collision approximation. The results of these calculations are presented in Fig. 2.

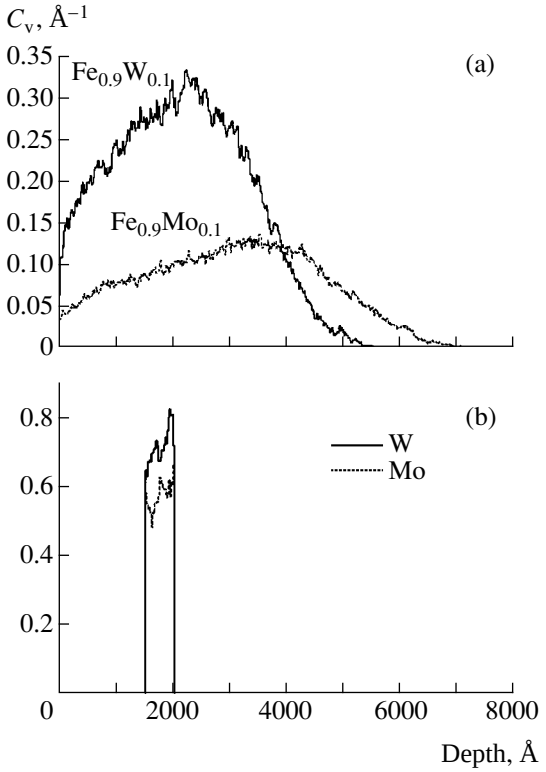

Fig. 2. Depth profiles of W and Mo vacancies produced by atomic collision cascades in (a) homogeneous $Fe_{0.9}Mo_{0.1}$ and $Fe_{0.9}W_{0.1}$ alloys and (b) three-layer Fe/MoC/Fe and Fe/WC/Fe targets.

Figure 2a shows the depth profiles of molybdenum (or tungsten) vacancies produced by the atomic collision cascades in homogeneous targets. The patterns of defect distribution show that the same collision cascade produces a much greater number of point defects in the tungsten subsystem than in the molybdenum subsystem.

Figure 2b shows analogous depth profiles of the Mo and W vacancies in the three-layer Fe/carbide/Fe targets. This figure also indicates that the number of tungsten vacancies in the tungsten carbide is greater than the number of molybdenum vacancies in the corresponding carbide. Taking the ratio of the numbers of

Table 1. The values of the defect production efficiency parameter β for various energies of Fe atoms

E_{Fe}, keV	β
20	1.136
60	1.321
100	1.421

Table 2. The ratio of the numbers of tungsten and molybdenum vacancies at various depths in the corresponding carbides

Depth, Å	C_v^W/C_v^{Mo}
1500	1.16
1750	1.15
2000	1.31

tungsten and molybdenum vacancies (C_v^W/C_v^{Mo}) at various depths in the corresponding carbide, we obtain the pattern presented in Table 2.

A comparison of data presented in Tables 1 and 2, we may conclude that estimates of both the cascade efficiency (Table 1) and the total number of defects produced by displaced target atoms (Table 2) show the same general trends. The results of both calculations demonstrate that the presence of tungsten favors an increase in the efficiency of cascade development in the matrix material from the standpoint of radiation damage production. This situation is explained both by the greater weight of tungsten atoms ($m_W = 1.916m_{Mo}$) and by the cross section of the interaction (scattering) of iron atoms being greater for their collisions with tungsten atoms than with molybdenum atoms.

A comparative analysis of these features of the effect of molybdenum and tungsten atoms on the development of atomic collision cascades leads to the conclusion that the near-surface regions of tungsten carbide are subjected to a greater radiation damage, since the number of radiation defects produced in this carbide is greater than in molybdenum carbide. In turn, the ballistic damage in the near-surface layers of carbides, in combination with diffusion processes, leads to gradual dissolution of the precipitates. We may suggest that the size of tungsten carbides (featuring more rapid decomposition under the action of atomic collision cascades) may drop below the critical level and dissolve in the matrix, while the molybdenum carbides will survive.

The results of calculation of the atomic collision cascades for the primary knock-on Fe atoms with an energy of 350 keV showed generally the same trends in dependence on the type of oversized impurity (W against Mo). We have also established a relationship between the level of defect (vacancy) production in Mo and W carbides on the precipitate size (carbide layer thickness). For example, the number of defects (vacancies) observed for a carbide layer thickness below 200 Å is greater in Mo carbide than in W carbide. When the carbide layer thickness exceeds 200 Å, the damage becomes greater in tungsten carbides than in molybdenum carbides, as described above. This effect can be explained by the greater number of tungsten atoms contained in thick carbide layers and, hence, by a greater number of these atoms involved in the cascade processes in thick carbide layers than in thin layers. Since W atoms possess a greater interaction cross section as compared to that of Mo atoms, the former (see Fig. 1) produce a greater number of defects in the carbide layer, leading to a faster tungsten carbide decomposition in comparison with the analogous process in MoC.

Thus, the results of computer simulation of the atomic collision cascades initiated by the reactor irradiation show that tungsten carbides may decompose faster than molybdenum carbides in the ballistic stage of the radiation damage, which is explained by certain features of the interaction potential of tungsten atoms (with Fe and W, see Fig. 1). As a result, the size of tungsten carbide precipitates may decrease to within the subcritical region and dissolve in the matrix, while the molybdenum carbides will survive.

Acknowledgments. The authors are grateful to A.A. Vasil'ev for fruitful discussions.

The work was supported by the Russian Foundation for Basic Research, project nos. 98-02-18369 and 99-02-17990.

REFERENCES

1. V. V. Rybin and Yu. V. Trushin, Pis'ma Zh. Tekh. Fiz. **23** (8), 77 (1997) [Tech. Phys. Lett. **23**, 326 (1997)].
2. M. W. Thompson, *Defects and Radiation Damage in Metals* (Cambridge Univ., Cambridge, 1969; Mir, Moscow, 1971).
3. J. F. Ziegler, J. P. Biersack, and U. Littmark, *The Stopping and Range of Ions in Solids* (Pergamon, New York, 1985).
4. G. A. Kinchin and R. S. Pease, Rep. Prog. Phys. **18**, 1 (1955).
5. B. Ya. Ber, E. E. Zhurkin, A. V. Merkulov, *et al.*, Zh. Tekh. Fiz. **66** (3), 54 (1996) [Tech. Phys. **41**, 261 (1996)].
6. Yu. V. Trushin, B. J. Ber, V. S. Kharlamov, and E. E. Zhurkin, J. Nucl. Mater. **233**–**237**, 991 (1996).

Translated by P. Pozdeev

Technical Physics Letters, Vol. 26, No. 10, 2000, pp. 879–881. Translated from Pis'ma v Zhurnal Tekhnicheskoĭ Fiziki, Vol. 26, No. 19, 2000, pp. 66–71.

Propagation of Ultrashort RF Pulses in a Polluted Atmosphere

V. A. Ivanchenko and V. V. Nikolaev

Research Institute of Mechanics and Physics, Saratov State University, Saratov, Russia

Received March 17, 2000

Abstract—The effect of absorption and dispersion on the spectral characteristics and the shape of ultrashort RF pulses propagating in a polluted atmosphere is studied theoretically. The frequency band occupied by the pulses essentially covers the rotational spectrum of gas molecules encountered in a real atmosphere. © *2000 MAIK "Nauka/Interperiodica".*

Previously [1, 2], we demonstrated possibilities for the radar detection and characterization of gaseous pollutants in the atmosphere probed in the range of frequencies covering the rotational spectra of typical pollutants in the millimeter and the submillimeter wave band [3]. It was assumed that the bandwidth of the probing pulses is much smaller than the carrier frequency. Compared with the traditional narrow-band radar probing, a superwide-band method employing ultrashort pulses (USPs) enables one to obtain a larger amount of data and, more importantly, to improve their quality as to the degree of reliability, resolution, etc. [4]. These merits are also valuable to the remote monitoring of the chemical composition of the lower atmosphere. The present study examines certain features of the USP propagation in a polluted atmosphere, the spectrum of the pulses covering the rotational spectrum of gas molecules.

The bandwidth of a USP may be on the order of or even much greater than the linewidth of the resonant absorption in gases under real conditions. Consequently, the shape of a probing pulse is affected by absorption and dispersion, which gives additional information on the monitored medium.

Assume that the probed medium is linear and uniform; i.e., the absorption coefficient χ and the permittivity ε are functions of the frequency only, being independent of the spatial coordinates and the field amplitude. Therefore, spectral components of a signal propagate independently of each other so that the shape of a pulse detected at a distance x from the transmitter can be represented as

$$y(x, t) = \frac{1}{\pi}\int_0^\infty |Y(x, \omega)|\cos[\omega t + \varphi(x, \omega)]d\omega,$$

where $|Y(x, \omega)| = |Y(0, \omega)|\exp[-\chi(\omega)x/2]$ and $\varphi(x, \omega) = \varphi(0, \omega) - \omega x\sqrt{\varepsilon(\omega)}/c$, with c being the speed of light in a vacuum and $Y(0, \omega)$ being the Fourier image of the initial pulse:

$$Y(0, \omega) = \int_{-\infty}^{\infty} y(0, t)\exp(-i\omega t)dt,$$

$$\varphi(0, \omega) = \arctan\left(\frac{\mathrm{Im}Y(0, \omega)}{\mathrm{Re}y(0, \omega)}\right).$$

Below, the function $\psi(x, \omega) = \varphi(x, \omega) + \omega x/c$ is called the phase spectrum of the $y(x, t)$ signal.

In practice, the shape and parameters of spectral lines in gases are governed by intermolecular interactions, since the probing radiation attenuation and the Doppler effect can be neglected when operating in the microwave band. Assume that any molecule of the absorbing gas has two nondegenerate energy levels and that the concentration of the absorbing gas is much lower than that of the background gas. Then, the frequency dependence of the absorption coefficient of a gas mixture has the form

$$\chi(\omega) = \frac{1}{L}\left[\frac{2\omega}{\pi}\mathrm{Re}\int_0^\infty \Phi(\tau)\cos(\omega\tau)d\tau\right], \qquad (1)$$

where L is a constant measured in the units of length and $\Phi(\tau)$ is the correlation function [5]. We must allow for multiparticle interaction, since it may have a profound effect on the shape and parameters of the spectral lines if the pressure is 1 atm or higher. In the adiabatic approximation, the form of the correlation function is provided by [5]

$$\Phi(\tau) = \exp[i\omega_0\tau + N\overline{v\sigma(\tau, v)}], \qquad (2)$$

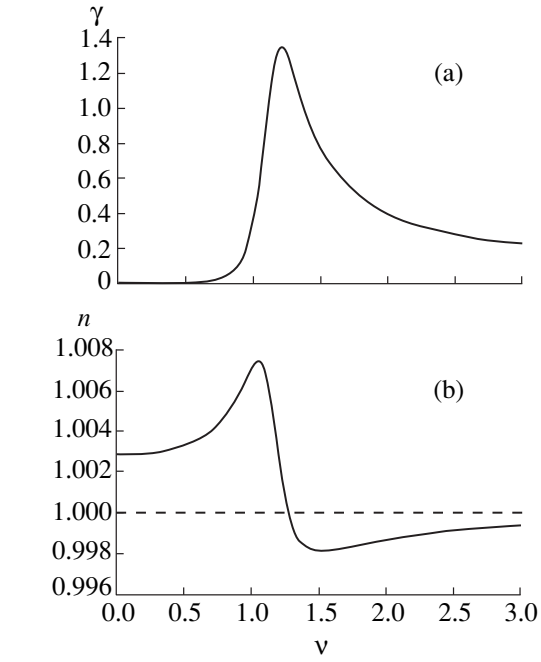

Fig. 1. Frequency dependences of (a) the dimensionless absorption coefficient and (b) the refractive index.

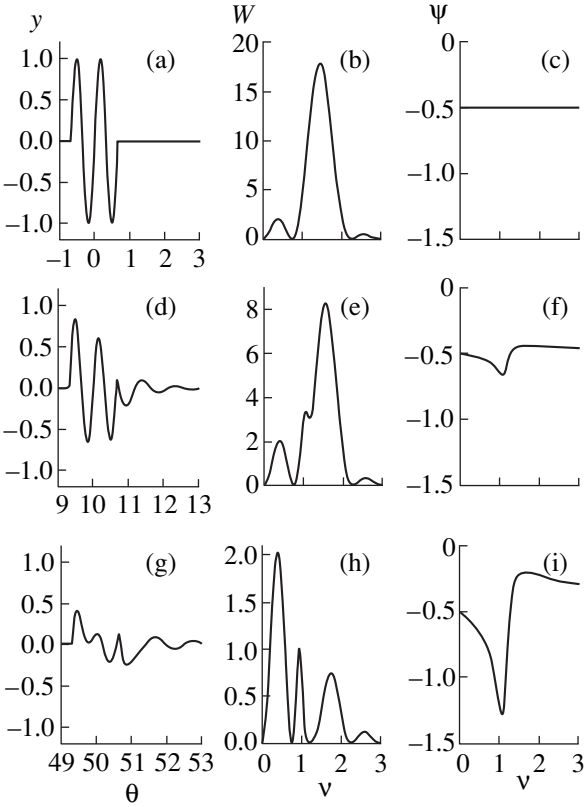

Fig. 2. Evolution of a USP in the course of propagation: (a, d, g) the pulse shape; (b, e, h) the energy spectral density; and (c, f, i) the phase spectrum at different distances from the transmitter. Panels (a–c) refer to the output of the transmitter; panels (d–f), to the distance $x = 1L$; and panels (g–i), to the distance $x = 5L$. The energy spectral density is normalized to $1/\omega_0^2$, and the phase spectrum, to π.

with

$$\sigma(\tau, v) = 2\pi\int_0^\infty b\,db\int_{-\infty}^{\infty}\left[\exp\left(iC\int_\zeta^{\zeta+\tau}\frac{dt}{(b^2+v^2t^2)^{p/2}}\right)-1\right]d\zeta. \quad (3)$$

Here, $\omega_0 = (E_b - E_a)/\hbar$, with E_a and E_b being the energies of the lower and the higher level, respectively, and $\hbar$ being the Planck constant; N is the concentration of the background gas; v is the velocity of the relative particle motion; and C and p are constants. The overbar denotes averaging over velocities.

Let us introduce the dimensionless variables $\gamma = L\chi$, $\nu = \omega/\omega_0$, $\theta = \omega_0 t/(2\pi)$, and $\rho = b_0^3 N$. Here, t is the time and b_0 is the Weisskopf radius:

$$b_0 = \left\{\frac{\sqrt{\pi}C}{\bar{v}}\left[\Gamma\left(\frac{p-1}{2}\right)/\Gamma\left(\frac{p}{2}\right)\right]\right\}^{\frac{1}{p-1}},$$

where $\bar{v}$ is the average velocity of the relative particle motion. Using the Kramers–Kronig relationships, we may readily express the refractive index n as a function of the dimensionless absorption coefficient γ:

$$n(\nu) - 1 = \frac{1}{2\pi^2 g}\wp\int_0^\infty\frac{\gamma(\nu')d\nu'}{\nu'^2-\nu^2},$$

where $g = \omega_0 L/(2\pi c)$ and the symbol $\wp$ denotes the Cauchy principal value.

Figure 1 shows the absorption coefficient and the refractive index as functions of the frequency. The former function was computed from formulas (1)–(3). The relative velocities of gas molecules were assumed to equal the average velocity. Also, we set $\bar{v} = b_0\omega_0/(2\pi)$, $\rho = 0.3$, $p = 6$, and $g = 10$.

Let a probing USP be a rectangular RF pulse of height 1 and length equal to two periods of the carrier (Fig. 2a), the carrier frequency being $\Omega_0 = 1.5\omega_0$. The energy spectral density W and the phase spectrum ψ of the pulse (Figs. 2b, 2c) are described by the formulas

$$W(0, \omega) = \frac{1}{\Omega_0^2}\left[\frac{\sin[2\pi(1-\omega/\Omega_0)]}{1-\omega/\Omega_0} - \frac{\sin[2\pi(1+\omega/\Omega_0)]}{1+\omega/\Omega_0}\right]^2,$$

$$\psi(0, \omega) = \varphi(0, \omega) = -\pi/2.$$

Figures 2d–2i show evolution of the shape and the spectrum of the USP in the course of propagation.

To sum up, USPs change their shape as they propagate in a medium with absorption and dispersion due to pronounced spectral widening. This effect can serve as a new source of information in the remote probing of the lower atmosphere.

REFERENCES

1. V. A. Ivanchenko and V. V. Nikolaev, Pis'ma Zh. Tekh. Fiz. **23** (24), 1 (1997) [Tech. Phys. Lett. **23**, 943 (1997)].
2. V. A. Ivanchenko and V. V. Nikolaev, Pis'ma Zh. Tekh. Fiz. **25** (3), 73 (1999) [Tech. Phys. Lett. **25**, 114 (1999)].
3. V. V. Efremenko and N. N. Markina, Radiotekh. Élektron. (Moscow) **38** (10), 1822 (1993).
4. I. Ya. Immoreev, Élektromagn. Volny Élektron. Sist. **2** (1), 81 (1997).
5. S. Chen and M. Takeo, Rev. Mod. Phys. **29** (1), 20 (1957).

Translated by A. Sharshakov

Technical Physics Letters, Vol. 26, No. 10, 2000, pp. 882–884. Translated from Pis'ma v Zhurnal Tekhnicheskoĭ Fiziki, Vol. 26, No. 19, 2000, pp. 72–76.

On the Measurement of Spatially-Resolved Energy Characteristics of a High-Power Laser Radiation

A. P. Solov'ev, O. V. Zyuryukina, and M. I. Perchenko

Research Institute of Mechanics and Physics, Saratov State University, Saratov, Russia

Received March 12, 1999; in final form, April 13, 2000

Abstract—Behavior of a signal of the Rayleigh scattering of a laser radiation in air was studied depending on the parameters of an ultrasonic wave excited in the region of observation. It is shown that the presence of an ultrasonic wave in this region provides for a spatial resolution in the direction of observation with respect to the energy parameters of the laser radiation from the Rayleigh scattering measured at the sound frequency. The minimum intensity of laser radiation and the spatial resolution are estimated for a particular frequency and intensity of sound. © *2000 MAIK "Nauka/Interperiodica".*

In the development of lasers and in the application of these devices in processing systems and research facilities, an important role belongs to contactless probing of a spatial distribution of the energy characteristics of a high-power laser radiation [1–4]. In this case, the introduction of any sensing elements in the radiation pathway is undesirable. Previously [5], the feasibility of nonperturbing measurements of the laser radiation parameters using the Rayleigh scattering data was demonstrated both theoretically and experimentally. It was found that the minimum measured radiation intensity of a He–Ne laser is 10 mW/cm^2 for an observation volume of $V_R \cong 2 \times 10^{-3}$ cm^3 within a solid angle of 2.6×10^{-2} sr. In the diagnostics of laser radiation with a complex structure, the main disadvantage of this method is the lack of spatial resolution in the direction of observation. This disadvantage can be removed by exciting an ultrasonic wave in the region of observation and recording a component of the Rayleigh scattering signal generated at the ultrasonic frequency.

Consider the scheme of interaction presented in Fig. 1. In this scheme, the ultrasonic wave travels through the region of observation of a photodetector. For definiteness, we assume that the wave propagates perpendicularly to the axes of both the receiver and the laser radiation. An ultrasonic wave with the frequency f propagating in the medium creates an additional sound pressure p relative to the mean pressure p_0. For a plane wave traveling along the y axis, the sound pressure takes the form

$$p(y, t) = \bar{p}_A \exp(-j2\pi(ft - y/\Lambda)). \quad (1)$$

Here, $p_A = (2I\rho_0 v)^{1/2}\exp(-\alpha y)$ is the wave amplitude, I is the intensity of sound at $y = 0$, ρ_0 is the unperturbed density of medium, v is the velocity of sound, α is the sound attenuation factor, and Λ is the sound wavelength [6]. The pressure wave is accompanied by a density wave ρ with $\bar{p}_A / \bar{p}_0 = \rho/\rho_0 = n/n_0 = m$, where n_0 is the concentration of gas molecules at atmospheric pressure and n is the amplitude of the variable component of concentration arising during the propagation of the sound pressure wave.

The Rayleigh scattering power W_R is proportional to the concentration of gas molecules; therefore, the Rayleigh scattering signal also contains a variable component at the ultrasound frequency. The photoreceiver *2* sums up instantaneous values of the Rayleigh signal power W_S at the ultrasound frequency arriving from sections with phase $2\pi y/\Lambda$. Let d_S be the transverse

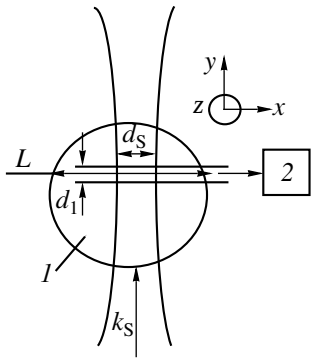

Fig. 1. The scheme of measurements with the ultrasonic wave: (*1*) laser beam cross section; (*2*) photodetector; (k_S) the wave vector of the ultrasonic wave; (d_1) dimension of the observation channel along the axis of the sound wave; (d_S) diameter of the ultrasonic wave in the region of measurements; (L) the dimension of the laser beam along the direction of observation. The direction of the laser radiation is perpendicular to the plane of the figure.

1063-7850/00/2610-0882$20.00

dimension of the ultrasound beam and d_1 and d_2 are dimensions of the observation channel cross section along and across the ultrasound propagation direction, respectively (i.e., along the y and z axes in Fig. 1). Then, for the optimum relationship of $d_2 \le d_S$, the amplitude of the variable component of the Rayleigh scattering power within a solid angle Ω can be written as

$$W_S = \frac{\Lambda}{\pi d_1}\sigma n_0 \Omega V I_0 \sin\left(\frac{\pi d_1}{\Lambda}\right)\exp(-\alpha y)\frac{\sqrt{2I\nu\rho_0}}{p_0} = W_R \frac{m\Lambda}{\pi d_1}\sin\left(\frac{\pi d_1}{\Lambda}\right)\frac{V}{V_R}\exp(-\alpha y), \quad (2)$$

where I_0 is the intensity of laser radiation in the region of observation at a given wavelength λ, y is the distance from the sound source to the probed (take-off) volume, σ is the Rayleigh cross section proportional to λ^{-4}, $V \cong d_1 d_2 d_S$ and $V_R \cong d_1 d_2 L$ are the probed volumes for the variable and constant power components, and L is the laser beam dimension in the direction of observation. One can see that, for $d_S < L$, the probed volume for the variable component is limited in the direction of observation by the width d_S of the ultrasound beam rather than by the laser beam dimension. By focusing the ultrasonic wave, the beam width can be reduced to $d_S \cong 2\Lambda$.

Figure 2 shows the sound attenuation factor α in dry and humid air (with a relative humidity of 40 and 100%) and the minimum dimension of the probed volume along the direction of observation $d_S = 2\Lambda$ as functions of the sound frequency for the scheme of measurements presented in Fig. 1. Using these data, we can choose the sound frequency depending on the required resolution across the laser beam. The attenuation at the chosen frequency depends on the distance from the sound source to the region of observation, that is, on the diameter d_L of the probed laser beam. In a range of the ultrasound frequencies from 200 kHz (Λ = 1.7 mm and α = 0.9 m^{-1}) to 2 MHz (Λ = 0.17 mm and α = 70 m^{-1}), the attenuation of sound is still not too large and the humidity of air has almost no effect on both the attenuation and the accuracy of measurements. For example, for a sound frequency of f = 1 MHz, the resolution along the direction of observation is $\cong$0.7 mm and the sound attenuation factor α is $\cong$0.2 cm^{-1}. The power W_S is maximum at $d_1 = \Lambda/2$ and $d_2 = d_S = 2\Lambda$ (all other factors being the same) and approximately equals

$$W_{S(\max)} \cong \frac{4m}{\pi} I_0 n_0 \sigma \Omega \Lambda^3 \exp(-\alpha y). \quad (3)$$

The laser radiation intensity I_0 can be determined from the measured variable component W_S of the Rayleigh signal. Let us estimate the minimum measurable intensity of laser radiation. Restricting our consideration to the shot noise and assuming that this noise is determined by the constant component of the Rayleigh scattering W_R, the power signal-to-noise ratio (S/N) at the photodetector output can be written as

$$\frac{S}{N} \cong \frac{\sigma\lambda\eta\Omega n_0 d_1 d_2 L I_0}{4ch}\frac{1}{\Delta F}\left[\frac{m\Lambda d_S}{\pi d_1 L}\sin\left(\frac{\pi d_1}{\Lambda}\right)\right]^2, \quad (4)$$

where η is the quantum efficiency of the photomultiplier, h is the Planck constant, c is the speed of light, and ΔF is the passband of an amplifier installed in the receiving system. At a sound frequency of 1 MHz; the sound intensity at the focal point I = 1 W/cm^2; a solid observation angle of 0.4 sr; the radiation wavelength λ = 0.63 μm; and the optimum dimensions of the observation channel $d_1 = \Lambda/2$, $d_2 = d_S = 2\Lambda$ (extraction volume $V = 8 \times 10^{-5}$ cm^3), and $L/d_S = 5$, the ratio $S/N = 1$ is reached at a laser radiation intensity of 100 W/cm^2 and a 100 Hz passband of the amplifier used in the receiving system. Note that $I_{min} \sim \lambda^3$. Using well-known radio engineering methods (e.g., the acquisition method), one can substantially increase the signal-to-noise ratio.

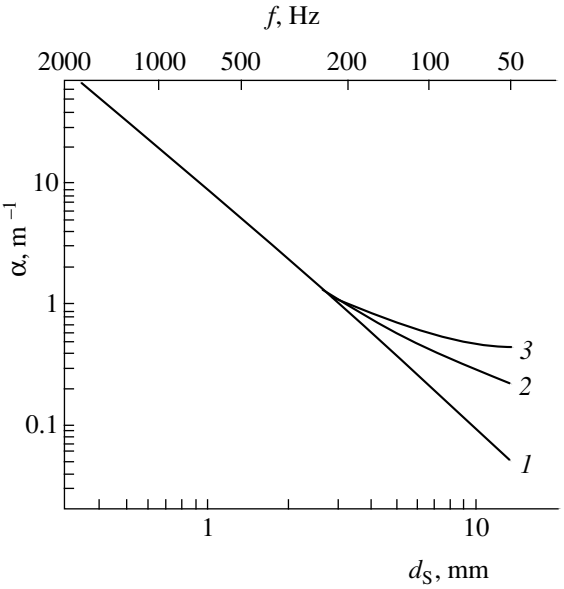

Fig. 2. The relationship between the sound attenuation factor in dry and humid air and the minimum dimension $d_S = 2\Lambda$ of the probed volume along the direction of observation for the scheme of measurements shown in Fig. 1. Curve *1* corresponds to dry air and curves *2* and *3* correspond to a relative humidity of 40 and 100%, respectively. The upper horizontal axis corresponds to the sound frequency *f*.

Acknowledgments. This work was supported in part by the State Committee of Russian Federation on Higher Education (project GR-72-96) and by the "Universities of Russia: Fundamental Studies" program (project no. 1669).

REFERENCES

1. O. V. Belikova, Yu. K. David, and L. V. Kuprina, Metrologiya, No. 5, 25 (1990).
2. G. M. Gandel'man, P. S. Kondratenko, and B. N. Levinskiĭ, in *Methods and Facilities for the Measurement of Laser Radiation Parameters*, VNIIFTRI (Moscow, 1985), p. 61.
3. L. W. Hillman, J. Krasinsky, *et al.*, Appl. Opt., No. 22, 3474 (1983).
4. Fang Qiwan and Zhang Xaohui, Chin. J. Lasers **19** (5), 363 (1992).
5. A. P. Solov'ev and O. V. Zyuryukina, Prib. Tekh. Éksp., No. 3, 128 (1999).
6. *Physical Values: A Handbook*, Ed. by I. S. Grigor'ev and E. Z. Meĭlikhov (Énergoizdat, Moscow, 1991).

Translated by A. Kondrat'yev

Technical Physics Letters, Vol. 26, No. 10, 2000, pp. 885–888. Translated from Pis'ma v Zhurnal Tekhnicheskoĭ Fiziki, Vol. 26, No. 19, 2000, pp. 77–83.

Laser Plasma Accelerated by an Optical Discharge Moving in Air at a Hypersonic Velocity

V. N. Tishchenko* and A. I. Gulidov**

** Institute of Laser Physics, Siberian Division, Russian Academy of Sciences, Novosibirsk, Russia*

*** Institute of Theoretical and Applied Mechanics, Siberian Division, Russian Academy of Sciences, Novosibirsk, Russia*

Received May 12, 2000

Abstract—The results of computer simulations show that a pulsing optical discharge moving in the atmosphere at a hypersonic velocity creates a plasma stream propagating in the direction opposite to that of the discharge. The plasma is accelerated upon efflux from the high-pressure region into an "evacuated" channel created by the discharge. Analytical expressions were derived to evaluate the stream velocity, density, and radius depending on the discharge parameters. *© 2000 MAIK "Nauka/Interperiodica".*

Applied aerospace hydrodynamics [1–3] studies the possibility of using laser radiation as a means of controlling the pattern of a body streamlining by a gas flow. In particular, a pulsed optical discharge (POD) generated in a hypersonic gas flow was shown to produce a quasistationary shockwave with a reduced gas density [4]. Experiments [5, 6] with a single laser spark showed evidence of the formation of weak streams. Thomas [7] calculated a stationary flow behind the light-detonation wave (LDW) front. However, Zuev [8] showed that the LDW generation is limited by the aerosol breakdown. Calculations [9, 10] of the streamlining of a body with a thermal source did not consider the stream generation. In a laser jet engine, a plasma stream is formed in the nozzle.

Below, we will demonstrate that a POD may produce a plasma stream in a free gas space. The energy of the laser sparks is converted into the kinetic energy with the participation of "soft walls" (contact breakage) created by a POD in the gas. The mathematical simulation was based on the nonstationary equations of gas dynamics (in the case of axial symmetry) and the Lagrange approach. The equation of state for the atmosphere was formulated using data from [11]. The final differential equations were numerically solved with the aid of a KRUG24 program package within the framework of an explicit finite difference scheme of the "cross" type with triangular cells using an algorithm of the local difference cell rearrangement [12].

The scheme of stream formation is as follows. Acting upon an immobile gas with the pressure P_0 and the density ρ_0, a focused periodic-pulse laser radiation with an axisymmetric power supply produces cylindrical sparks [13] with a length L, a radius $R_0 \ll L$, a pressure $P \gg P_0$, and the absorbed energy $\varepsilon_v \gg \varepsilon_0$ (ε_0 is the air energy within the spark volume at $t = 0$). For the pulse duration $t_1 \ll R_0/C_0$ (C_0 is the sound velocity in the gas), the pressure P is maximum. The focal plane propagates at a velocity V along the beam axis. At a pulse repetition rate $F \approx V/L$, the sparks form a continuous channel with the length $L_C \gg L$, radius $R > R_0$, $\rho \ll \rho_0$, and $P \sim P_0$. Each spark produces a pressure jump at the beginning of the channel, and the resulting plasma is accelerated upon efflux from the high-pressure region into the "evacuated" channel For $T_R/T_Z \approx$ 0.3–1, the stream moves in the direction opposite to that of POD at a velocity $U \approx C$ relative to the surrounding gas (T_R and $T_Z \approx L/C$ are the characteristic times of pressure leveling as a result of the radial and longitudinal expansion of the spark, respectively, and C is the sound velocity in the channel). In the model of a nonviscous gas, the stream is decelerated as a result of interaction with a dense gas at the end of the channel. For a hypersonic POD velocity ($V > C$) in focusing systems with variable focal distance, the deceleration zone does not affect the plasma acceleration. The channel length is limited by cooling and viscous friction. The length can be determined from the following relationship: $L_C \approx 10T_1V$, where $T_1 \sim 0.0003$ s is the characteristic time of the laser plasma cooling to approximately half of the initial temperature [14].

As seen from data presented in the figure, the axial velocity $U(Z)$ of the stream attains a quasistationary level at some distance from the beginning of the channel. In the stationary flow stage ($P \sim P_0$), the process can be described by a simplified analytical model. The problem is determined by nine parameters: P_0 and ρ_0 (medium); γ_0 (adiabate exponent); ε_v, F, and t_1 (laser radiation); and V, L, and R_0 (pulsed optical discharge). There are six independent dimensionless combinations

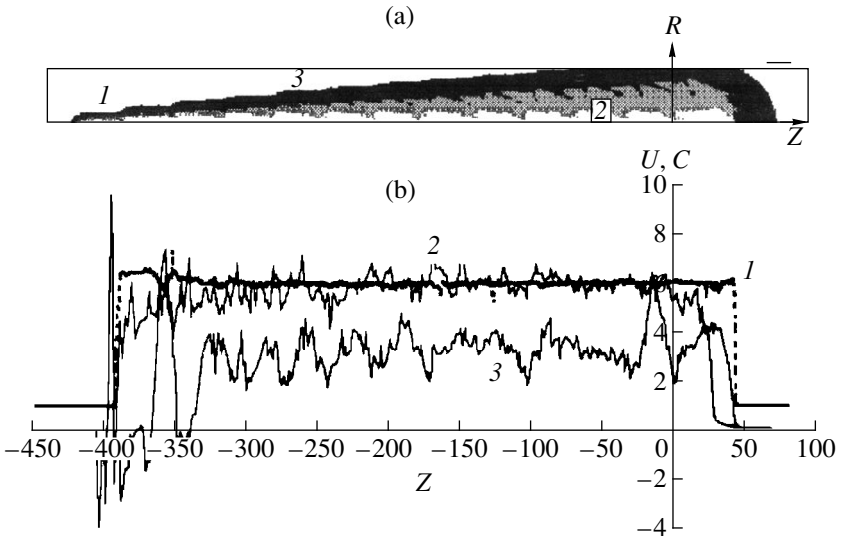

Fig. 1. The calculated pattern of perturbations created by POD moving in air (from right to left) at a velocity of 5100 m/s ($M_0 = 15$) with $\varepsilon = 208$. The firs spark was generated within the region $0 \le Z \le L$; $R_0 = 0.0025$ m. The distribution corresponds to the time instant $t = 26.7$ (200 μs) and a stream length of ~1 m. (a) Longitudinal (Z) and radial (R) distributions of the gas density at $L = 32$ (0.08 m): (*1*) "last" spark; (*2*) plasma stream; (*3*) shockwave. (b) Longitudinal (Z) distribution at $R = 0$ of the (*1*) sound velocity at $L = 32$ and (*2*, *3*) stream velocity at $L = 8$ (*2*) and 32 (*3*).

of parameters (π-theorem). For $t_1 \ll R_0/C_0$, the effect of t_1 is small. The parameter ρ enters into the equation of state in the form of an almost linear term. The condition of continuity of the channel leads to the relationship

$$F^{-1} \approx T_S = L/M_0, \tag{1}$$

where $M_0 = V/C_0$ (here and below, all quantities are presented in a dimensionless form). The values of time, dimensions, velocity, density, and pressure were normalized to R_0/C_0, R_0, C_0, ρ_0, and P_0, respectively. For air ($\gamma_0 = 1.4$), there are only three independent dimensionless parameters: M_0, L, and

$$\begin{aligned}\varepsilon = \varepsilon_v/\varepsilon_0 &= \varepsilon_v(\gamma_0 - 1)/[\pi R_0^2 L P_0 \\ &= (\gamma_0 - 1)Q/P_0 = [W/(VP_0)][(\gamma_0 - 1)/(\pi R_0^2)].\end{aligned} \tag{2}$$

Here Q [J/m^3] and $W/(VP_0)$ [J/(m Pa)] are the density and the linear density of energy absorbed in the spark, respectively; $W = \varepsilon_v F$ is the average POD power; F [Hz] is the pulse repetition rate; L [m] is the spark length; and V [m/s] is the focal plane propagation velocity.

The results of our calculations indicate that, with a sufficiently high precision, the stream radius, density, and specific internal energy density can be considered as depending only on ε. Let us introduce a complex $\tau(M_0, L, \varepsilon)$ describing the axial component of the stream velocity (the radial component is negligibly small). There are two possible regimes of POD interaction with the gas medium: pulsed (the interval between laser radiation pulses is large, $T_S \gg T_R$, and the length of the high-pressure zone is equal to the spark length L) and quasistationary, where $T_S \ll T_R$: the high-pressure zone consists of the plasma of many laser sparks and has a length of

$$L^* = M_0 T_R. \tag{3}$$

Taking this into account, we have selected τ in the form of the ratio T_R/T_Z, which can be expressed as

$$\begin{aligned}\tau &= T_R C/L (L \gg L^*), \\ \tau &= (C/M_0)(L \ll L^*), \\ \tau &= (C/M_0)/(1 + bL/L^*)(L \sim L^*),\end{aligned} \tag{4}$$

where $b \sim 1$, while T_R and C depend on ε. This model is applicable to a system with cylindrical geometry ($L^*/2 \gg 1$ for $L \ll L^*$ and $L/2 \gg 1$ for $L \ge L^*$), instantaneous heating ($t_1 \ll R_0/C_0$), and a sufficiently large energy ($\varepsilon \gg 1$) absorbed in the cold gas.

The values of T_R and C were determined by numerically solving the problem of a cylindrical domain exhibiting thermal explosion in air. An analysis of the results showed that the spark expansion may be separated into two stages. In the fast stage ($t_1 < t < T_R$), pressure in the spark drops from the maximum (at $t = t_1$) to $P \approx 2$ ($t = T_R$) and the rate of contact breakage drops from supersonic to ~0.3. In the subsequent slow stage ($T_R < t < T_P$), the pressure decreases to $P \approx 1$ and the plasma boundary ceases to propagate ($t = T_P$). For $t > T_R$, the sound velocity and the specific internal

energy density ε_P in the explosion cavern weakly depend on r and t. The calculated values of T_R, T_P, and the corresponding parameters C, ρ, R, and ε_P were approximated by different power functions in the two energy ranges.

For $t = T_R$ (the values of error δ are indicated when $\delta > 0.05$):

$$T_R = 0.7\varepsilon^{0.2} (\delta < 0.1), \quad C = 1.26\varepsilon^{0.3} \quad (\varepsilon = 5\text{–}200);$$
$$T_R = 0.08\varepsilon^{0.6}, \quad C = 0.713\varepsilon^{0.4} \quad (\varepsilon = 200\text{–}1000). \tag{5}$$

For $t = T_P$, we obtain

$$C = 1.15\varepsilon^{0.3}, \quad \varepsilon_P = 0.53\varepsilon \quad (\varepsilon = 5\text{–}200);$$
$$C = 0.68\varepsilon^{0.4}, \quad \varepsilon_P = 1.38\varepsilon^{0.84} \quad (\varepsilon = 200\text{–}1000);$$
$$T_P = 0.5\varepsilon^{0.5}, \quad \rho = 1.6/\varepsilon^{0.8}, \quad R = 0.8\varepsilon^{0.4} \ (\delta < 0.1). \tag{6}$$

Expressions (6) can be used to evaluate the stream parameters in the stationary flow stage. Substituting formulas (5) into Eqs. (3) and (4), we obtain the following expressions for L^* and τ:

	$\varepsilon = 5\text{–}200$	$\varepsilon = 200\text{–}1000$	
	$L^* = 0.7M_0\varepsilon^{0.2}$,	$L^* = 0.08M_0\varepsilon^{0.6}$,	(7)
$(L \gg L^*)$	$\tau = 0.88\varepsilon^{0.5}/L$,	$\tau = 0.057\varepsilon/L$,	(8)
$(L \ll L^*)$	$\tau = 1.26M_0^{-1}\varepsilon^{0.3}$,	$\tau = 0.713M_0^{-1}\varepsilon^{0.4}$,	(9)
$L^* \sim L$	$\tau = 1.26M_0^{-1} \times \varepsilon^{0.3}/(1 + L/L^*)$,	$\tau = 0.713M_0^{-1} \times \varepsilon^{0.4}/(1 + L/L^*)$.	(10)

The results of our calculations are presented in the figure for a quasistationary ($L \ll L^*$) and nearly pulsed ($L \sim L^*$) stream acceleration regimes. The sound velocity in the stream in both cases was $C \sim 6$. For $L \ll L^*$ and $\tau = C/M_0 = 0.4$, we have $U \approx C$, while in the second case the U value is markedly lower because of a small τ. In the region of stationary flow, the radial component of the stream velocity is small ($U_R \ll U$), the gas density is low $\rho \ll \rho_0$, and $P \sim 1$. Interacting with a dense gas at the end of the channel, the stream is decelerated, a vortex is formed, and a contact surface propagates at a velocity of $\sim 0.5C_0$ in the stream direction. A shockwave formed in the surrounding gas represents a sum of components from many individual spars. The longitudinal component of the shockwave momentum compensates for the stream momentum. The stream power amounts to ~50% of the power absorbed in the POD, while the remaining fraction is transmitted with the shockwave.

The stream velocity variation along the channel axis is not monotonic. However, an effective Mach number for the average U and C values along the stream selected as the parameters (for various initial data ad the same τ) is well approximated by the following egression:

$$M = U/C = (1 + 1.33 \times 10^{-4}\tau^{-5})^{-1}. \tag{11}$$

It should be recalled that M and τ depend on M_0, L, and ε. However, formula (11) can be simplified for $\tau > 0.3$ to yield $M \approx 1$ and for $\tau < 0.15$, when $M \approx 7500\tau^5$. For $L \geq L^*$ and small τ, the modulation of U is close to 100%. Using Eqs. (1), (2), and (6)–(11), we may evaluate the velocity, radius, gas density, and energy density in the stream for the given parameters of the medium and the POD.

We may also solve the inverse problem of determining the POD parameters necessary to obtain a stream with desired properties. The pressure of deceleration at the stream axis can be determined using expressions from Eqs. (11) and (6) and the relationship $P = \gamma_0\rho C^2M^2 + 1$. Substituting formulas (6), we obtain $P = 1.48M^2/\varepsilon^{0.2} + 1$ ($\varepsilon < 200$) and $P = 0.518M^2 + 1$ ($\varepsilon = 200$–1000). This yields $P \approx 1.5$–2 for $\tau > 0.3$ and $P \approx 1$ for $\tau < 0.1$. Assuming that all of the plasma is accelerated to the sound velocity, we may estimate a ratio of the kinetic stream power to the POD power: $\eta = \gamma_0(\gamma_0 - 1)\varepsilon^{-1}C^2/2 \sim 0.1$–$0.15$. These values of η can be reached using special modes of energy supply to the plasma.

Thus, we have demonstrated that laser radiation can, under special conditions, induce moving plasma and gasodynamic inhomogeneities moving in a gas in the form of shockwave and plasma streams.

Acknowledgments. The authors are grateful to A.G. Ponomarenko for fruitful discussions and support. The work was financed by the Russian Foundation for Basic Research, project no. 00-02-17482.

REFERENCES

1. L. N. Myrabo and Yu. P. Raizer, AIAA Pap., No. 94-2451, 1 (1994).
2. I. V. Nemchinov, V. I. Artem'ev, V. I. Bergelson, *et al.*, Shock Waves, No. 4, 35 (1994).
3. V. Yu. Borzov, V. M. Mikhaĭlov, I. V. Rybka, *et al.*, Inzh.-Fiz. Zh. **66** (5), 515 (1994).
4. P. K. Tret'yakov, G. N. Grachev, A. I. Ivanchenko, *et al.*, Dokl. Ross. Akad. Nauk **336** (4), 466 (1994) [Phys. Dokl. **39**, 415 (1994)].
5. I. A. Bufetov, A. M. Prokhorov, V. B. Fedorov, *et al.*, Dokl. Akad. Nauk SSSR **261** (3), 586 (1981) [Sov. Phys. Dokl. **26**, 1066 (1981)].

6. V. N. Kondrashov, N. B. Rodionov, S. F. Sitnikov, *et al.*, Zh. Tekh. Fiz. **56** (1), 89 (1986) [Sov. Phys. Tech. Phys. **31**, 53 (1986)].
7. P. D. Thomas, AIAA J. **15**, 1405 (1977).
8. V. E. Zuev, in *Optical Discharge in Aerosols* (Nauka, Novosibirsk, 1990), p. 155.
9. V. A. Levin, N. E. Afonina, P. Yu. Georgievskiĭ, *et al.*, Preprint No. 36–98 (Institute of Mechanics, Moscow State University, Moscow, 1988), p. 48.
10. S. V. Guvernyuk and A. B. Samoĭlov, Pis'ma Zh. Tekh. Fiz. **23** (9), 1 (1997) [Tech. Phys. Lett. **23**, 333 (1997)].
11. N. M. Kuznetsov, in *Thermodynamic Functions and Impact Adiabates for Air at High Temperatures* (Mashinostroenie, Moscow, 1965), p. 462.
12. V. M. Fomin, A. I. Gulidov, and G. A. Sapozhnikov, in *High-Speed Interaction of Substances* (Sib. Otd. Ross. Akad. Nauk, Novosibirsk, 1999), p. 600.
13. V. V. Korobkin, L. Ya. Polonskiĭ, and L. N. Pyatnitskiĭ, Tr. Inst. Obshch. Fiz., Ross. Akad. Nauk **41**, 23 (1993).
14. V. N. Tishchenko, Opt. Atmos. Okeana **11** (2), 228 (1998).

Translated by P. Pozdeev

Technical Physics Letters, Vol. 26, No. 10, 2000, pp. 889–890. Translated from Pis'ma v Zhurnal Tekhnicheskoĭ Fiziki, Vol. 26, No. 19, 2000, pp. 84–87.

"Oscillating" Riemann Invariants of the Hyperbolic Systems of Partial Differential Equations

Yu. N. Zaĭko

The Volga Region Academy of Government Services, Saratov, Russia

e-mail: pags@pags.renet.ru

Received March 2, 2000

Abstract—The phenomenon of wavenumber oscillations in a wave packet representing an RF pulse propagating in a dispersive medium was studied by numerical methods. An explanation is suggested in the context of nonlinear geometrical optics (NGO), where the wavenumber is a Riemann invariant that remains constant on characteristics of the corresponding equations. The wavenumber oscillations arise in the region of intersection of the characteristics of the equations. It is demonstrated that the intersection of characteristics is due to the approximation neglecting the interaction between narrow-band wave packets constituting the pulse. With the packet interaction ignored, the characteristics are straight lines. If the interaction is allowed for, the characteristics do not intersect and may significantly differ in shape from straight lines. Consequently, an external observer moving at a constant velocity crosses the same characteristic many times, thus perceiving the wavenumber as an oscillating function. © *2000 MAIK "Nauka/Interperiodica".*

As is known, a hyperbolic system of partial differential equations (PDEs) possesses real and different characteristics of the component equations. Such are the equations of nonlinear geometrical optics,

$$\begin{aligned} \frac{\partial k}{\partial t} + v_g \frac{\partial k}{\partial x} &= 0, \\ \frac{\partial E_k}{\partial t} + \frac{\partial}{\partial x}(v_g E_k) &= 0, \end{aligned} \tag{1}$$

where $k = \Phi_x(x, t)$ is the wavenumber; $v_g = \partial\omega/\partial k$ is the group velocity, $\omega = -\Phi_t(x, t)$ is the frequency; and $E_k \sim a_k^2$ is the energy spectral density of a narrow-band wave packet whose amplitude is a_k. System (1) is interesting both in itself and as a good model of many objects featuring a wave motion. One of the Riemann invariants of system (1) is $k(x, t)$. The wavenumber is constant on any characteristic determined by the equation $dx/dt = v_g$. Hyperbolic PDEs may be solved by integration along characteristics. The approach enables one to construct a solution of system (1) subjected to an initial condition $k(x, t = 0) = F(x)$. The solution is defined outside the region of characteristics intersection in the (x, t) plane. The region is bounded by a curve that has a singular point with coordinates

$$t^* = \left[v_g' \left(\frac{\partial k}{\partial x} \right)_{t=0} \right]^{-1}, \quad x^* = v_g t^*. \tag{2}$$

In this region, a classical solution of system (1) becomes multivalued, which is unacceptable. There are two alternative ways typically followed to remove the ambiguity:

(1) Construct a discontinuous solution of the shock wave type with a zero front width; in the (x, t) plane, the discontinuity propagates along a curve emerging from point (2) [1].

(2) Complement system (1) with higher derivative terms so as to include, e.g., viscosity; the resulting shock wave has a finite front width, the solution oscillating within these limits [2].

It should be pointed out that the variety of hyperbolic PDEs by no means reduces to the above cases and the presence of higher derivatives does not exhaustively account for the oscillating behavior of solutions to hyperbolic PDEs. Indeed, consider the figure which depicts the computed propagation of a rectangular-envelope pulse for the H_{10} mode in a metal waveguide [3]. The problem reduces to solving the Klein–Gordon equation subject to appropriate boundary conditions. Although the equation does not include higher derivatives, the solution does oscillate.

To find out a reason for the oscillating behavior of $k(x, t)$ or $\omega(x, t)$, let us separate two narrow-band wave packets centered at k_1 and k_2 from the propagating pulse. The corresponding nonlinear dispersion equations are as follows:

$$\begin{aligned} \omega_1 &= \omega_0(k_1) + \sigma_1 a_1^2 + \mu_1 a_1^2 a_2^2 + \ldots \\ \omega_2 &= \omega_0(k_2) + \sigma_2 a_2^2 + \mu_2 a_2^2 a_1^2 + \ldots \end{aligned} \tag{3}$$

The terms with $\sigma_{1,2}$ were considered by Whitham [1],

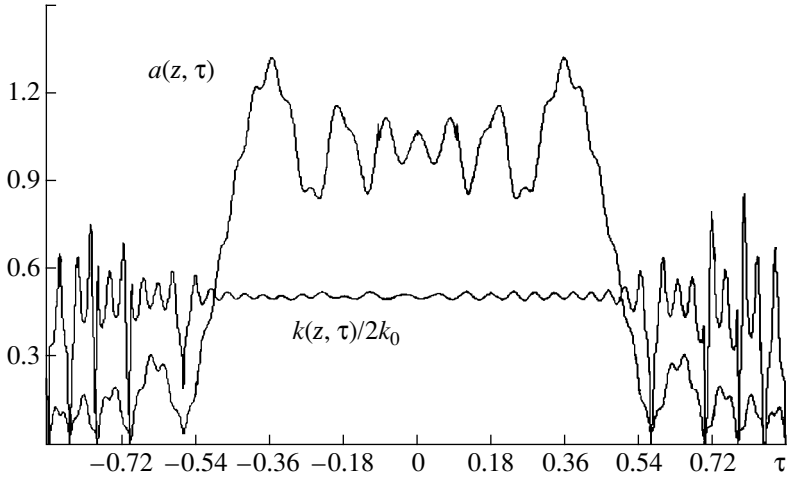

Computed propagation of a rectangular-envelope RF pulse of the H_{10} mode in a rectangular metallic waveguide without attenuation: $a(z, \tau)$ and $k(z, \tau)$ are the amplitude and the wavenumber, respectively, with $z = x|k''(\omega_0)|/T^2$ and $\tau = (t - xk'(\omega_0))/T$; x is the coordinate; t, the time; ω_0, the pulse carrier frequency; T, the pulse duration; and $k_0 = k(\omega_0)$, a solution of the dispersion equation. The pulse parameters are as follows: $\pi z|k''(\omega_0)|^{1/2} = 0.14$; $zk_0 = 100$; $zk_0'/T = 0.1$; $a(0, \tau) = 1$ for $|\tau| \le T/2$ and $a(0, \tau) = 0$ be $|\tau| > T/2$. The computation is performed in the second-order approximation of the dispersion theory.

who revealed the splitting of the characteristics ($i = 1, 2$)

$$\frac{dx}{dt} = v_g(k_i) \pm [\sigma_i v_g'(k_i)]^{1/2} a_i. \quad (4)$$

The terms with $\mu_{1.2}$ refer to the interaction between the wave packets and can be evaluated by computing a two-particle Green's function [5] within the framework of the Hamiltonian formalism [4]. In line with [1], we neglect the dependence of σ and μ on k (an allowance for this dependence leads to simple renormalization). Substitute expressions (3) into system (1) and seek a solution in the form $k_{1.2}$, $a_{1.2}^2 \sim \exp(j\Omega t - jqx)$. The result is as follows ($i = 1, 2$):

$$(K_1 - 1)(K_2 - 1) = 4\mu_1\mu_2 \frac{a_1^2 a_2^2}{\sigma_1\sigma_2};$$
$$K_i = \frac{1}{\sigma_i v_{gi}'}\left(\frac{V - v_{gi}}{a_i}\right)^2, \quad V = \frac{\Omega}{q}. \quad (5)$$

Thus, taking into account the interaction between two narrow-band wave packets reveals that the characteristics of system (1) do not intersect. Since a solution is formed by many packets, the characteristic may greatly differ from a straight line. Consider an external observer moving at a velocity u along the straight line $dx/dt = u$ in the (x, t) plane. Each characteristic, on which the Riemann invariant $k(x, t)$ is uniform, is crossed by the observer many times. That is why the observer perceives $k(x, t)$ as an oscillating function. With T denoting the pulse duration [3], the oscillation frequency is

$$f = T v_g^2 \left(\frac{\partial k}{\partial x}\right)_{t=0} \frac{x^*}{x}. \quad (6)$$

In conclusion, recall that oscillations in parameters of waves propagating in different media were observed in various studies involving the solution of wave equations. Although both exact [6] and [7] solutions were considered, no physical explanation has been found for the phenomenon.

REFERENCES

1. G. B. Whitham, *Linear and Nonlinear Waves* (Wiley, New York, 1974; Mir, Moscow, 1977).
2. V. I. Karpman, *Non-Linear Waves in Dispersive Media* (Nauka, Moscow, 1973; Pergamon, Oxford, 1975).
3. Yu. N. Zaĭko, Izv. Vyssh. Uchebn. Zaved., Radiofiz. **32** (12), 1558 (1989).
4. V. E. Zakharov and E. A. Kuznetsov, Usp. Fiz. Nauk **167** (11), 1137 (1997).
5. L. P. Kadanoff and G. Baym, *Quantum Statistical Mechanics: Green's Function Methods in Equilibrium and Nonequilibrium Problems* (Benjamin, New York, 1962; Mir, Moscow, 1964).
6. A. B. Shvartsburg, Usp. Fiz. Nauk **168** (1), 85 (1998).
7. Yu. P. Verbin, Radiotekh. Élektron. (Moscow) **40** (8), 1169 (1995).

Translated by A. Sharshakov

Technical Physics Letters, Vol. 26, No. 10, 2000, pp. 891–893. Translated from Pis'ma v Zhurnal Tekhnicheskoĭ Fiziki, Vol. 26, No. 19, 2000, pp. 88–94.

Cathode Layer Characteristics of a Low-Pressure Glow Discharge in Argon and Nitrogen

V. A. Lisovskiĭ and S. D. Yakovin

Scientific Physicotechnological Center, Kharkov State University, Kharkov, Ukraine

Received February 18, 2000; in final form, May 22, 2000

Abstract—Cathode layer characteristics were experimentally determined for a glow discharge in argon and nitrogen in a broad range of gas pressures. A normal glow discharge regime is observed only provided that the gas ionization takes place in the anode layer (on the right of the inflection point in the glow discharge initiation curve). Importance of using a correct method for the normal cathode voltage drop is emphasized. © *2000 MAIK "Nauka/Interperiodica".*

As is known [1–10], there are two possible regimes of a dc glow discharge—normal and anomalous. In the anomalous mode, an increase in the discharge current I_{dc} is accompanied by a growth in the voltage drop U_c across the cathode layer (and the voltage between electrodes U_{dc}) and by a drop in the cathode layer thickness d_c. In this regime, the discharge extends over the whole cathode surface, whereas in the normal mode only a part of the cathode surface is involved in the discharge operation. When the discharge current is decreased, the cathode voltage drop and the cathode layer thickness remain unchanged ($U_c = U_n$ and $pd_c = (pd_c)_n$, where p is the gas pressure), while the discharge area S on the cathode decreases (but the current density is constant $j = I_{dc}/S = j_n$). It was claimed [3, 11, 12] that the normal glow discharge regime can be observed only to the right of the minimum in the glow discharge initiation curve, that is, at $pL \geq (pL)_{min}$ (L is the interelectrode distance), while at lower gas pressures only an anomalous glow discharge mode is possible.

The purpose of this work was to measure the cathode layer characteristics (cathode voltage drop U_c, cathode layer thickness d_c, ratio of the discharge current density to the square of gas pressure j/p^2) for a short (free of a positive column) low-pressure glow discharge in argon and nitrogen in a broad range of gas pressures. It was found that a normal discharge regime is observed only to the right of the inflection point in the glow discharge initiation curve provided that the gas ionization takes place in the anode layer. We will also demonstrate that one of the methods used to determine the normal cathode voltage drop leads to incorrect data.

The experiments were performed in argon and nitrogen at pressures p in the range from 10^{-2} to 10 Torr, the discharge voltages $U_{dc} \leq 1000$ V, and the discharge currents $I_{dc} \leq 100$ mA. The voltage of a dc source was applied to a duralumin cathode, while a stainless steel anode was grounded. The cathode and anode diameters were virtually equal to that (100 mm) of the discharge tube, and the interelectrode distance was $L = 33$ mm. Some experiments were performed in a 63-mm-diam discharge tube containing a mobile stainless steel cathode and anode with a diameter of 62 mm. The discharge plasma parameters were measured using a single cylindrical nichrome probe with a length of 5 mm and a diameter of 0.18 mm. The voltage drop across the cathode layer U_c was determined by placing the probe at a visible layer boundary and measuring the plasma potential φ_{pl} relative to the anode. The U_c value was calculated as the difference of the voltage between electrodes U_{dc} and the plasma potential ($U_c = U_{dc} - \varphi_{pl}$). The current density j was determined as the ratio of the current I_{dc} measured in the electrode circuit to the cathode area S. If the normal current density effect was observed, the j value was determined by measuring the discharge current under conditions when the discharge was extended over the whole cathode surface while the voltage was still equal to the normal value.

Figure 1 shows the glow discharge initiation curves $U_{dc}(p)$ and a plot of the minimum cathode voltage drop $U_{c(min)}$ versus the gas pressure p. The minimum cathode voltage drop U_c(min) refers to the U_c value measured immediately before the discharge quenching. As seen from Fig. 1, an increase in the gas pressure is accompanied by decrease in $U_{c(min)}$ down to a minimum value of $U_{c(min)} = U_n$ ($U_n = 200 \pm 3$ V for argon and $U_n = 280 \pm 3$ V for nitrogen) reached at $p = p_n$ ($p_n/p_{min} \approx 3.5$).

As was demonstrated previously [13], the glow discharge initiation curves exhibit (on the right of the minimum) an inflection point with the coordinates $p = p_{inf}$ and $U_{dc} = U_{dc(inf)}$ such that

$$\frac{U_{dc(inf)}}{U_{dc(min)}} = \frac{e}{2}, \quad \frac{p_{inf}}{p_{min}} = e, \tag{1}$$

where e is the natural logarithm base, p_{min} and $U_{dc(min)}$ being the coordinates of the minimum in the glow dis-

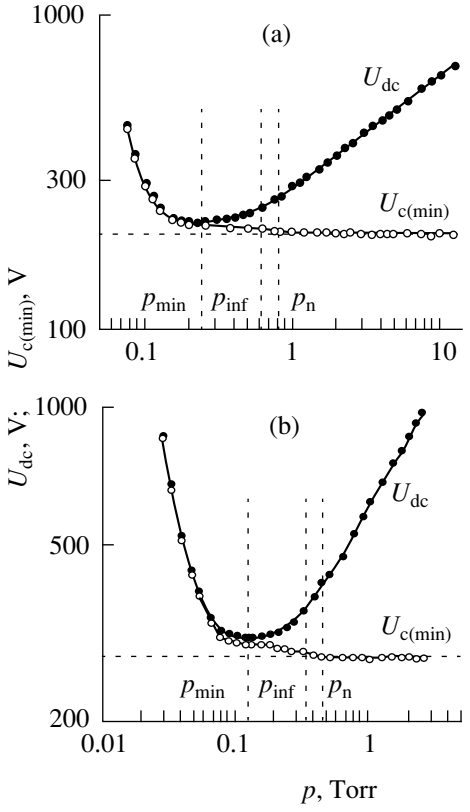

Fig. 1. The glow discharge initiation curve $U_{dc}(p)$ and a plot of the minimum cathode voltage drop $U_{c(min)}$ versus the gas pressure p for (a) argon and (b) nitrogen. Discharge tube diameter 100 mm; interelectrode distance L = 33 mm.

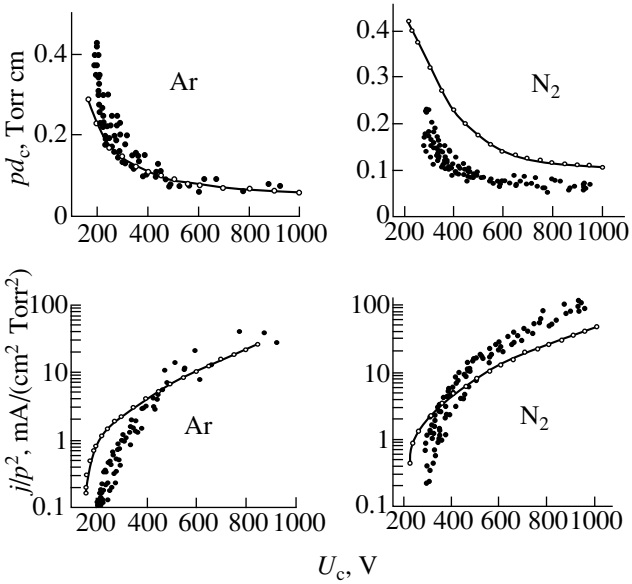

Fig. 2. Plots of a product of the pressure by the cathode layer thickness (pd_c) and of the ratio of the discharge current density to the square of gas pressure (j/p^2) versus the cathode voltage drop U_c measured for the glow discharge in argon and nitrogen. Discharge tube diameter 100 mm; interelectrode distance L = 33 mm.

charge initiation curves. Relationships (1) indicate that a threshold pressure p_n corresponding to the onset of the normal glow discharge regime occurs to the right of the inflection point. This conclusion was confirmed by the results of our measurements of the discharge current–voltage characteristics and by visual observations of the glow discharge region near cathode.

Figure 2 shows the plots of pd_c and j/p^2 versus U_c measured for the glow discharge in argon and nitrogen. For argon, $(pd_c)_n \approx 0.4 \pm 0.03$ Torr cm and $(j/p^2)_n \approx 0.11 \pm 0.02$ mA/(cm^2 Torr^2), while for nitrogen $(pd_c)_n \approx 0.23 \pm 0.03$ Torr cm and $(j/p^2)_n \approx 0.22 \pm 0.02$ mA/(cm^2 Torr^2). Also presented in Fig. 2 are the plots of experimental data for an iron cathode taken from a review of Frencis [2] which show a reasonable agreement with our results. Note that the experimental values of pd_c and j/p^2 determined as functions of U_c for various gas pressures and voltages between electrodes quite satisfactorily fit to the same curve.

According to [4, 14], the transition from Townsend to the glow discharge regime proceeds in such a manner that the potential redistribution (related to a perturbation of the field in vacuum E_{dc} by the space charge) inhibits the electron multiplication to the left of the inflection point. At the same time, the potential redistribution to the right of the inflection point facilitates the multiplication process and the glow discharge may exist at lower voltages. Therefore, the normal discharge regime may be observed only in the vicinity and to the right of the inflection point.

In practice, the cathode voltage drop U_c is frequently determined by the following procedure. The glow discharge is initiated for L on the order of a few centimeters, after which the anode is moved toward cathode and the voltage between electrodes is measured at a constant discharge current [2, 3, 15, 16]. Figure 3a shows a plot of U_{dc} versus L obtained using this procedure. The minimum voltage between electrodes determined by this method at several values of the discharge current is usually assumed to be represent the normal cathode voltage drop U_n. However, we will now demonstrate that this method of determining the normal cathode voltage drop is incorrect.

Let us fix the distance $L = L_1$, at which a minimum voltage between electrodes is observed, and measure the discharge current–voltage characteristic $I_{dc}(U_{dc})$ (Fig. 3b). Under these conditions, the normal current density effect is absent (i.e., neither current increases at a constant voltage nor the discharge area contracts with decreasing current in the electrode circuit). Therefore, the minimum voltage between electrodes determined as described above by no means represents the true normal cathode voltage drop. The discharge observed under these conditions corresponds to a discharge at $pL \approx (pL)_{min}$. Now, let us increase the distance between electrodes, while the discharge is glowing and the voltage between electrodes has a minimum value. When

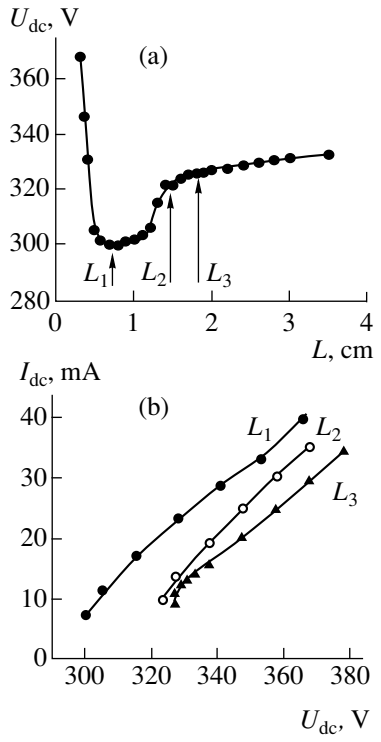

Fig. 3. Plots of (a) the voltage between electrodes U_{dc} vs. the interelectrode distance L measured at a constant discharge current I_{dc} = 10 mA and (b) the current–voltage characteristic $I_{dc}(U_{dc})$ measured for a glow discharge in nitrogen with the interelectrode distances L_1–L_3 indicated in Fig. 3a. Discharge tube diameter 63 mm; nitrogen pressure p = 1 Torr.

the anode goes sufficiently far away into the dark Faraday space ($L = L_2$), the voltage between electrodes exhibits a sharp drop (by 10–20 V, depending in the particular gas type). Simultaneously, an anode sheath in the form of a thin lighting layer appears at the anode surface. Under these conditions, no normal glow discharge exists either. Upon a further increase in the interelectrode distance ($L = L_3$), the normal current density effect appears at a minimum discharge current density (Fig. 3b). As seen from the comparison between Figs. 1 and 3, the normal cathode voltage drop may be observed only provided that the voltage between electrodes is not minimum. Therefore, the aforementioned conventional method of determining the normal cathode voltage drop is incorrect.

Thus, we have experimentally established that the glow discharge may exist in the normal regime only in the presence of an anode sheath at the anode surface. Once the anode sheath is not observed, the glow discharge operates in the anomalous regime. The anode sheath appears when the voltage drop across the anode layer is close to the electron-impact ionization potential of gas molecules. Therefore, there is a relationship between the onset of a normal glow discharge regime and the effect of ionization in the anode layer.

Thus, we have determined the cathode layer characteristics for a glow discharge in the normal and anomalous regimes. It was found that the normal glow discharge regime may exist only in the region of pressures to the right of the inflection point in the glow discharge initiation curve.

REFERENCES

1. M. J. Druyvesteyn and F. M. Penning, Rev. Mod. Phys. **12** (2), 87 (1940).
2. G. Frencis, in *Handbuch der Physik*, Ed. by S. Flugge (Springer-Verlag, Berlin, 1956), Vol. 22, pp. 53–208.
3. V. L. Granovskiĭ, *Electric Current in a Gas. Steady-State Current* (Nauka, Moscow, 1971).
4. Yu. P. Raĭzer, *The Physics of Gas Discharge* (Nauka, Moscow, 1987).
5. V. N. Melekhin and N. Yu. Naumov, Pis'ma Zh. Tekh. Fiz. **12** (2), 99 (1986) [Sov. Tech. Phys. Lett. **12**, 41 (1986)].
6. Yu. D. Korolev, Zh. Tekh. Fiz. **57** (2), 380 (1987) [Sov. Phys. Tech. Phys. **32**, 231 (1987)].
7. Yu. P. Raĭzer and S. T. Surzhikov, Pis'ma Zh. Tekh. Fiz. **13** (8), 452 (1987) [Sov. Tech. Phys. Lett. **13**, 186 (1987)].
8. G. G. Lister, J. Phys. D **25** (12), 1649 (1992).
9. W. Helin, L. Zuli, and L. Daming, Vacuum **47** (9), 1065 (1996).
10. M. Goto and Y. Kondoh, Jpn. J. Appl. Phys. **37** (1), 308 (1998).
11. B. N. Klyarfel'd, L. G. Guseva, and A. S. Pokrovskaya-Soboleva, Zh. Tekh. Fiz. **36** (4), 704 (1966) [Sov. Phys. Tech. Phys. **11**, 520 (1966)].
12. B. N. Klarfeld, L. G. Guseva, and V. V. Vlasov, in *Proceedings of the Xth International Conference on Phenomena in Ionized Gases, Oxford, 1971*, Contrib. Papers 1, p. 97.
13. V. A. Lisovskiĭ and V. D. Yegorenkov, J. Phys. D **27** (11), 2340 (1994).
14. V. I. Kolobov and A. Fiala, Phys. Rev. E **50** (4), 3018 (1994).
15. A. Guntherschulze, Z. Phys. **40**, 414 (1926).
16. A. Guntherschulze, Z. Phys. **49**, 358 (1928).

Translated by P. Pozdeev

Technical Physics Letters, Vol. 26, No. 10, 2000, pp. 894–896. Translated from Pis'ma v Zhurnal Tekhnicheskoĭ Fiziki, Vol. 26, No. 20, 2000, pp. 1–7.

Effect of the Titanium Oxide Stoichiometry on the Efficiency of CO Oxidation on the Au/TiO_x System Surface

T. T. Magkoev*, D. Rosenthal, S. L. M. Schröder**, and K. Christmann****

** North Ossetian State University, Vladikavkaz, Russia*

*** Free University of Berlin, Germany*

e-mail: magkoev@osetia.ru

Received May 12, 2000

Abstract—Infrared reflection absorption and X-ray photoelectron spectroscopies are used to show that the process of carbon monoxide (CO) oxidation can occur on the surface of a system formed during the appearance of gold clusters on the surface of a titanium oxide layer cooled below room temperature. The efficiency of this process is significantly affected by stoichiometry of the titanium oxide layer. The use of a TiO_x substrate with the stoichiometry different from TiO_2 results in more effective CO oxidation in comparison with the process observed in the Au/TiO_2 system. An important role in the oxidation process is played by the gold–oxide interface. © *2000 MAIK "Nauka/Interperiodica".*

In recent years, the materials with metal clusters formed on the surface of oxide substrates have been widely used in heterogeneous catalysis [1, 2]. In particular, one of the most efficient catalysts used in carbon monoxide oxidation is the Au/TiO_2 system [3]. Despite a large number of studies devoted to this process, there is no commonly accepted opinion about the nature of the high catalytic activity of this material. On the one hand, it is believed that the high catalytic activity is provided by the properties of gold clusters [4]; on the other hand, it was suggested that a considerable role belongs to properties of the Au/TiO_2 interface [5]. Elucidation of this problem requires further detailed study of the system properties.

Below, we present experimental data indicating that the titanium oxide stoichiometry plays an essential part in the oxidation of CO molecules on the surface of the Au/TiO_x system. The studies were performed in ultrahigh vacuum (2×10^{-10} Torr) by methods of infrared reflection absorption (IRRAS), X-ray photoelectron (XPS), low-energy ion scattering (LEISS), and Auger electron (AES) spectroscopies. These techniques are described in detail elsewhere [6–9] and are only briefly outlined here.

The IRRAS method reduces to the following: an IR radiation beam polarized in the plane of incidence is incident on the surface at an angle of 80°. This configuration provides the maximum sensitivity of the method to the intramolecular vibrations normal to the surface. This is the situation observed for CO on the surface of most metals. The spectral resolution of this method equals 4 cm^{-1}. The Au/TiO_x structures formed were cooled to a temperature of 90 K, after which CO was adsorbed and the IR spectra were recorded. All the IR spectra of CO molecules were normalized to the background spectrum recorded prior to CO adsorption.

The AES measurements were performed using a cylindrical mirror analyzer and a coaxial electron gun producing a normally incident primary electron beam. The photoelectron spectra were excited by the X-ray AlK_α line with an energy of 1453 eV and recorded with the aid of a spherical deflector analyzer. The LEIS spectra were excited by a 1-keV beam of He ions and measured at a scattering angle of 135°. This method is extremely sensitive to the state of the surface layer and the adsorbed film growth mechanism [10]. The density of the primary He ion beam did not exceed 3×10^{-7} A/cm^2. We believe that the state of the ion-bombarded system only slightly changes during a 3-min-long period of time required to record a LEISS spectrum.

To calibrate the flows of Ti and Au atoms thermally evaporated and deposited onto a substrate surface, we invoked the experimental data on the growth mechanisms of Ti and Au films on the Re(1000) surface. During the room-temperature adsorption of atoms of these metals on the substrate at a deposition rate of 0.15 ML/min, a layer mechanism of the film growth is operative in both cases. Upon growing the first continuous monolayer (ML) of adatoms, the coverage Θ was assumed to be unity. The thickness of the monatomic film was taken equal to the atomic diameter of the corresponding metal. An oxide substrate for gold adsorption was represented by a 130-Å-thick TiO_x layer formed on a Re(1000) crystal surface. Unlike the case of bulky titanium oxide crystals, the use of TiO_x layers allowed us, first, to obtain the desired layer stoichiometry (dependent on the layer formation mode) and, sec-

ond, to study the $CO/Au/TiO_x$ system by the IRRAS method.

We used two modes of the titanium oxide layer deposition. In the first mode, titanium atoms were deposited at a rate of 0.5 ML/min onto the Re(1000) substrate in an oxygen atmosphere at a pressure of 10^{-6} Torr and a temperature of 700 K. Upon the formation of each five monolayers (until attaining a total layer thickness of 30 ML), the deposition of Ti atoms was halted and the system was kept for 10 min in the oxygen atmosphere at the temperature indicated above. An X-ray photoelectron spectrum from the titanium layer thus obtained is shown in Fig. 1 (the lower curve). A comparison of this spectrum with that of a bulky TiO_2 crystal [11] shows that the stoichiometry of the titanium oxide layer is close to TiO_2.

In the second mode, an oxide layer was grown in a similar way with the only difference being that the titanium atoms were continuously deposited until attaining a desired thickness of 30 ML (without intermediate keeping of the deposit in the oxygen atmosphere). The corresponding XPS spectrum is shown in Fig. 1 (the upper curve). Despite the similar location of the main maxima, the two spectra are markedly different. The broader lines and the shoulder *A* observed in the second spectrum indicate that the degree of Ti oxidation in the second mode is lower than that in TiO_2. Therefore, it can be suggested that the second spectrum corresponds to the composition TiO_x (with $x < 2$).

Gold atoms were deposited onto the surface of the titanium oxide layers of these two types at a substrate temperature of 500 K. The process was continued until reaching a coverage corresponding to eight monolayers. According to the LEISS and AES data, three-dimensional gold clusters are formed on the substrate surface in both cases. At $\Theta = 8$ ML, the clusters occupied about 70% of the titanium oxide surface. Assuming that all the islands are of the same hemispherical shape, one can evaluate their heights, which, at this coverage, are about 40 Å. The Au/TiO_2 and Au/TiO_x systems thus obtained were cooled to 90 K and exposed to carbon monoxide until attaining a total exposure of 100 L (1 L = 10^{-6} Torr s). The corresponding IR absorption lines caused by excitation of the intramolecular oscillations in CO adsorbed on the gold surface are shown in Fig. 2a (curve *1*) and Fig. 2b (curve *1*). Upon heat treatment of the systems thus obtained at a temperature of 250 K and their subsequent 30-min exposure to oxygen at a pressure of 10^{-6} Torr, the intensity of the IR absorption lines of carbon monoxide decreased in both cases. The decrease was more pronounced for the system $CO/Au/TiO_x$ (Fig. 2b, curve *2*) than for the system $Co/Au/TiO_2$ (Fig. 2a, curve *2*). Annealing of the same systems at a temperature of 250 K without the subsequent exposure to oxygen did not noticeably changed the spectra. Thus, we may suggest that the observed decrease in the IR line intensities is caused by CO oxidation. As seen from Fig. 2, this process is more efficient on the surface of the Au/TiO_x system than on the surface of the Au/TiO_2 system. This seems to be indicative of the important role of the oxide layer in the carbon monoxide oxidation on the surface of the Au/TiO_x system.

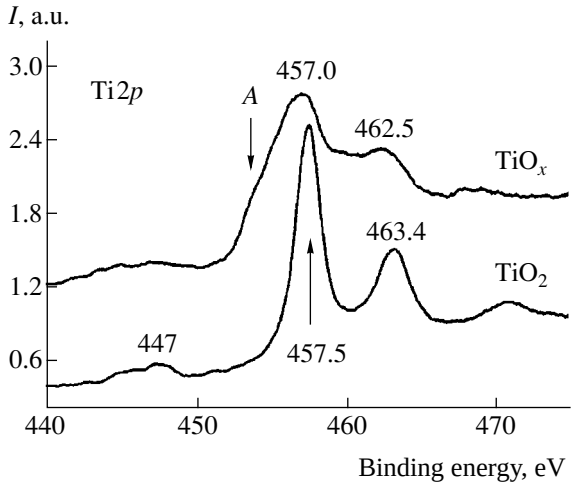

Fig. 1. X-ray photoelectron spectra of titanium oxide layers of different compositions formed on the Re(1000) surface. The layer thickness was estimated at 130 Å.

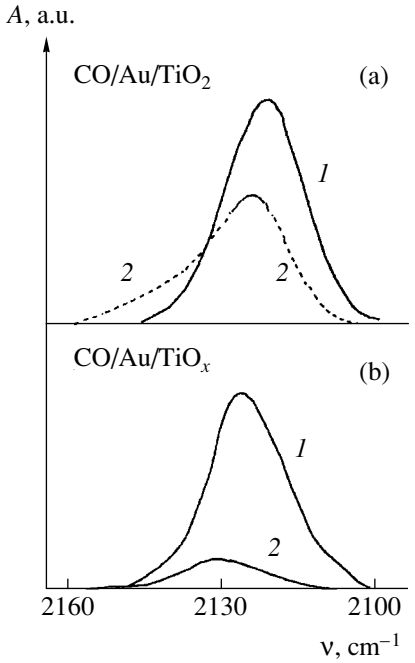

Fig. 2. IR absorption lines of CO molecules on the surface of the (a) Au/TiO_2 and (b) Au/TiO_x ($x < 2$) systems (*1*) prior to and (*2*) after their interaction with oxygen. It is seen that this process is more efficient in the Au/TiO_x system.

This assumption is also confirmed by the XPS study of the interaction between CO molecules and the surface of the Au/TiO_2 system. Figure 3 (curve *1*) shows

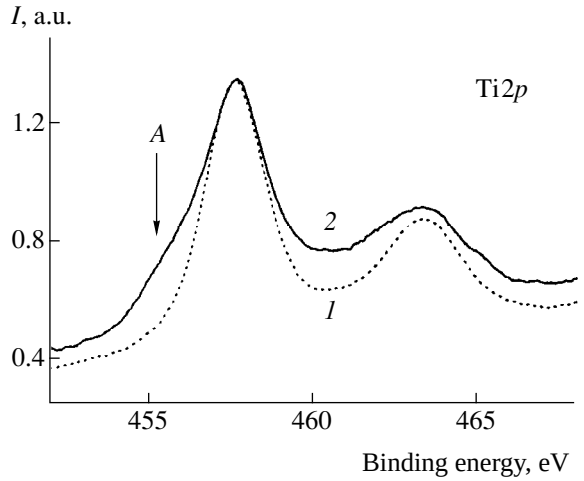

Fig. 3. X-ray photoelectron spectra of a ~130-Å-thick stoichiometric titanium oxide layer TiO_2 (*1*) prior to and (*2*) after interaction with CO molecules. The changes observed upon exposure to CO indicate the loss of oxygen from the titanium dioxide layer.

the X-ray photoelectron spectrum of the Au/TiO_2 system obtained by the procedure described above. The spectrum obtained upon a 1-h exposure of this system to carbon monoxide at a substrate temperature of 500 K is shown in Fig. 3 (curve *2*). The pattern of changes in the spectrum, in particular, the appearance of the low-energy shoulder *A* on the main line, indicates a lower degree of oxidation for some Ti atoms and, therefore, a certain loss of oxygen from the TiO_2 layer in the process of interaction with CO molecules. This behavior may be indicative of the participation of oxygen from titanium dioxide in the process of CO oxidation on the surface of the Au/TiO_2 system. It should also be emphasized that exposure of the TiO_2 layer without deposited gold clusters to CO molecules under the conditions analogous to those described above did not change the spectrum in the way shown in Fig. 3. Thus, we assume that an important role in oxidation of CO molecules is played by the Au/TiO_x interface.

The results obtained lead to the conclusion that stoichiometry of the titanium oxide layer plays an important part in the oxidation of CO molecules on the surface of the Au/TiO_x system. The use of a TiO_x layer with the stoichiometry different from TiO_2 as an oxide substrate provides a more efficient CO oxidation than in the case of the Au/TiO_2 system. The gold–oxide interface in the Au/TiO_2 system can be regarded as a catalytically active region.

Acknowledgments. This study was performed within the framework of the scientific cooperation between the Russian Academy of Sciences and the German Service for Scientific Exchange between Academies (DAAD), project no. A9902853.

REFERENCES

1. Q. Dong, J. Wang, Y. Gao, and S. Chen, Catal. Lett. **58**, 37 (1999).
2. C. T. Campbell, Surf. Sci. Rep. **27**, 1 (1997).
3. T. Hayashi, K. Tanaka, and M. Haruta, J. Catal. **178**, 566 (1998).
4. X. Lai, T. Clair, M. Valden, and D. W. Goodman, Prog. Surf. Sci. **59**, 25 (1998).
5. J. Grunwaldt, C. Kiener, C. Woegerbauer, and A. Baiker, J. Catal. **181**, 223 (1999).
6. T. T. Magkoev and M. Song, Poverkhnost', No. 11, 45 (1999).
7. P. Lenz-Solomun and K. Christmann, Surf. Sci. **345**, 41 (1996).
8. K. Christmann, G. Ertl, and H. Shimizu, J. Catal. **61**, 397 (1990).
9. T. T. Magkoev, M.-B. Song, K. Fukutani, and Y. Murata, Surf. Sci. **363**, 281 (1996).
10. K. H. Ernst, A. Ludviksson, R. Zhang, *et al.*, Phys. Rev. B **47**, 13782 (1993).
11. L. Zhang, R. Persaud, and T. E. Madey, Phys. Rev. B **56** (16), 10549 (1997).

Translated by L. Man

Technical Physics Letters, Vol. 26, No. 10, 2000, pp. 897–899. Translated from Pis'ma v Zhurnal Tekhnicheskoĭ Fiziki, Vol. 26, No. 20, 2000, pp. 8–12.

Nonlinear Thermomagnetic Waves of Finite Amplitude in Superconductors

N. A. Taĭlanov and U. T. Yakhshiev

Department of Theoretical Physics, Institute of Applied Physics, Tashkent State University, Tashkent, Uzbekistan

e-mail: taylanov@iaph.silk.org

Received May 12, 2000

Abstract—A theoretical analysis of the dynamics of thermal and electromagnetic perturbations in a superconductor shows that nonlinear thermal and electric dissipative wave structures may form under certain conditions on the sample surface. The structures possess a finite-amplitude and propagate at a constant velocity. The appearance of these structures is qualitatively described and the wave propagation velocity is estimated. © *2000 MAIK "Nauka/Interperiodica".*

At present, superconducting systems with high critical field strengths and current densities are widely implemented in various advanced technologies. However, successful operation of the superconducting materials is only possible provided that special measures are taken to prevent a system from the thermal or magnetic breakage of superconductivity and the transition to a normal (resistive) state. For this reason, one of the main problems in the investigation of properties of superconductors is that of predicting the superconducting state breakage caused by dissipative and nonlinear effects related to viscous motions of the magnetic flux. This explains the considerable interest in the study of dissipative and nonlinear effects in superconductors that has arisen in recent years.

This work is devoted to the analysis of the nonlinear dynamics of interrelated thermal and electromagnetic perturbations in a superconductor caused by dissipative effects involved in the viscous motion of the magnetic flux. The structure and evolution of the stationary thermomagnetic waves propagating in the superconductor is studied based on a system of nonlinear equations describing dynamics of the instability development in the system studied.

The evolution of thermal and electromagnetic perturbations in a superconductor is described by a set involving the one-dimensional thermal conductivity equation [1]

$$\nu\frac{\partial T}{\partial t} = k\frac{\partial^2 T}{\partial x^2} + \mathbf{jE}, \tag{1}$$

the Maxwell equation

$$\frac{4\pi}{c^2}\frac{\partial \mathbf{j}}{\partial t} = \frac{\partial^2 \mathbf{E}}{\partial x^2}, \tag{2}$$

and the related equation of the critical state

$$\mathbf{j} = \mathbf{j}_c(T, \mathbf{H}) + \mathbf{j}_r(\mathbf{E}). \tag{3}$$

Here ν is the heat capacity, k is the thermal conductivity coefficient, $\mathbf{j}_c$ is the critical current density, and $\mathbf{j}_r$ is the current density in the resistive state.

The above system is essentially nonlinear because the right-hand part of Eq. (1) contains a term describing the Joule heat evolution in the region of a resistive phase. Such a set (1)–(3) of nonlinear parabolic differential equations in partial derivatives has no exact analytical solution.

For the automodel propagating waves of the type $\xi(x, t) = x - vt$, the initial differential Eqs. (1)–(3) acquire the following form:

$$-\nu v\frac{\partial T}{\partial \xi} = \frac{\partial}{\partial \xi}\left[k\frac{\partial T}{\partial \xi}\right] + jE, \tag{4}$$

$$\frac{\partial E}{\partial \xi} = -\frac{4\pi v}{c^2}j, \tag{5}$$

$$E = \frac{v}{c}H. \tag{6}$$

A set of boundary conditions corresponding to Eqs. (4)–(6) is as follows:

$$\begin{aligned} &T(\xi \longrightarrow +\infty) = T_0, \quad \frac{\partial T}{\partial \xi}(x \longrightarrow -\infty) = 0, \\ &E(\xi \longrightarrow +\infty) = 0, \quad E(\xi \longrightarrow -\infty) = E_e, \end{aligned} \tag{7}$$

where T_0 is the initial temperature, E_e is the strength of a constant external electric field.

1063-7850/00/2610-0897$20.00

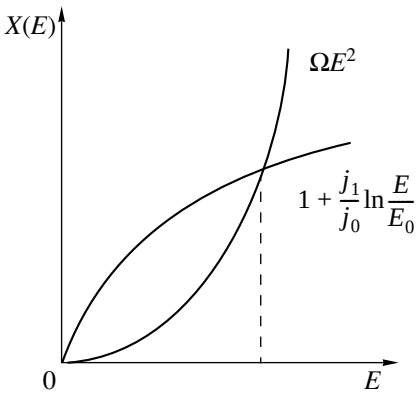

Plots of the left- and right-hand parts of Eq. (9).

In view of considerable analytical difficulties involved in solving the exact problem, we will restrict our consideration to the so-called Bean–London critical state model by assuming that $\partial j_c/\partial H = 0$ [2]. A characteristic field dependence of $j_r(E)$ in the region of sufficiently strong electric fields ($E > E_f$) can be approximated by a piecewise linear function $j_r \approx \sigma_f E$, where σ_f is the effective conductivity. In the region of small field strengths ($E < E_f$), we assume a relationship $j(E) \approx j_1 \ln(E/E_0)$ to be valid with j_1 being a characteristic local current density scatter (related to a pinning force inhomogeneity) on the order of $j_1 \approx 0.01 j_c$ and E_0 being a constant. This relationship between j and E is due to a thermoactivated flux creep discovered in the early experiments (see, e.g. [3]). The thermoactivated flux creep is a principal mechanism of the energy dissipation during the magnetic flux penetration deep into the sample. This factor must affect the character of the nonlinear thermomagnetic wave propagation in the system studied.

Excluding the variables $T(\xi)$ and $H(\xi)$, using Eqs. (4) and (6), and taking into account the boundary conditions (7), we obtain an equation describing the electric field $E(\xi)$ distribution:

$$\frac{\partial^2 E}{\partial z^2} + \beta\left[1 + \frac{j_1}{\sigma_d E}\tau\right]\frac{\partial E}{\partial z} + \beta^2\tau\left[\frac{j_0}{\sigma_d} + \frac{j_1}{\sigma_d}\ln\frac{E}{E_0}\right] = \frac{E^2}{2E_k}. \tag{8}$$

The dimensionless variables used in Eq. (8) are defined as follows:

$$z = \frac{\xi}{L}, \quad \beta = \frac{\nu t_k}{L}, \quad t_k = \frac{\nu L^2}{k},$$

$$\tau = \frac{4\pi\sigma_f k}{c^2\nu}, \quad E_k = \frac{k}{aL^2}, \quad L = \frac{cH_e}{4\pi j_0},$$

where L is the depth of the magnetic flux penetration into the sample, σ_d is the differential conductivity, a is a constant parameter, and H_e is the external magnetic field strength.

The corresponding equation of state is obtained using a relationship [4]

$$\Omega E^2 = X(E) = 1 + \frac{j_1}{j_0}\ln\frac{E}{E_0}, \tag{9}$$

where

$$\Omega = \frac{\sigma_d}{2\beta^2\tau j_0 E_k}.$$

As seen from the plots of $X(E)$ versus E (see figure), there exists a single point of intersection of the curves $y = \Omega E^2$ and $y = 1 + (j_1/j_0)\ln(E/E_0)$, which corresponds to a single stable equilibrium state. The stability of this state is determined by the sign of derivative $\partial^2 E/\partial z^2$ in the vicinity of the equilibrium point. The wave velocity v_E can be determined from Eq. (9) with an allowance for the boundary conditions:

$$v_E = \frac{L}{t_k}E_e\left[2\tau\frac{j_0 E_k}{\sigma_d}\left(1 + \frac{j_1}{j_0}\ln\frac{E_e}{E_0}\right)\right]^{-1/2}. \tag{10}$$

Now we can use Eq. (6) and readily derive an equation describing the field distribution for a nonlinear H-wave. The wave velocity v_H of this H-wave is given by the formula

$$v_H = \frac{cE}{H_e}\exp\left[\frac{\sigma_d}{2\tau j_1}E_k\left(\frac{LH_e}{ct_k}\right)^2 - \frac{j_0}{j_1}\right]. \tag{11}$$

As seen, the wave velocity exponentially increases with the field amplitude H_e. For a sufficiently small amplitude $H_e < H_a$, where

$$H_a = \frac{ct_k}{L}\left[\frac{2\tau j_0 E_k}{\sigma_d}\right]^{1/2}, \tag{12}$$

the wave velocity is negligibly small, which corresponds to the case of the thermoactivated flux creep. For $H_e = H_a$, the wave propagates at a finite constant velocity. In this case, the maximum heating of a super-

conductor in the region immediately in front of the wave is described by the relationship

$$\frac{T - T_0}{T_0} = \frac{H_e^2}{8\pi\nu T_0}. \quad (13)$$

In concluding, we must note that taking into account a nonlinear dependence of the current density j on the electric field strength E would not qualitatively change the main results, since the character of the equilibrium state on the phase plane remains essentially the same.

REFERENCES

1. I. L. Maksimov, Yu. N. Mastakov, and N. A. Taĭlanov, Fiz. Tverd. Tela (Leningrad) **28**, 2323 (1986) [Sov. Phys. Solid State **28**, 1300 (1986)].
2. C. P. Bean, Phys. Rev. Lett. **8**, 250 (1962).
3. R. G. Mints and A. L. Rakhmanov, *Instabilities in Semiconductors* (Nauka, Moscow, 1984).
4. V. I. Karpman, *Non-Linear Waves in Dispersive Media* (Nauka, Moscow, 1973; Pergamon, Oxford, 1975).

Translated by P. Pozdeev

Technical Physics Letters, Vol. 26, No. 10, 2000, pp. 900–902. Translated from Pis'ma v Zhurnal Tekhnicheskoĭ Fiziki, Vol. 26, No. 20, 2000, pp. 13–19.

Self-Organization of a Critical State and 1/*f* Fluctuations Caused by the Interaction of Phase Transitions in a Distributed System

V. N. Skokov and V. P. Koverda

Institute of Thermal Physics, Ural Division, Russian Academy of Sciences, Yekaterinburg, Russia
e-mail: skok@itp.e-burg.su

Received May 5, 2000

Abstract—A mathematical model is proposed that describes the appearance of fluctuations with a spectral density inversely proportional to the frequency as a result of the intersection of phase transitions in a spatially inhomogeneous system. The model is represented by a set of two nonlinear stochastic differential equations with mutually interacting order parameters. It is demonstrated that a random walk in the model potential field corresponding to the intersecting sub- and supercritical phase transitions may lead to the self-organization of a critical state and the appearance of fluctuations with a 1/*f* spectral density. © *2000 MAIK "Nauka/Interperiodica".*

Fluctuation processes with the power spectrum intensity inversely proportional to the frequency (flicker noise or 1/*f* noise) are observed in various processes [1–3]. Although extensive investigations into this phenomenon have been performed for many years, no commonly accepted pattern has yet been elaborated and even mechanisms leading to the appearance of fluctuations are frequently unclear. For this reason, the search for new systems featuring the flicker noise and the development of new models of this phenomenon still offer an important direction of investigation.

The interest in random processes with diverging spectral characteristics has sharply increased in recent years in connection with the discovery of the phenomenon of the self-organized critical state [4], whereby a system exhibits critical behavior in the course of its own evolution with no need of a fine adjustment of the control parameters. Low-frequency divergence of the spectral density of fluctuations is evidence that a process featuring the flicker nose possesses no characteristic time scale. This fact suggests that the system occurs in the vicinity of a critical phase transition.

Previously [5–7], we have experimentally observed fluctuations with a 1/*f* spectrum during a change in the boiling mode of liquid nitrogen on the surface of thin high-temperature superconductor films under conditions of Joule self-heating. We also reported [8] on the thermal fluctuations with 1/*f* and $1/f^2$ spectra observed in boiling water films on a vertical filament heater. It was noted that this process has much in common with the phenomenon of the self-organized critical state.

The experimental results were explained within the framework of a mathematical model [6, 7] describing nonequilibrium phase transitions in a system with lumped parameters represented by a set of two nonlinear stochastic equations:

$$\begin{aligned} \dot{\phi} &= -\phi\psi^2 + \psi + \Gamma_1(t), \\ \dot{\psi} &= -\psi\phi^2 + \gamma\phi + \Gamma_2(t), \end{aligned} \tag{1}$$

where ϕ, ψ are the interacting order parameters and $\Gamma_1(t)$, $\Gamma_2(t)$ are the Gaussian δ-correlated noise functions. A special feature of this model is that the stochastic equations describing the process contain nonpotential terms ($\gamma > 1$) taking into account the presence of external fluxes. The system essentially converts white noise into two stochastic processes with the spectral densities proportional to $1/f$ and $1/f^2$.

Recently [9], we suggested a potential point system leading to similar results. In this study, we will consider the appearance of 1/*f* fluctuations in the order parameter in a spatially distributed potential system.

Let us consider a system with the space-time evolution described by two one-dimensional stochastic equations of the diffusion type:

$$\begin{aligned} \partial\phi/\partial t &= D_1\partial^2\phi/\partial x^2 + Q_1(\phi, \psi) + \Gamma_1(x, t), \\ \partial\psi/\partial t &= D_2\partial^2\psi/\partial x^2 + Q_2(\phi, \psi) + \Gamma_2(x, t), \end{aligned} \tag{2}$$

where D_1, D_2 are the diffusion coefficients and $\Gamma_1(x, t)$, $\Gamma_2(x, t)$ are the random δ-correlation forces. This set of equations (2) is rather general and describes nonequilibrium phase transitions in many physical and chemical systems. Let us consider the case when the two characteristic spatial scales of the order parameter are significantly different, that is, $D_1/D_2 \gg 1$. The source functions characterizing interaction of the order parameters will be approximated by the expressions

1063-7850/00/2610-0900$20.00

$Q_1(\phi, \psi) = -\phi\psi^2 + \psi$, $Q_2(\phi, \psi) = -\psi\phi^2 + \phi$ [6, 7]. In this case, the set of stochastic equations acquires the following form:

$$\begin{aligned} \partial\phi/\partial t &= D_1\partial^2\phi/\partial x^2 - \phi\psi^2 + \psi + \Gamma_1(x, t), \\ \partial\psi/\partial t &= -\psi\phi^2 + \phi + \Gamma_2(x, t). \end{aligned} \tag{3}$$

This set describes a random walk in the potential

$$\Phi = \Phi_0 + \int\left\{\frac{1}{2}\phi^2\psi^2 - \phi\psi + \frac{1}{2}(\nabla\phi)^2\right\}dx \tag{4}$$

possessing a saddle at the origin of coordinates. In the absence of inhomogeneities ($\nabla\phi = 0$), the system also possesses the lines of stationary points determined by the condition $\phi\psi = 1$. Once an inhomogeneity appears in the parameter ϕ, the hyperbolas $\phi\psi = 1$ incline toward increasing parameter ψ. Figure 1 shows a phase portrait of the system obtained by numerically integrating set (3) without random sources ($\Gamma_1 = \Gamma_2 = 0$), with the dashed lines indicating separatrices. This system possesses an asymptotic solution in the form of power functions $\phi \longrightarrow t^{-1/4}$ and $\psi \longrightarrow t^{1/4}$ for $t \longrightarrow \infty$ [in contrast to the nonpotential set (1) featuring an asymptotic behavior of the type $\phi \longrightarrow t^{-1/2}$ and $\psi \longrightarrow t^{1/2}$ for $t \longrightarrow \infty$].

The physical meaning of potential (4) is readily elucidated upon accomplishing a linear transformation to the new variables $\theta = (\psi - \phi)/\sqrt{2}$, $\eta = (\phi + \psi)/\sqrt{2}$ corresponding to the phase plane rotation by $\pi/4$ (not changing the type of the potential surface). In the new variables, an expression for the potential acquires the following form:

$$\begin{aligned} \Phi(\theta, \eta) = \int\Big\{&\frac{1}{8}\theta^4 + \frac{1}{8}\eta^4 + \frac{1}{2}\theta^2 - \frac{1}{2}\eta^2 + \frac{1}{2}(\nabla\theta)^2 \\ &+ \frac{1}{2}(\nabla\eta)^2 - \frac{1}{4}\theta^2\eta^2 - \nabla\theta\nabla\eta\Big\}dx. \end{aligned} \tag{5}$$

The structure of expression (5) indicates that potential $\Phi(\theta, \eta)$ corresponds to the intersection of two phase transitions with the order parameters θ and η. Different signs of the square terms suggest that we deal with the intersection of sub- and supercritical phase transitions. The last two terms in (5) describe the interaction of the order parameters, the negative sign of the interaction term $\theta^2\eta^2$ corresponding to the absence of nonzero stationary solutions in a purely dynamic (noise-free) system.

The numerical solutions were obtained using an explicit integration scheme. The spatially distributed white noise was represented by sequences of Gaussian random numbers. The control parameters were represented by the intensities of random sources and the diffusion coefficient D_1. For a small intensity of noise, the solutions to set (3) have the form of slightly fluctuating relaxation functions $\phi(t)$ and $\psi(t)$ representing a system performing a random walk in one of the valleys (determined by the initial conditions) of the potential $\Phi(\phi, \psi)$. The process is nonstationary, and, as the random source intensity increases, the system jumps from one to another valley. Then the process becomes stationary—at least, with respect to the first two moments of the distribution function of the parameter ϕ—provided that the integration steps are finite. The transition to the stationary process is essentially due to the fact that external random forces do not allow the system to walk too far along the narrowing valleys of the potential $\Phi(\phi, \psi)$. The distribution functions of the parameters $\phi(t)$ and $\psi(t)$ possess a symmetric dome like shape and can be well approximated by the Gaussian distribution.

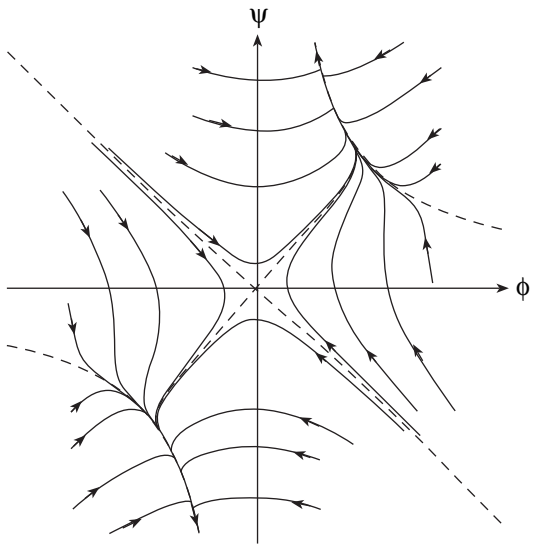

Fig. 1. A typical phase portrait of a dynamic system obtained by averaging over the spatial variable.

Using the numerically calculated realizations, we determined the corresponding spectral densities of fluctuations by the Fourier transform method. It was found that, within rather broad limits of variation of the diffusion coefficient D_1 and the intensity of random sources, the spectral density S_ϕ of the parameter ϕ was inversely proportional to the frequency. At the same time, the frequency dependence of the spectral density S_ψ is inversely proportional to the frequency square. Figure 2 shows the $S_\phi(f)$ function obtained upon spatial averaging of the corresponding spectra. Note that the spectra of fluctuations of the variable ϕ at each point in the space also exhibit a characteristic 1/f shape. The inset in Fig. 2 shows a typical space-averaged realization. The numerical data presented in Fig. 2 were obtained by integrating over 65540 time steps and 32 space steps with $dt = 0.05$ and $dx = 0.8$, respectively, with the diffusion coefficient $D_1 = 0.4$, the intensity of

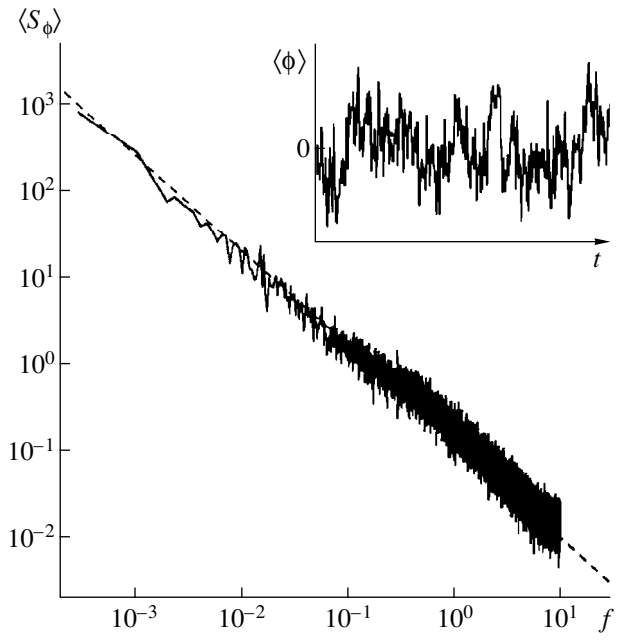

Fig. 2. The space-averaged spectral density $\langle S_\phi \rangle$ of fluctuations in the parameter $\langle \phi \rangle$. The inset shows the corresponding realization. The dashed line represents the function $\langle S_\phi \rangle \sim 1/f^{1.09}$.

random sources $\sigma = 3$, and zero initial and boundary conditions.

As seen from Fig. 2, the $1/f$ law is obeyed within a frequency interval covering more than four orders of magnitude. This range can be expanded to follow the diverging low-frequency characteristic, provided that an n-fold increase in the number of integration steps is accompanied by the $\sqrt{n}$-fold decrease in the temporal integration step and the $\sqrt{n}$-fold increase in the intensity of random sources. The spectrum of the parameter ψ is described by the function $S_\psi(f) \sim 1/f^2$.

It should be noted that the above results correspond to the case when one of the diffusion coefficients (here, D_2) can be taken equal to zero. The results of our numerical analysis showed that, as the D_2 value increases from 0 to D_1, the $S_\phi(f)$ and $S_\psi(f)$ curves change in the low-frequency range to exhibit horizontal "shelves" characteristic of the Lorentzian spectra. If the two diffusion coefficients are equal, the parameters ϕ and ψ coincide and the set (3) becomes equivalent to the Ginzburg–Landau equation for the first-order phase transition in a system with a single order parameter.

The diverging spectral characteristics of fluctuations, as well as the power character of the relaxation functions, are indicative of the critical behavior of the system studied. This behavior is observed in a broad range of the control parameters and needs no fine adjustment of these parameters. The system falls in a critical state as a result of intersection and interaction of the nonequilibrium sub-and supercritical phase transitions. In this context, we may speak of the self-organization of a critical state.

Thus, the random walk in a two-valley potential with strongly different diffusion coefficients leads to the appearance of fluctuations with a $1/f$ spectrum. The intersection and interaction of the nonequilibrium sub- and supercritical phase transitions, as well as processes of the type described by the set of reaction-diffusion equations (2), are frequently encountered in practice. For this reason, the proposed model can be used to explain the $1/f$ noise observed in various systems and provides for a new approach to the phenomenon of self-organized critical behavior.

Acknowledgments. The work was supported by the Russian Foundation for Basic Research, project no. 00-02-16288.

REFERENCES

1. Sh. M. Kogan, Usp. Fiz. Nauk **145** (2), 285 (1985) [Sov. Phys. Usp. **28**, 170 (1985)].
2. G. P. Zhigal'skiĭ, Usp. Fiz. Nauk **167** (6), 624 (1997).
3. Yu. L. Klimontovich, *Statistical Theory of Open Systems* (Yanus, Moscow, 1995; Kluwer, Dordrecht, 1995).
4. P. Bak, C. Tang, and K. Wiesenfeld, Phys. Rev. A **38** (1), 364 (1988).
5. V. P. Koverda, V. N. Skokov, and V. P. Skripov, Pis'ma Zh. Éksp. Teor. Fiz. **63** (9), 739 (1996) [JETP Lett. **63**, 775 (1996)].
6. V. P. Koverda, V. N. Skokov, and V. P. Skripov, Zh. Éksp. Teor. Fiz. **113** (5), 1748 (1998) [JETP **86**, 953 (1998)].
7. V. P. Koverda and V. N. Skokov, Physica A (Amsterdam) **262**, 376 (1999).
8. V. N. Skokov, V. P. Koverda, and A. V. Reshetnikov, Pis'ma Zh. Éksp. Teor. Fiz. **69** (8), 590 (1999) [JETP Lett. **69**, 636 (1999)].
9. V. N. Skokov and V. P. Koverda, Pis'ma Zh. Tekh. Fiz. **25** (9), 9 (1999) [Tech. Phys. Lett. **25**, 341 (1999)].

Translated by P. Pozdeev

Technical Physics Letters, Vol. 26, No. 10, 2000, pp. 903–906. Translated from Pis'ma v Zhurnal Tekhnicheskoĭ Fiziki, Vol. 26, No. 20, 2000, pp. 20–27.

The Low-Temperature Electric Conductivity of YBaCuO and LaSrMnO Dielectric Films Obtained by a Pulsed Laser Sputter Deposition Technique

V. D. Okunev*, N. N. Pafomov*, A. Abaleshev*, H. Belska-Lewandowska, P. Gierlowski**, A. Klimov**, and S. Lewandowski****

** Donetsk Physicotechnical Institute, National Academy of Sciences of Ukraine, Donetsk, Ukraine*

*** Institute of Physics, Polish Academy of Sciences, Warsaw, Poland*

e-mail: okunev@host.dipt.donetsk.ua

Received May 6, 2000

Abstract—We have studied the electric conductivity of YBaCuO and LaSrMnO dielectric films obtained by pulsed laser sputtering of targets possessing metallic conductivity. The plots of the sample resistance versus temperature $R = R(T)$ measured at $T < T_{cr}$ (T_{cr} = 160–240 K) exhibit regions where R is independent of the temperature. This phenomenon is probably related to manifestations of the quantum confinement effects upon the conversion of small grains into quantum dots. In the region of $T < T_{cr}$, the electric conductivity of the system is determined by a mechanism of the phononless electron tunneling with participation of the atomic-type states belonging to small grains (clusters) featuring metallic conductivity in the amorphous matrix. © *2000 MAIK "Nauka/Interperiodica".*

In recent years, increased attention of researchers has been drawn to the properties of manganates of the LaSrMnO type possessing giant magnetoresistance. This is reflected, in particular, by an increasing number of publications devoted to the mechanism of electric conductivity in these compounds [1–7]. Prokhorov *et al.* [5] recently reported on the temperature dependence of the electric resistance of thin $Pr_{0.65}Ca_{0.35}MnO_3$ films obtained by method of pulsed laser sputter deposition. The observed behavior was untypical of solids, showing a temperature coefficient of resistance tending to zero in the range of $T < 130$ K. Based on the concept of Gor'kov [2, 8] concerning the possibility of a "spray" or "droplet" phase formation, the data obtained in [5] were interpreted by assuming that the samples studied represent a dielectric matrix with metallic inclusions (or small-size ferromagnetic clusters in a paramagnetic matrix). The presence of regions with a constant resistance $R(T)$ = const ($\rho \approx 10^4$ Ω cm) was attributed to magnetic ordering of the $Pr_{0.65}Ca_{0.35}MnO_3$ films at low temperatures.

Without calling for the revision of the experimental data interpretation presented in [5], we would like to emphasize some general trends manifested in the electrical properties of dielectric films obtained by pulsed laser sputtering of the targets possessing metallic conductivity. Previously [9], we reported on the presence of analogous regions in the $R(T)$ curves for amorphous YBaCuO films (the measurements were performed on samples with planar electrode geometry) containing nanocrystalline clusters with a metallic spectrum.

Figure 1 shows the temperature variation of the resistance of YBaCuO films obtained by sputtering a stoichiometric target with radiation of an excimer laser (KrF, λ = 248 nm, $\tau \approx$ 25 ns, Φ = 1.5 J/cm^2 [9]) and depositing the sputtered material onto glass substrates at $T \simeq 300$ K. The regions where the sample resistance is independent of the temperature are observed in the $R(T)$ curves of both planar samples (Fig. 1, curves *1–3*) and sandwich structures (curve *4*). As is clearly seen from these data, the presence of horizontal portions is not related to the possible shunting effect of the film–substrate interface or the surface contamination of high-resistivity layers. The electric conductivity of the films remains unchanged as the temperature decreases down to T = 4.2 K (see the inset in Fig. 1). For the samples free of crystalline clusters, the R versus T curves obey the Mott law $R(T) \sim \exp[(T_0/T)^{1/4}]$ [10].

Our subsequent investigations devoted to the electrical properties of high-resistivity LaSrMnO films with an amorphous structure obtained by the same pulsed laser sputter deposition technique showed evidence of the analogous phenomenon in virtually the same temperature interval. Figure 2 presents the temperature variation of the resistance of samples obtained by sputtering of a $La_{0.6}Sr_{0.2}Mn_{1.2}O_3$ target (one of the most frequently employed compositions for this system) and deposition on $Nd_3Ga_5O_{12}$ substrates heated to various temperatures. In the temperature interval T_s = 600–650°C, the system exhibits a phase transition from amorphous to crystalline state. As a result the electric conductivity increases by 5–9 orders of magnitude, depending on the

1063-7850/00/2610-0903$20.00 © 2000 MAIK "Nauka/Interperiodica"

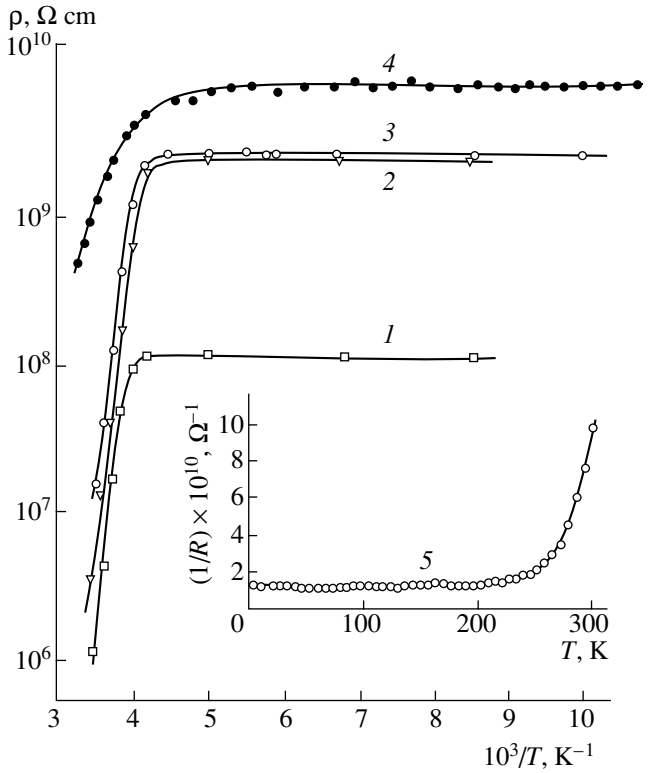

Fig. 1. The plots of resistivity versus temperature for the amorphous YBaCuO films obtained by pulsed laser sputtering of an $YBa_2Cu_3O_{7-\delta}$ target: (*1–3*) samples with a planar electrode geometry, the YBaCuO film thickness $l = 2.5 \times 10^{-4}$ cm, and the interelectrode spacing 0.3 cm, measured at an electric field strength of $E = 3 \times 10^2$ V/cm; (*4, 5*) sandwich structure (Ag–*a*-YBaCuO–Cr–glass) with the YBaCuO film thickness $l = 5 \times 10^{-5}$ cm and the cross section area 6×10^{-5} cm^2, measured at an electric field strength of 2×10^4 V/cm. Curve *5* in the inset shows the temperature variation of resistivity for a sandwich structure measured in the low-temperature range.

temperature of measurements. The temperature dependence of the resistance of a film with crystalline structure exhibits a characteristic nonmonotonic behavior with a maximum in the vicinity of the Curie temperature [1–4, 6, 7]. From the standpoint of this study of special interest are the high-resistivity samples obtained at lower substrate temperatures (T_s = 550, 600°C) featuring the regions with $R(T)$ = const. The temperature of the transition from the state with $R(T)$ = const to the regime of activation conductivity ($T_{cr} \sim$ 160 K) is somewhat lower in this system than in the YBaCuO films where T_{cr} = 180–240 K.

Note that in all the cases mentioned above (that is, in three different metal oxide systems YBaCuO, PrCaMnO, LaSrMnO) the regions of $R(T)$ = const are observed for dielectric films obtained by pulsed laser sputter deposition. Moreover, it is known that the dielectric matrices of all these films contain inclusions (crystalline clusters) possessing metallic conductivity. In our opinion, a relationship between the appearance of the regions with $R(T)$ = const and the magnetic ordering in PrCaMnO and LaSrMnO films has a secondary character and is due to the effect of the magnetic ordering on the process of cluster transition to a state with metallic spectrum. In the general case, the magnetic state of a system is not of principal significance. We must also bear in mind that the dielectric films of different compositions were obtained using targets possessing metallic conductivity. This is an important factor since, for the given film preparation technique, the nanocrystalline clusters with metallic conductivity are not necessarily formed immediately in the laser torch. The origin of the clusters may as well be related to the explosion character of interaction of the high-energy laser radiation with the substance and/or to the secondary processes involved in the target sputtering (e.g., the shockwave generation and propagation [9]), in which cases the clusters represent essentially a form of existence of the target fragments.

In elucidating the mechanism of electric conductivity in the films in the regions of $R(T)$ = const, we have to recognize that the systems studied are sharply inhomogeneous, which, according to a classification commonly accepted, belong to granulated metals on the dielectric side of a dielectric–metal junction. The electrical properties of such stochastically inhomogeneous systems are determined to a considerable extent by the process of electron tunneling between the metal granules distributed in a dielectric matrix. The tunneling transitions in these systems, similar to those in many other solid objects, are temperature-dependent and proceed with the participation of phonons. The results of extensive investigations conducted in recent decades [11–13] show that the resistance of granulated media varies with the temperature, as a rule, according to the following law:

$$R(T) \sim \exp[(T_0/T)^{1/2}]. \quad (1)$$

Taking into account that the regions of $R(T)$ = const were observed in the materials occurring in different structural states and possessing different magnetic and electrical properties, we may conclude that the only conduction mechanism capable of providing for the appearance of regions with $R(T)$ = const is that based on the electron tunneling between granules with metallic conductivity but not involving phonons.

This possibility is offered by a classical quantum-mechanical mechanism of electron tunneling with the participation of discrete atomic-type states. This discrete spectrum may be realized upon the conversion of clusters into quantum dots. This spatial confinement of the charge carriers in all three dimensions leads to the realization of a limiting case of quantization with a most pronounced modification of the electron properties of a given material: the ideal quantum dots possess a δ-shaped energy spectrum similar to that of an isolated atom [14, 15]. Indeed, the regions in which the

resistivity ρ is independent of the temperature T are observed only in the cases where the X-ray diffraction data [9] indicate the presence of small clusters (on the order of several tens of Ångströms). Previously [9], we presented evidence in favor of the effect of the quantum confinement, taking place in clusters possessing metallic conductivity, on the optical properties of amorphous YBaCuO films. Use of the quantum confinement effects is an important trend in the development of modern semiconductor electronics [14, 15]. A distance between the energy levels in quantum-confined systems is determined by the size of clusters d and by the density of states at the Fermi level $N(0)$ [12]:

$$\Delta \approx [d^3 N(0)]^{-1}. \quad (2)$$

For small granules with a size of 10–40 Å composed of atoms of the usual metals such as Au, Ni, Pt, and W, the distance between energy levels in the quantum-confined state does not exceed several tens of meV [17]. Therefore the tunneling transitions with thermal activation of electrons on various energy levels are really possible in these systems in the temperature range studied ($4.2 < T < 300$ K). In our case, the granules are only formally classified as metals and more likely represent strongly degenerate semiconductors with metallic conductivity [18, 19]. The density of states at the Fermi level and the concentration of free holes can be 1–2 orders of magnitude lower than those in usual metals. Moreover, a considerable decrease in the charge carrier concentration and, accordingly, in the density of states at the Fermi level may be additionally caused by the hole trapping on the surface states [9]. The difference between the energy levels in these systems may be greater by more than one order of magnitude as compared to the Δ value in the granules of classical metals.

There were attempts [16, 17] at calculating the electric conductivity of granulated metals based on the discrete character of the energy spectrum of small granules. These calculations were aimed at eliminating the artificial limitations on the system parameters related mainly to the assumption of a constant relationship between the size and spacing of granules [11] used to derive formula (1). However, it was demonstrated [13] that relationship (1) can be derived assuming only a sufficiently large scatter of granules (granules of the same size may feature the tunneling transitions not involving phonons).

The tunneling transitions must apparently depend on the relationship between the thermal energy, the distance between energy levels Δ in a quantum-confined system, and the electric-charge energy E_c. As is known [11–13],

$$E_c \approx e^2/\varepsilon d. \quad (3)$$

The value of Δ increases with decreasing granule size by the law $\Delta \sim 1/d^3$, while E_c increases at a markedly slower rate ($E_c \sim 1/d$). Therefore, a system of granules with small size d may satisfy both the requirements

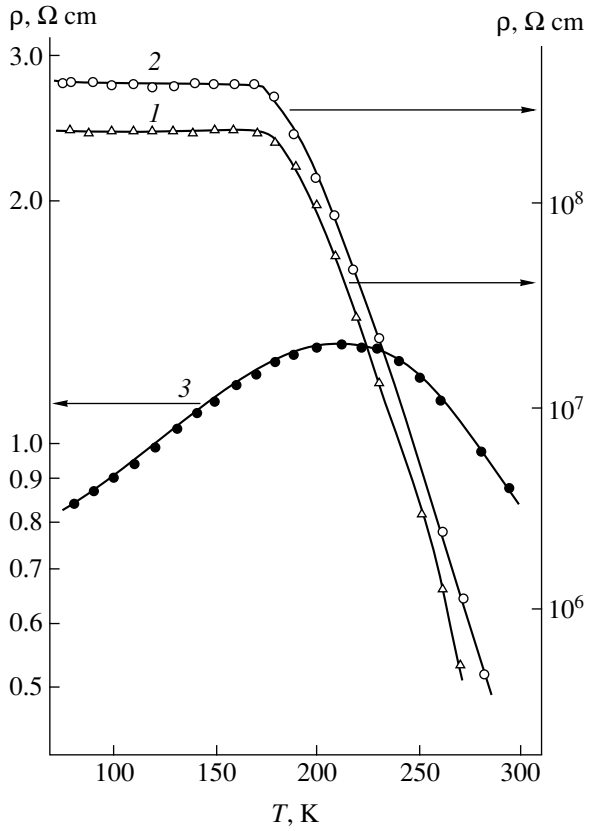

Fig. 2. The plots of resistivity versus temperature for the LaSrMnO film samples with planar electrode geometry deposited at various substrate temperatures T_s = 550 (*1*); 600 (*2*); 650°C (*3*). The LaSrMnO film thickness $l = 1 \times 10^{-5}$ cm; the interelectrode spacing 0.3 cm; electric field strength applied during the resistivity measurements $E = 1 \times 10^3$ (*1*, *2*); 3.3 V/cm (*3*).

$\Delta \gg kT$, $E_c \gg kT$ and the condition $\Delta \gg E_c$. This implies that the electric conductivity of the system caused by the electron tunneling with participation of the atomic-type states belonging to small clusters possessing metallic conductivity is independent of the temperature at $T < T_{cr}$. A certain contribution may be probably due to the effects caused by the resonance tunneling of electrons involving clusters of ultimately small dimensions and localized states of the matrix [20]. The phonon spectrum of clusters is also subject to quantization [21], which additionally hinders the tunneling transitions with the participation of phonons. However, as the temperature increases and the thermal energy becomes comparable with the distance between the energy levels of quantum dots, the energy spectrum acquires a quasi-discrete character ($\Delta \approx kT$) and the system passes into a regime of thermoactivated conductivity.

REFERENCES

1. É. L. Nagaev, Usp. Fiz. Nauk **166** (8), 833 (1996) [Phys. Usp. **39**, 781 (1996)].

2. L. P. Gor'kov, Usp. Fiz. Nauk **168** (6), 665 (1998).
3. A. Urushibara, Y. Moritomo, T. Arima, *et al.*, Phys. Rev. B **51** (20), 14103 (1995).
4. A. E. Kar'kin, D. A. Shulyatev, A. A. Arsenov, *et al.*, Zh. Éksp. Teor. Fiz. **116** (2), 671 (1999) [JETP **89**, 358 (1999)].
5. V. G. Prokhorov, G. G. Kaminskiĭ, V. S. Flis, and Yong Pak Lee, Fiz. Nizk. Temp. **25** (10), 1060 (1999) [Low Temp. Phys. **25**, 792 (1999)].
6. V. A. Berezin, V. I. Nikolaĭchik, V. T. Volkov, *et al.*, Pis'ma Zh. Tekh. Fiz. **25** (10), 42 (1999) [Tech. Phys. Lett. **25**, 398 (1999)].
7. O. Yu. Gorbenko, R. V. Demin, A. R. Kaul', *et al.*, Fiz. Tverd. Tela (St. Petersburg) **40** (2), 290 (1998) [Phys. Solid State **40**, 263 (1998)].
8. L. P. Gor'kov and A. V. Sokol, Pis'ma Zh. Éksp. Teor. Fiz. **46** (7), 333 (1987) [JETP Lett. **46**, 420 (1987)].
9. V. D. Okunev, Z. A. Samoilenko, V. M. Svistunov, *et al.*, J. Appl. Phys. **85** (10), 7282 (1999).
10. V. D. Okunev and N. N. Pafomov, Pis'ma Zh. Tekh. Fiz. **17** (17), 1 (1991) [Sov. Tech. Phys. Lett. **17**, 315 (1991)].
11. P. Sheng, B. Abeles, and Y. Arie, Phys. Rev. Lett. **31** (1), 44 (1973).
12. B. I. Belevtsev, Yu. F. Komnik, and A. V. Fomin, Fiz. Nizk. Temp. **12** (8), 821 (1986) [Sov. J. Low Temp. Phys. **12**, 465 (1986)].
13. E. Z. Meĭlikhov, Zh. Éksp. Teor. Fiz. **115** (4), 1484 (1999) [JETP **88**, 819 (1999)].
14. Zh. I. Alferov, Fiz. Tekh. Poluprovodn. (St. Petersburg) **32** (1), 3 (1998) [Semiconductors **32**, 1 (1998)].
15. N. N. Ledentsov, V. M. Ustinov, V. A. Shchukin, *et al.*, Fiz. Tekh. Poluprovodn. (St. Petersburg) **32** (4), 385 (1998) [Semiconductors **32**, 343 (1998)].
16. E. Simánek, Solid State Commun. **40** (11), 1021 (1981).
17. M. Mostefa and G. Olivier, J. Phys. C **18** (1), 93 (1985).
18. Gang Yu and Alan J. Heeger, Int. J. Mod. Phys. B **7** (22), 3751 (1993).
19. V. D. Okunev, Z. A. Samoilenko, A. Abal'oshev, *et al.*, Appl. Phys. Lett. **75** (13), 1949 (1999).
20. L. V. Iogansen, Zh. Éksp. Teor. Fiz. **45** (2), 207 (1963) [Sov. Phys. JETP **18**, 146 (1963)].
21. B. A. Tavger and V. Ya. Demikhovskiĭ, Usp. Fiz. Nauk **96** (1), 61 (1968).

Translated by P. Pozdeev

Technical Physics Letters, Vol. 26, No. 10, 2000, pp. 907–909. Translated from Pis'ma v Zhurnal Tekhnicheskoĭ Fiziki, Vol. 26, No. 20, 2000, pp. 28–33.

Magnetostatic Surface Waves on a Moving Domain Boundary in a Garnet Ferrite Crystal

E. A. Vilkov

Ul'yanovsk Department, Institute of Radio Engineering and Electronics, Russian Academy of Sciences, Ul'yanovsk, Russia

Received January 18, 2000

Abstract—The behavior of magnetostatic surface waves on a domain boundary uniformly propagating in a garnet ferrite crystal was theoretically studied. It was established that the boundary motion, while not affecting the magnetostatic surface wave structure, may significantly modify the wave spectrum. © *2000 MAIK "Nauka/Interperiodica".*

At present, devices employing the magnetostatic and spin surface waves in layered structures of magnetic materials are widely used in data processing systems [1]. As is known, the magnetostatic surface waves (MSSWs) can be effectively trapped by the domain boundaries (DBs) in ferromagnetic materials [2, 3]. This, in view of the ability of DBs to move over a crystal under the action of external control, poses an important task of evaluating the waveguide properties of DBs under the conditions of their controlled motion. In particular, study of the spectral properties of MSSWs on moving DBs is of interest from the standpoint of using this phenomenon in controlled data transfer channels. A similar possibility of using domain boundaries moving in a ferroelectric material for the signal transfer with a surface electrosonic wave was recently demonstrated in [4].

In this work, we have studied for the first time the behavior of an MSSW on a 180°-DB of the Bloch wall type uniformly moving in a garnet ferrite crystal. It was suggested that, in the laboratory (crystallographic) frame $x0yz$, the DB lies in the (001) crystal plane and moves perpendicularly to the spontaneous magnetization axis $M_0^{(j)}$ in the domains $M_0^{(1)} \uparrow\downarrow M_0^{(2)} \parallel [001] \parallel 0z$ ($j = 1, 2$ is the domain number) with the current coordinate $y = y_D = V_D t$ (t is the time, V_D is the domain boundary velocity). Accordingly, the spontaneous magnetizations $M_0^{(j)}$ and the internal magnetic field strengths $H_i^{(j)}$ in the domains are assigned the following values:

$$M_0^{(j)} = (-1)^{j+1} M_0, \quad H_i^{(j)} = (-1)^{j+1} H_i, \quad M_0 > 0, \quad H_i > 0, \tag{1}$$

where $j = 1$ for $y > y_D$ and $j = 2$ for $y < y_D$. In addition, we assume that the crystal occurs in a state far from a phase transition and the velocity V_D is not very close to the transverse sound velocity c_t in the ferrite studied, which allows us to ignore the structural transformation processes in the moving DB. Finally, we also assume that MSSWs trapped by DBs propagate along the x-axis and can be described within the framework of a non-exchange magnetostatic approximation, in which case $k\Delta \ll 1$ (Δ is the DB thickness) and the DB can be considered as a geometric—thin and structureless—surface.

To construct a solution for this problem, we will pass from the laboratory frame of reference to the DB rest frame $\tilde{x}0\tilde{y}\tilde{z}$. Since $V_D \ll c$ (c is the speed of light), we may use the Galilean transformation:

$$\tilde{y} = y - V_D t, \quad \tilde{x} = x, \quad \tilde{t} = t. \tag{2}$$

Accordingly, the differential operators are transformed by the following scheme:

$$\frac{\partial}{\partial y} \longleftrightarrow \frac{\partial}{\partial \tilde{y}}, \quad \frac{\partial}{\partial x} \longleftrightarrow \frac{\partial}{\partial \tilde{x}}, \quad \frac{\partial}{\partial t} \longleftrightarrow \frac{\partial}{\partial \tilde{t}} - V_D \frac{\partial}{\partial \tilde{y}}. \tag{3}$$

In the selected MSSW propagation geometry, the magnetic potentials φ_j satisfy the Laplace equation [1]

$$\nabla^2 \varphi_j = 0, \tag{4}$$

which, by virtue of (3), is invariant with respect to the transformation (2). A solution to Eq. (4), where ∇ is the Hamiltonian operator in the $\tilde{x}0\tilde{y}$ plane, can be represented in the following form:

$$\varphi_j = A_j \exp i(k\tilde{x} - \Omega\tilde{t}) \exp[(-1)^j k\tilde{y}], \tag{5}$$

where Ω is the MSSW frequency in the DB rest frame. The signs of the MSSW boundary localization coefficient k were selected so as to ensure that the solution would be limited inside the domains.

Equation (4) has to be supplemented by the boundary conditions of continuity for the normal component of the magnetic potential

$$\varphi_1\big|_{\tilde{y}=0} = \varphi_2\big|_{\tilde{y}=0}, \tag{6}$$

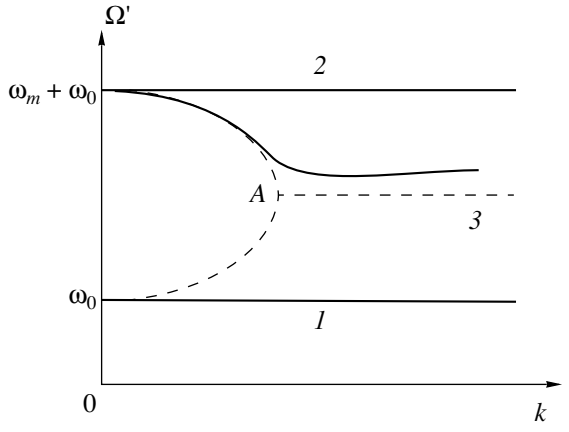

Fig. 1. Qualitative pattern of the spectrum of MSSWs on moving DBs.

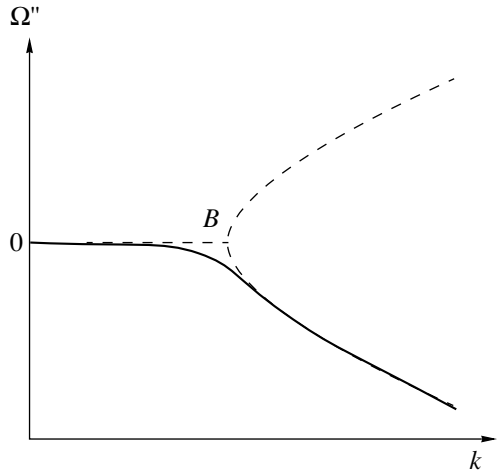

Fig. 2. Qualitative pattern of the damping coefficient for MSSWs on moving DBs.

and for the normal component of the magnetic induction

$$-\mu^{(1)}\frac{\partial\varphi_1}{\partial\tilde{y}}-\mu_{yx}^{(1)}\frac{\partial\varphi_1}{\partial\tilde{x}}\bigg|_{\tilde{y}=0}=-\mu^{(2)}\frac{\partial\varphi_2}{\partial\tilde{y}}-\mu_{yx}^{(2)}\frac{\partial\varphi_2}{\partial\tilde{x}}\bigg|_{\tilde{y}=0}. \quad (7)$$

Here

$$\mu^{(j)}=\frac{\omega_0\omega_m}{\omega_0^2-[\Omega+(-1)^{j+1}iV_Dk]^2},$$

$$\mu_{yx}^{(j)}=\frac{(-1)^{j+1}i\omega_m[\Omega+(-1)^{j+1}iV_Dk]}{\omega_0^2-[\Omega+(-1)^{j+1}iV_Dk]^2}$$

are the magnetic permeability tensor in the DB rest frame, $\omega_0=\gamma H_i$, $\omega_m=\gamma M_0$, and γ is the magnetomechanical ratio. Substituting expression (5) into Eqs. (6) and (7) and using the condition of solvability of the set of homogeneous algebraic equations with respect to amplitudes A_1 and A_2, we obtain the following dispersion relation for MSSWs on a moving DB:

$$\Omega=\omega_0+\frac{\omega_m}{2}\pm\sqrt{\frac{\omega_m^2}{4}-V_D^2k^2}. \quad (8)$$

As seen from formula (5) and Eq. (8), the MSSW structure is analogous to that of a usual collinear ($k\parallel 0\tilde{x}$) surface wave. In contrast to the case of a surface electrosonic wave in a ferroelectric [4], the MSSW front does not rotate in the direction of the DB motion, remaining perpendicular to the boundary. Figure 1 (dashed curve) shows a typical spectrum of MSSWs (with neglect of losses) on a moving DB, constructed in the plane of spectral variables k, $\Omega'=\mathrm{Re}(\Omega)$. Solid straight lines *1* and *2* represent the frequency doublet ω_0, $\omega_0+\omega_m$ corresponding to an MSSW on an immobile DB. This doublet is obtained from the spectrum of magnetostatic waves in a periodic domain structure [2, 3] in the high-frequency limit (lone domain boundary). It should be noted that Gilinskiĭ and Mints [2] called (without any justification) for the spectral line *1* ($\Omega'=\omega_0$) of the doublet to be rejected from the solution.

The DB motion eliminates the monochromaticity of the spectral lines and imparts a signal character to the MSSW propagation. The dispersion branches of the solution exhibit monochromatic closure behind a root point of the spectrum (8) with the coordinates ($\Omega'=\omega_0+\omega_m/2$, $k=\omega_m/2V_D$) to form a spectral line *3* at a frequency $\Omega'=\omega_0+\omega_m/2$. In Fig. 2, showing the plots of $\Omega''=\mathrm{Im}(\Omega)$ corresponding to the spectral curves of Fig. 1, point *A* is represented by the branching point *B*.

In order to describe the behavior of the MSSW spectra in the vicinity of the root singularities, it is a common practice to introduce losses inherent in real systems. Using this approach, we perform the transformation $k\longrightarrow k(1+i\alpha)$, with the small parameter $\alpha\ll 1$ determining the level of magnetic losses, and arrive at the dispersion functions $\Omega'(k)$ and $\Omega''(k)$ depicted by solid curves in Figs. 1 and 2. It should be noted that Fig. 1 presents only a physical branch of the solution, into which the spectral line *2* transforms due to the boundary motion and the presence of losses. In Fig. 2, this branch corresponds to the portion of the curve $\Omega''(k)<0$ describing damped magnetooptical oscillations. This result justifies the necessity of rejecting the spectral line *1* in Fig. 1 that was stipulated in [2]: once the DB motion and losses are taken into account, this spectral line transforms into another branch of the solution $\Omega'(k)$, corresponding to $\Omega''(k)>0$, which represents increasing magnetostatic oscillations that cannot be physically realized under the conditions studied.

In the garnet ferrite crystals, $\omega_m\sim 10^{10}$ s^{-1} and (for the practically attainable velocities $V_D\sim 10^5$ cm/s), the root singularity of the spectrum (8) falls within the region of magnetostatic wavenumbers $k<10^5$ cm^{-1}.

These conditions are expected to lead to the most significant changes in the MSSW spectrum as a result of the DB motion, which might be of interest from the standpoint of applications. In particular, by controlling the DB motion, we can modify, in a controlled manner, a delay in the signal carried by MSSWs predominantly on the descending part of the $\Omega'(k)$ curve (Fig. 1), that is, in the region of anomalous dispersion. The vicinity of the root singularity in the dissipation-free spectrum (8) of MSSWs on moving DBs is also of interest due to the fact that, according to Eq. (5), this region is characterized by a minimum scale (determined by the wavelength) of the boundary localization of MSSWs relative to the geometric size of the garnet ferrite crystal. This circumstance may provide for the practical realization of the effect of MSSW translation by DBs moving over the crystal. Note that these results remain valid when the consideration is conducted in the laboratory frame of reference.

Acknowledgments. The author is grateful to V.G. Shavrov and N.S. Shevyakhov for problem formulation and supervision. The work was supported by the "Integration" State Program, project no. A0066.

REFERENCES

1. G. A. Vugal'ter and I. A. Gilinskiĭ, Izv. Vyssh. Uchebn. Zaved., Radiofiz. **32** (10), 1187 (1989).
2. I. A. Gilinskiĭ and R. G. Mints, Zh. Éksp. Teor. Fiz. **59** (10), 1239 (1970).
3. M. A. Sigal, Zh. Tekh. Fiz. **59** (10), 137 (1989) [Sov. Phys. Tech. Phys. **34**, 1173 (1989)].
4. N. S. Shevyakhov, Akust. Zh. **45** (4), 570 (1999) [Acoust. Phys. **45**, 509 (1999)].

Translated by P. Pozdeev

Technical Physics Letters, Vol. 26, No. 10, 2000, pp. 910–912. Translated from Pis'ma v Zhurnal Tekhnicheskoĭ Fiziki, Vol. 26, No. 20, 2000, pp. 34–39.

The Josephson Effect in Metal–PDMS–Metal Structures

A. N. Ionov and V. A. Zakrevskiĭ

Ioffe Physicotechnical Institute, Russian Academy of Sciences, St. Petersburg, 194021 Russia

Received May 25, 2000

Abstract—We report on the Josephson effect observed for the first time in a superconductor–poly(dimethylsiloxane)– superconductor structure. © *2000 MAIK "Nauka/Interperiodica".*

It was reported [1] that 5–12 μm thick poly(dimethylsiloxane) (PDMS) layers not subjected to any preliminary treatments exhibited high but unstable room-temperature conductivity. When an external voltage below 1 V was applied to a PDMS sample, the resistance exhibited random variations from 10^9 to 0.5 Ω. In the low-resistance (high-conductivity) state, the total resistance of the metal–PDMS–metal structure was independent of the PDMS film area and thickness.

Previously, we demonstrated that a stable high-conductivity state can be observed in thin-film samples of some thermostable polymers of the polyarylene group, such as poly(diphenylenephthalide) [2], and polyimides [3] placed between metal electrodes. This state was observed even in the absence of a specially applied electric field, provided that the film thickness did not exceed 1.5 μm. A small external uniaxial pressure applied to the structure did not affect the polymer film properties, and it was only necessary to improve the contact between polymer and metal electrodes. It was also found that sandwich structures comprising a thin film of an amorphous polyimide between superconductor layers feature the Josephson effect [3]. It was also of interest to study the effect of a magnetic field on the properties of sandwich structures with PDMS.

PDMS is an organosilicon polymer with the formula $[–Si(CH_3)_2–O–]_n$ that occurs at room temperature in a high-elasticity (rubberlike) state.[1] In order to prevent the material from flowing out of the interelectrode space, a 1–3 μm thick ring-shaped dielectric layer with an inner diameter of 2.5 mm was deposited onto one of the electrodes. Thus, the polymer studied was confined within a cavity formed by the electrode surfaces and the inner wall of the dielectric ring.

The electrodes were made of a massive pure tin (99.99% Sn) and had a thickness of 2.0 mm and a diameter of 12 mm. The electrode surface roughness measured with a MII-4 interference microscope did not exceed 0.08 μm. Note that a high external mechanical pressure (100 times that used in the experiments with PDMS) applied to electrodes in the absence of a polymer sample did not lead to the shortening of the electrodes. The experiments with PDMS showed that the structures with a dielectric ring (and, hence, the PDMS film) thickness of 1.5 μm and below exhibit a stable high-conductivity state for an applied electric field strength not exceeding 40 V/cm.

Now we will consider the results of the low-temperature experiments with the Sn–PDMS–Sn structures in the temperature range where tin occurs in a superconducting state (the critical temperature for this metal is T_c = 3.72 K). Methods used for the temperature and resistance measurements were analogous to those described elsewhere [2, 3].

Figure 1 shows a temperature dependence of the resistance $R(T)$ of a Sn–PDMS–Sn structure. A significant decrease in the sample resistance begins in the region of 3.65–3.75 K, and then the resistance drops with the temperature down to a technical zero determined by the sensitivity of the measuring equipment. A similar $R(T)$ behavior was previously observed for poly(diphenylenephthalide), an amorphous polyimide, and an oxidized atactic poly(propylene) [2–4]. As seen from Fig. 1, the superconducting transition is blurred

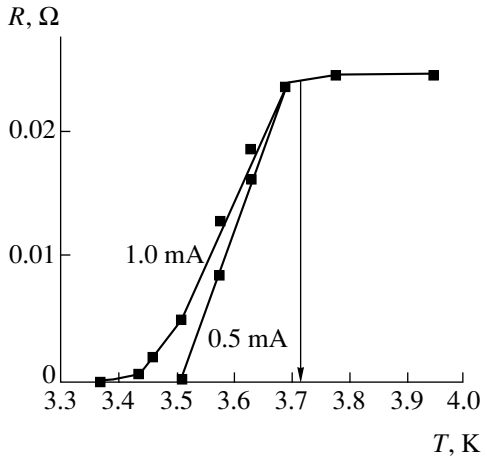

Fig. 1. Temperature dependence of the resistance of a Sn–PDMS–Sn structure measured at two values of the current.

[1] Some of our experiments were performed with a material possessing a molecular weight of 250 000 that was kindly provided to us by I.S. Shlimak.

within a certain temperature interval rather than being sharp as in the system of two tin electrodes in direct contact (in the latter case, the superconductivity appears sharply at $T = T_c$ as indicated by the vertical arrow). As is known, the temperature blurring is also characteristic of very thin superconducting filaments or small metal particles, provided that their diameter d is much smaller than the coherence length ξ_0 of the Cooper pair (for Sn, $\xi_0 = 250$ nm [5]). This fact suggests that the polymer may contain thin conducting channels. The assumption is confirmed by the transition width increasing with the current passing through the structure (Fig. 1). Indeed, the greater the intrinsic magnetic field generated by the current in a conductor is, the smaller the sample diameter is that allows the superconductivity to appear [6].

The above data suggest that the polymer film confined between massive superconducting electrodes contains superconducting channels with small cross sections, which may exhibit the properties of weak bonds. More evidence is provided by the current–voltage (I–U) characteristic of the Sn–PDMS–Sn sandwich structure presented in Fig. 2a. As seen from this plot, no voltage drop across the structure is observed for $I \le I_c$. This shape of the I–U plot is typical of the Josephson junctions. Therefore, we may expect the Sn–PDMS–Sn structures to feature the Josephson current oscillations in a weak magnetic field.

Indeed, the experiment confirmed this hypothesis. Figure 3 sows the pattern of oscillations in the voltage drop (reflecting variations in the current) across the Sn–PDMS–Sn sandwich structure in a weak transverse magnetic field. The voltage oscillations were measured for two values of the direct current passing through the structure: $I \ge I_c$ (Fig. 3a) and $I > I_c$ (Fig. 3b). As seen, the observed pattern significantly differs from that expected for a system with a single Josephson junction and is more likely to represent a system of N parallel mutually interacting junctions [8]. Figure 3 also shows that the character of voltage oscillations in the magnetic field varies depending on the current passing through the structure. This is apparently related to a nonstationary state of the Josephson junction in the case of $I > I_c$ and $V \neq 0$.

Let us turn back to Fig. 2. As is known, the behavior of $I_c(T)$ in the vicinity of T_c is described by the formula $I_c(T) = \text{const}(1 - T/T_c)^n$, where the exponent n depends on the type of the Josephson junction. In particular, $n = 2$ for an SNS junction (N is a normal metal), in which the superconductivity is due to the proximity effect [9], and $n = 1$ for a junction of the SIS type (I being a tunneling-transparent barrier with a thickness not exceeding 2 nm) or a point contact between two superconductors (S) [10, 11]. The inset in Fig. 2 shows the experimental data on $I_c(T)$ plotted in the double logarithmic coordinates. As seen, our results are well described by the above formula with $n = 1$, which rejects the possibility of a Josephson junction of the

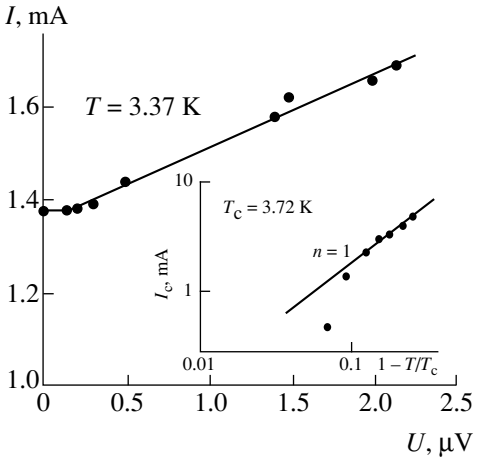

Fig. 2. The current–voltage characteristic of a Sn–PDMS–Sn structure measured in a weak electric field at $T = 3.37$ K. The inset shows the temperature dependence of the critical current (for tin, $T_c = 3.72$ K).

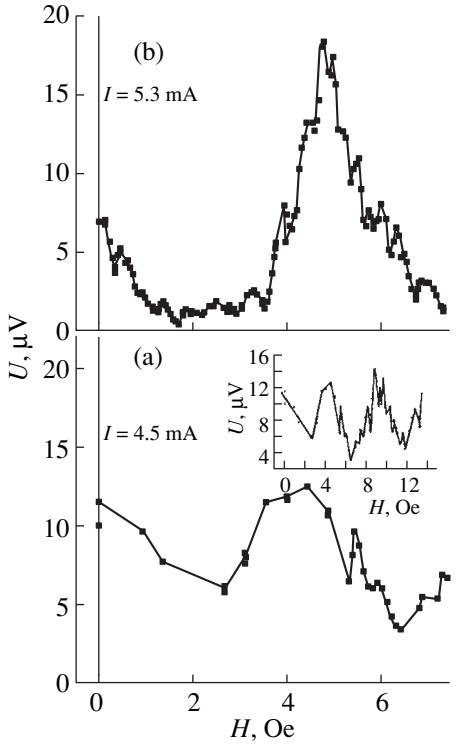

Fig. 3. The plots of voltage drop across the Sn–PDMS–Sn sandwich structure versus the transverse magnetic field strength measured at $T = 2.73$ K for two values of the direct current passing through the structure $I = 4.5$ (a) and 5.3 mA (b). The inset shows the pattern of voltage oscillations in a wider range of magnetic field strengths.

SNS type corresponding to the proximity effect in a polymer channel. As for a junction of the SIS type, it must be noted that, although we did not intend to create a tunneling-transparent dielectric layer, this possibility cannot be excluded since the Sn electrodes may be oxi-

dized in air in the course of the sandwich structure preparation. However, even if this Josephson point contact is formed, we must expect that a superconducting channel in the polymer exists as well. Thus, further investigations are necessary to elucidate the nature of superconductivity of this polymer channel.

Acknowledgments. The work was supported by the Russian Foundation for Basic Research, project no. 00-03-33060.

REFERENCES

1. I. Shlimak and V. Marchenkov, Solid State Commun. **107** (9), 443 (1998).
2. V. A. Zakrevskiĭ, A. N. Ionov, and A. N. Lachinov, Pis'ma Zh. Tekh. Fiz. **24** (13), 89 (1998) [Tech. Phys. Lett. **24**, 539 (1998)].
3. A. N. Ionov, V. A. Zakrevskiĭ, and I. M. Lazebnik, Pis'ma Zh. Tekh. Fiz. **25** (17), 36 (1999) [Tech. Phys. Lett. **25**, 691 (1999)].
4. V. M. Arkhangorodskiĭ, A. N. Ionov, V. M. Tuchkevich, and I. S. Shlimak, Pis'ma Zh. Éksp. Teor. Fiz. **51** (1), 56 (1990) [JETP Lett. **51**, 67 (1990)].
5. P. C. Hohenberg, in *Proceedings of the 11th International Conference on Low-Temperature Physics, Scotland, 1968*; Usp. Fiz. Nauk **102** (2), 239 (1970); W. J. Skocpol, Rep. Prog. Phys. **38**, 1049 (1975).
6. A. C. Rose-Innes and E. H. Rhoderick, in *Introduction to Superconductivity* (Pergamon, Oxford, 1969), Chap. 8.
7. R. Holm, *Electric Contracts: Theory and Application* (Springer-Verlag, New York, 1967).
8. J. Kent Harbaugh and D. Stroud, cond-mat/9809279.
9. P. G. De Gennes, Rev. Mod. Phys. **36**, 225 (1964).
10. V. Ambergaokar and A. Baratoff, Phys. Rev. Lett. **10**, 486 (1963).
11. L. G. Aslamazov and A. I. Larkin, Pis'ma Zh. Éksp. Teor. Fiz. **9** (2), 150 (1969) [JETP Lett. **9**, 87 (1969)].

Translated by P. Pozdeev

Technical Physics Letters, Vol. 26, No. 10, 2000, pp. 913–915. Translated from Pis'ma v Zhurnal Tekhnicheskoĭ Fiziki, Vol. 26, No. 20, 2000, pp. 40–45.

The Properties of InGaAsP/InP Heterolasers with Step-Divergent Waveguides

E. G. Golikova, V. A. Kureshov, A. Yu. Leshko, D. A. Livshits, A. V. Lyutetskiĭ, D. N. Nikolaev, N. A. Pikhtin, Yu. A. Ryaboshtan, S. O. Slipchenko, I. S. Tarasov, and N. V. Fetisova

Ioffe Physicotechnical Institute, Russian Academy of Sciences, St. Petersburg, Russia

Received June 8, 2000

Abstract—InGaAsP/InP laser heterostructures with step-divergent waveguides and two stressed quantum wells were obtained by metalorganic VPE. The lasers emitting at 1.55 μm provide for an intrinsic quantum yield of η_i = 85 %. An optical power of 5.2 W in the continuous operation mode was achieved at a laser diode temperature of 10°C. The internal optical losses in the laser heterostructure studied amount to 3.6 cm^{-1}, which is comparable with the level of losses in similar structures with uniform divergent waveguides. *© 2000 MAIK "Nauka/Interperiodica".*

This work continues our investigation devoted to high-power semiconductor lasers emitting in the 1.3–1.5 μm range. Previously [1–4] we determined the main factors limiting the maximum optical radiation power that can be achieved in mesastrip InGaAsP/InP heterolasers with wide contacts. These factors include large internal optical losses [1, 2], high temperature sensitivity of the differential quantum efficiency [3], and a decrease in the stimulated quantum yield caused by the escape of injected charge carriers into the waveguide [4]. This paper reports on the properties of mesastrip InGaAsP/InP heterolasers with wide contacts based on a separately bounded heterostructure with improved design.

Laser heterostructures based on the InGaAsP/InP solid solution system exhibit certain features in the energy band structure, namely, a special distribution of the bandgap width jump between the conduction and valence bands [5]. Indeed, the conduction band accounts for 1/3 of the total bandgap width jump at the InGaAsP/InP heterojunction [5], which determines a small depth of the potential well for electrons. This leads to the escape of the injected charge carriers and the resulting decrease in the stimulated quantum yield [4]. To reduce this undesired effect, we have refined the design of the separately bounded laser heterostructure. A single waveguide was replaced by three featuring a step-divergent bandgap width variation (Fig. 1). The bandgap width in the wide-bandgap part of the waveguide was increased so as to reduce the charge carrier escape to the waveguide part in contact with emitters. The narrow-bandgap part was accordingly expanded so as to retain the optical confinement factor of the whole waveguide. It should be noted that all the known implementations of step waveguides in laser heterostructures were aimed at reducing the nonradiative recombination at the heterojunctions of a thin waveguide [6–8].

The purpose of this work was to study the properties of InGaAsP/InP laser heterostructures emitting at 1.55 μm with step-divergent-bandgap waveguides obtained by metalorganic-hydride vapor-phase epitaxy.

Figure 1 shows an energy band diagram of a laser heterostructure with the step-divergent waveguide obtained by metalorganic-hydride VPE. The VPE technology and the properties of analogous heterostructures were described in detail previously [1]. A principal distinguishing feature of the structure studied in this work consists in the three-step waveguide design. The thicknesses and bandgap widths of the steps are indicated in Fig. 1. These heterostructures were used in standard laser diode assemblies mounted on copper heat exchangers [1].

Figure 2 shows the plots of the inverse differential quantum efficiency versus the Fabry–Perot resonator length for the lasers with uniform and step-divergent

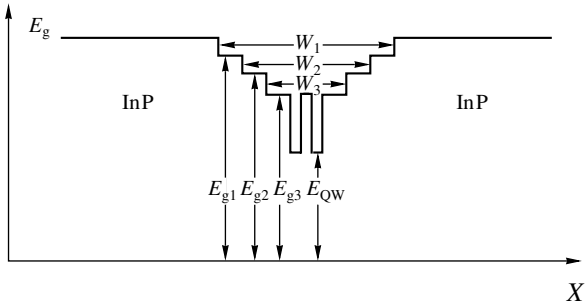

Fig. 1. A schematic band diagram of a laser heterostructure with a step-divergent waveguide: E_{g1} = 1.24 eV; E_{g2} = 1.13 eV; E_{g3} = 1.03 eV; W_1 = 0.85 μm; W_2 = 0.36 μm; W_3 = 0.12 μm.

1063-7850/00/2610-0913$20.00 © 2000 MAIK "Nauka/Interperiodica"

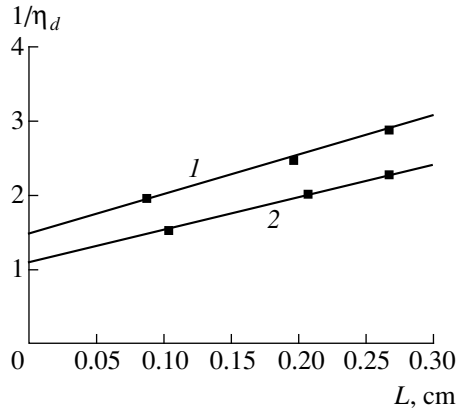

Fig. 2. The plots of the inverse differential quantum efficiency versus the Fabry–Perot resonator length of the laser diodes for the heterostructures with (*1*) uniformly divergent and (*2*) step-divergent waveguides.

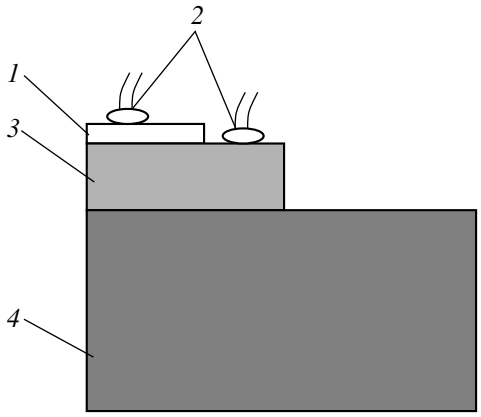

Fig. 3. A diagram of the temperature measurement in a sample heterostructure: (*1*) laser diode; (*2*) thermocouples; (*3*) laser heat exchanger; (*4*) water-cooled heat exchanger.

waveguides. By extrapolating these plots, we may estimate the intrinsic quantum yield of the corresponding laser diodes in the initial region of the output power–current characteristic. In our case, the intrinsic quantum yield was $\eta_i = 67 \pm 3\%$ for the uniformly divergent waveguide and $\eta_i = 85 \pm 3\%$ for the step-divergent waveguide structure. Using the plots of Fig. 2, we may also evaluate the internal optical losses for the structures studied, which amount to $\alpha_i = 4.2$ and 3.6 cm^{-1} for the heterostructures with uniform and step- divergent waveguides, respectively. These values are somewhat inferior to analogous characteristics ($\alpha_i = 1.3$ cm^{-1}) of the best systems reported so far [2]. From these data we infer that the laser heterostructures with a step-divergent waveguide provide for an increase in the stimulated quantum yield without introducing additional optical losses.

A minimum value of the threshold current density (210 A/cm^2) was obtained in laser diodes with 3.3-mm-long Fabry–Perot resonators. Despite a high α_i value, the laser diodes emitting at 1.55 μm provided for a sufficiently high differential quantum efficiency of 44%.

Previously [3], we have demonstrated that the active region of a laser operated in the continuous mode exhibits a 50°C overheating with respect to the water-cooled copper heat exchanger. For this reason, we have used a modified cooling system that ensured constant temperature of the laser heat exchanger (or the crystal) in the entire range of pumping currents employed. Figure 3 shows a diagram of the temperature measurement scheme used with the laser diode tested in the continuous operation mode. Provided the laser diode temperature was maintained on a constant level, the differential quantum efficiency retained the initial value and the maximum attained power was limited only by the thermal breakdown of the laser diode. It should be noted that the breakdown in longer laser diodes (~2.6 mm) was observed at lower current densities than in the shorter ones (~1.1 mm).

Figure 4 shows the output power–current characteristic for the laser diodes of various lengths measured in the continuous operation mode. Cooled with a water flow sufficient to provide a constant temperature of the copper heat exchanger, a laser diode with a resonator length of 2.6 mm yielded a power of 2.5 W at a current of 10 A. Here, the maximum output power was limited by overheating of the active region relative to the heat exchanger. Elimination of this drawback by maintaining a constant temperature of the laser diode allowed the output power of samples with the resonator lengths 2.6 and 1.1 mm to be increased up to 5.2 and 4.2 W,

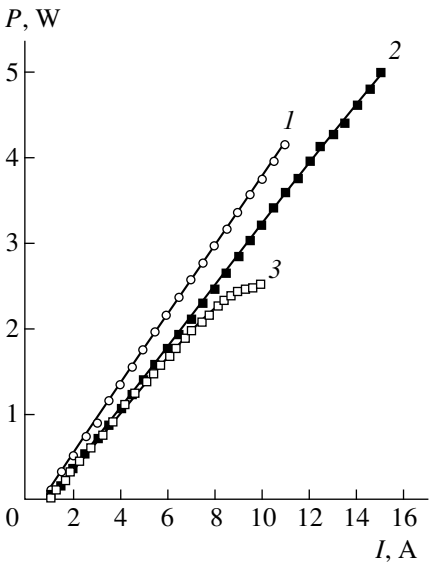

Fig. 4. The output power–pumping current characteristic measured in the continuous operation mode for the laser diodes with the resonator length (*1*) 1.1 and (*2*, *3*) 2.6 mm at (*1*, *2*) a laser diode crystal temperature of 10°C and (*3*) a heat exchanger temperature of 10°C.

respectively. The differential quantum efficiency remained unchanged in the entire range of the pumping currents studied.

Thus, using a laser heterostructure with a step-divergent waveguide allowed us to increase the intrinsic quantum yield up to 85%. The maximum output optical power of a structure operated in the continuous pumping mode was 5.2 W and the internal optical losses did not exceed 3.6 cm^{-1}.

REFERENCES

1. E. G. Golikova, V. A. Gorbylev, N. Yu. Davidyuk, *et al.*, Pis'ma Zh. Tekh. Fiz. **26** (5), 5 (2000) [Tech. Phys. Lett. **26**, 225 (2000)].
2. D. Z. Garbuzov, R. J. Menna, R. U. Martinelli, *et al.*, Electron. Lett. **33**, 1635 (1997).
3. E. G. Golikova, V. A. Kureshov, A. Yu. Leshko, *et al.*, Fiz. Tekh. Poluprovodn. (St. Petersburg) **34**, 881 (2000) [Semiconductors **34**, 853 (2000)].
4. A. Yu. Leshko, A. V. Lyutetskiĭ, N. A. Pikhtin, *et al.*, Fiz. Tekh. Poluprovodn. (St. Petersburg) (in press) [Semiconductors (in press)].
5. S. Adachi, *Physical Properties of III–V Semiconductor Compounds* (Wiley, New York, 1992).
6. A. Kasukawa, I. J. Murgatroyd, Y. Imajo, *et al.*, Jpn. J. Appl. Phys., Part 2 **28**, 661 (1989).
7. A. Kasukawa, T. Namegaya, N. Iwai, *et al.*, Photonics Tech. Lett. **6**, 4 (1994).
8. H. Temkin, D. Coblentz, R. A. Logan, *et al.*, Appl. Phys. Lett. **62**, 2402 (1993).

Translated by P. Pozdeev

Technical Physics Letters, Vol. 26, No. 10, 2000, pp. 916–918. Translated from Pis'ma v Zhurnal Tekhnicheskoĭ Fiziki, Vol. 26, No. 20, 2000, pp. 53–58.

Current Transfer Processes in Thin Lutecium and Terbium Oxide Films on Silicon

Ya. G. Fedorenko, L. A. Otavina, and S. V. Korenyuk

Saratov State University, Saratov, 410071 Russia

e-mail: fedorenkoyg@info.sgu.ru

Received July 11, 2000

Abstract—The results of the experimental study of the current transfer processes in thin Lu_2O_3 and Tb_2O_3 films on silicon substrates are presented. It is shown that, depending on the experimental conditions, the process of either the thermionic-field or the over-barrier emission prevails. Illumination of the structure does not change the effective surface barrier height. The results presented may be important for the practical applications of rare earth oxide-based thin-film systems. *© 2000 MAIK "Nauka/Interperiodica".*

Effects associated with the current transfer in thin films have long been studied and used for various purposes. In particular, a considerable interest has been shown recently in the mechanisms of charge transfer, accumulation, and capture in rare earth oxide films [1–3]. The use of rare earth oxides as dielectrics in metal–insulator–semiconductor (MIS) structures has a number of advantages in comparison with silicon dioxide. These are the low temperatures of their deposition (450–500°C), the possibility of applying high-quality dielectric coatings by various methods, high values of the dielectric constant, and their high radiation resistance [4–6]. However, data on the transverse conductivity of the MIS structures with 100-Å-thick rare earth oxide layers are limited.

In the present article, we consider the results of the experimental study of the current transfer characteristics in rare earth oxide–silicon structures.

Terbium, lutecium, and gadolinium oxide films with a thickness of 100 Å were obtained by the method of thermal deposition of metal films onto silicon substrates in vacuum with a subsequent 15-min oxidation in air at 450°C.

The current–voltage characteristics were measured at a positive bias on the field electrode corresponding to the accumulation mode of the *n*-type silicon surface, in which the voltage and temperature dependences of the current are determined mainly by the conductivity of the oxide layer. The current–voltage characteristics of the samples with various rare earth oxides were qualitatively similar. Consider the main features observed in the study of conductivity. Figure 1 shows typical current–voltage characteristics of the samples with Tb_2O_3 and Lu_2O_3 films plotted in the Poole–Frenkel and Schottky coordinates. The measurements were made at room and liquid-nitrogen temperatures. All the plots show bending points in the region of voltages from 0.1 to 1.2 V indicating a change in the conductivity mechanism. At voltages exceeding 1.0 V, a strictly linear segment is observed. In front of the bending point, the

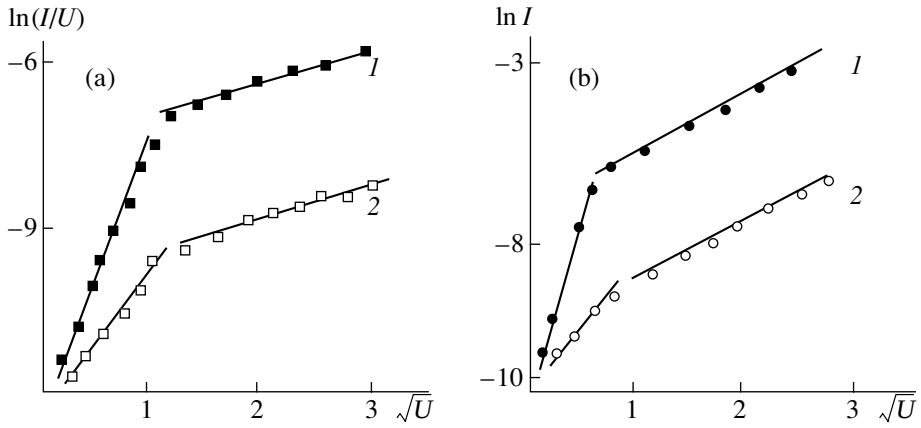

Fig. 1. Current–voltage characteristics of (a) Lu_2O_3 and (b) Tb_2O_3 based MIS structures measured at various temperatures: (*1*) 300; (*2*) 77 K.

1063-7850/00/2610-0916$20.00 © 2000 MAIK "Nauka/Interperiodica"

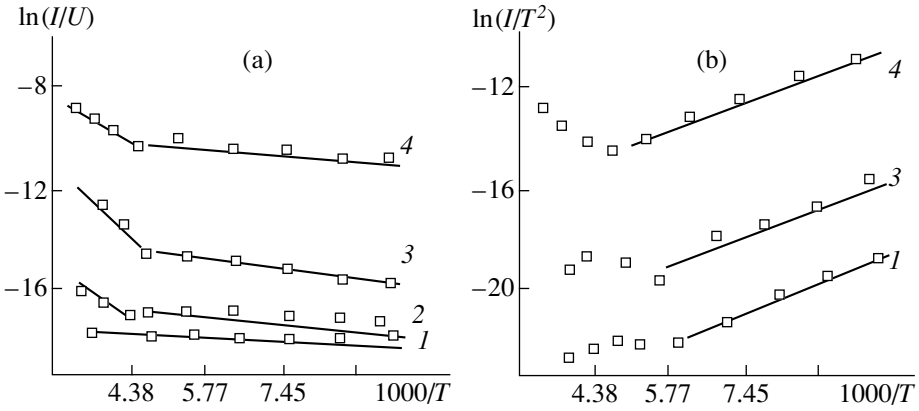

Fig. 2. Temperature dependences of the current in the (a) Lu_2O_3 and (b) Tb_2O_3 based MIS structures measured at various voltages on the field electrode: (*1*) 0.1; (*2*) 0.3; (*3*) 1.0; (*4*) 2.5 V.

plots exhibit a steeper increase in the current depending on the voltage, which seems to be caused by the influence of the current limited by the space charge or the liberation of the carriers from shallow traps in the vicinity of the conduction band bottom. The current–voltage characteristics obtained at 77 K also exhibit bending points in the voltage interval from 1.0 to 1.2 V, which confirms the leading role of the electric field in the process of current transfer.

To reveal the contributions of various conduction mechanisms, we compared the slopes of the experimental current–voltage characteristics in the range of their linearity with the theoretically calculated ones. To evaluate the slopes theoretically, it is necessary to know the dielectric layer thickness and permittivity. We estimated this value from the high-frequency voltage–capacity characteristic, while the ε value was assumed to range within 12–15 for lutecium [4] and taken equal to 30 for terbium (the published data). For the Poole–Frenkel mechanism, the slope β_1 has the value 1.8, whereas for the Schottky mechanism, $\beta_2 = 0.96$. The experimental slopes of the current–voltage characteristics are listed in the table.

The tabulated data for each material were averaged over eight specimens. It is seen that for most of the dielectrics the slope in the case of the Schottky mechanism is closer to the theoretical data than the slope determined for the Poole–Frenkel mechanism.

The plots of the current versus temperature for the Tb_2O_3 and Lu_2O_3 based specimens constructed in the Poole–Frenkel and Schottky coordinates are shown in Fig. 2. For this family of curves, the role of the parameter is played by the voltage applied to the structure. It is seen that the current–voltage characteristic in the Poole–Frenkel coordinates is linear in the high-temperature range (300–150 K). In the voltage range, from 0.8 to 4.0 V, the curves can be divided into two regions—I_1 and I_2. The current I_1 is provided by the Poole–Frenkel mechanism and prevails in intense electric fields and at relatively high temperatures. The current I_2 seems to be caused by the tunneling emission of electrons from the traps to the conduction band prevailing at low temperatures and intense electric fields. At the voltages from 0.1 to 0.6–0.8 V, the temperature dependence is linear in the entire temperature range, and the film conductivity only slightly depends on the temperature. As the voltage increases from 0.8 to 2.5 V, the slope of the temperature dependence in the range from 300 to 150 K tends to decrease, which is characteristic of the Poole–Frenkel mechanism.

As the temperature decreases within a wide range from 150 to 77 K, a weak temperature dependence of the current is observed in intense electric fields (U = 1–4 V). As is seen from Fig. 2b, the temperature dependence of the current for the Tb_2O_3 based specimens measured at low temperatures is linear in the Schottky coordinates; the current somewhat increases with a decrease in the temperature, which is characteristic of the over-barrier emission and tunneling.

We have analyzed the slope of the temperature dependence at 300–150 K in the α versus $\sqrt{U}$ coordinates to determine the activation energy of the conduc-

Slopes of the current–voltage characteristics calculated under the assumption of the Poole–Frenkel (β_1) and the Schottky (β_2) mechanisms and the conductivity activation energy E_t

Dielectric material	β_1	β_2	E_t, eV
Y_2O_3	1.45	0.71	0.03
Dy_2O_3	1.24	0.96	0.026
Tb_2O_3	1.58	0.99	0.04
Gd_2O_3	1.6	1.1	–
Lu_2O_3	1.7	0.9	0.032

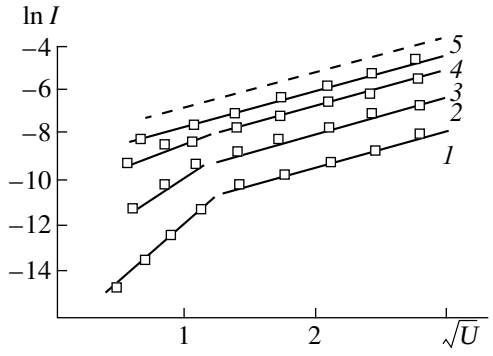

Fig. 3. Current–voltage characteristics of a Tb_2O_3 based MIS structure measured at various illumination levels: (*1*) 10^3; (*2*) 3×10^3; (*3*) 4×10^3; (*4*) 6×10^3; (*5*) 7×10^3 lx.

tion process in various dielectrics: E_t = 0.026–0.04 eV. The corresponding data are given in the table and are close to the ionization energies of shallow donor traps in the corresponding rare earth oxide films (E_t = 0.036 eV [5]). This is more evidence in favor of the Poole–Frenkel mechanism being operative in thin lutecium and terbium oxide films in the temperature and field strength ranges studied.

The effect of illumination on the sample structures and the corresponding current–voltage characteristics also confirm the existence of various conductivity mechanisms in the films studied. The current–voltage characteristics of the Tb_2O_3 based MIS structures measured on the illuminated specimens are shown in Fig. 3. In the region of voltages from 1.4 to 2.5 V, the characteristics obtained at an illumination of up to 6000 lx exhibit bending points. Behind these points, the plots constructed in the Schottky coordinates are linear. The constant slope observed irrespective of the illumination and voltage applied indicates that the illumination almost does not affect the metal–dielectric barrier height. It is known [6] that the efficiency of photoconversion in MIS structures is significantly dependent on the magnitude and the sign of the initial surface energy band bending, that is, on the barrier for electrons on the semiconductor surface. In terbium oxide–based MIS structures, the sign of the built-in charge is negative, the surface of the *n*-Si substrate is depleted in the major carriers, and, therefore, the photogenerated charge carriers appearing in the vicinity of the barrier considerably modulate the conductivity of the depleted layer. In the region where the injection mechanism is operative, the photogeneration does not significantly increase the current, because of a high dark concentration of the charge carriers. As the illumination intensity increases, the point on the ln*I* versus $\sqrt{U}$ plot at which the conductivity mechanism changes shifts toward higher voltages (Fig. 3). For the illumination intensities exceeding 6000 lx, only the injection mechanism of the current transfer is possible (dashed line in Fig. 3). With increasing illumination, most of the electron–hole pairs generated by the light in the MIS structure experience recombination in the semiconductor bulk and, hence, only a small number of such pairs can contribute to the photocurrent.

Thus, the results obtained indicate a complicated nature of the charge transfer processes occurring in terbium and lutecium oxide films. The study of the current transfer characteristics depending on the voltage, temperature, and illumination shows that conductivity in rare earth oxide films is determined by several mechanisms, the manifestation of which depends on the experimental conditions. In the range of field strengths $E > 10^6$ V/cm and temperatures 300–150 K, the key part is played by the Poole–Frenkel mechanism. At lower temperatures, the effects of the metal–dielectric and dielectric–semiconductor barriers become substantial, and the dielectric layer conductivity is determined by tunneling and the Schottky over-barrier emission.

REFERENCES

1. C. H. Ling, J. W. Bhaskaran, W. K. Choi, and L. K. Ah, J. Appl. Phys. **77** (12), 6350 (1995).
2. A. I. Petrov and V. A. Rozhkov, in *Physics and Chemistry of Rare-Earth Semiconductors* (Nauka, Novosibirsk, 1990).
3. S. C. Choi, M. H. Cho, S. W. Whangbo, and C. N. Whang, Appl. Phys. Lett. **71** (7), 903 (1997).
4. A. M. Sverdlova, Élektron. Tekh., Ser. 2 **5**, 96 (1972).
5. B. A. Andreev, N. A. Sobolev, D. I. Kuritsin, *et al.*, Fiz. Tekh. Poluprovodn. (St. Petersburg) **33** (4), 419 (1999) [Semiconductors **33**, 407 (1999)].
6. I. A. Agafonov, A. F. Plotnikov, and V. N. Seleznev, Tr. Fiz. Inst. Akad. Nauk SSSR **184**, 24 (1987).

Translated by L. Man

Technical Physics Letters, Vol. 26, No. 10, 2000, pp. 919–922. Translated from Pis'ma v Zhurnal Tekhnicheskoĭ Fiziki, Vol. 26, No. 20, 2000, pp. 59–66.

Argon–Oxygen Ion-Plasma Treatment Modifies the Surface Composition and Photoluminescence Spectrum of Porous Silicon

B. M. Kostishko*, A. V. Drozdov*, P. V. Shibaev, and A. E. Kostishko***

** Ul'yanovsk State University, Ul'yanovsk, Russia*

*** Copenhagen University, Fruebjergvej 3, DK-2100, Copenhagen, Denmark*

Received May 22, 2000

Abstract—We have studied changes in the surface composition and photoluminescence spectrum of porous silicon (por-Si) during the ion-plasma etching of samples in an argon–oxygen gas mixture. This treatment leads to the passivation of the surface of quantum filaments by residual fluorine and the formation of silicon oxide. The source of fluorine atoms are HF molecules retained in the volume of pores upon the por-Si structure formation by chemical etching. Increase in the fluorine concentration is accompanied by the growth in intensity of the blue-green band and broadening of the red band in the photoluminescence spectrum of por-Si. *© 2000 MAIK "Nauka/Interperiodica".*

The role of molecules passivating the surface of quantum filaments and filling the volume of pores in light-emitting devices based on porous silicon (por-Si) have been extensively studied for more that one decade [1]. The initial data, concerning thermostimulated changes in the composition of hydrogen-containing groups (mono- and dihydrides) in por-Si heat-treated in vacuum, and an evident relationship between the SiH_2 degradation and por-Si photoluminescence quenching [2, 3] served as the main arguments against the Canham quantum-confinement model [4]. Eventually, it was established that both hydrogen- [5] and oxygen-containing compounds [6] may lead to the activation of photoluminescence in por-Si. All these results contributed to the formulation of the so-called "hydrogen" and "interfacial" models [1, 7].

However, none of the models existing at present can account for the entire combination of complicated processes occurring in por-Si and describe the mechanisms responsible for its light-emitting properties and degradation behavior. In particular, it was demonstrated [8] that filling the pores in por-Si with a dielectric medium or polar molecules may lead to a decrease in the photoluminescence intensity as a result of changes in the binding energy or in the concentration of excitons. A significant contribution of excitons to the photoluminescence of por-Si was theoretically predicted as long ago as in 1992 [9]. However, dependence of the properties of por-Si on the presence of fluorine-containing compounds in the material surface layer was insufficiently studied, although, it was clearly demonstrated that the photoluminescence in por-Si is excited predominantly in an oxide phase enriched, in particular, by F^- and SiF^- ions [10].

In connection with the above data, this work was devoted to the study of changes in the surface composition of por-Si in the course of the ion-plasma etching in an argon–oxygen mixture. The sample surface composition was determined by Auger electron spectroscopy (AES). Also reported are the data on changes in the photoluminescence spectra of por-Si samples upon the ion-plasma-induced oxidation and fluorination.

The experiments were performed with por-Si samples prepared by a standard technology involving a 10-min electrochemical etching in an electrolyte comprising a mixture of HF and C_2H_5OH. The porosity and thickness of the porous layer were 45% and 6 μm, respectively.

The ion-plasma etching of por-Si samples was effected in a commercial vacuum system of the VUP-5 type. The pressures of argon and residual oxygen in the vacuum chamber during etching were maintained equal to 2.6×10^{-2} Pa; the plasma discharge voltage and current were 2.5 kV and 25 mA, respectively; an additional sample heating during this treatment did not exceed 5 K. In the course of the ion-plasma etching, a part of the sample surface was shielded with a mask (representing the same single-crystal silicon wafer as that used for the por-Si preparation). The chemical composition of samples was studied using an 09-IOS-10-005 AES spectrometer equipped with an energy analyzer providing a resolution of $\Delta E/E = 0.4\%$. The AES measurements were performed at a residual gas pressure of $P = 10^{-7}$ Pa in the analytical chamber, a primary electron beam energy of 3 keV, and an electron beam current of $i = 0.5$ μA.

As seen from the AES data presented in Fig. 1, the por-Si surface composition exhibits significant changes

1063-7850/00/2610-0919$20.00

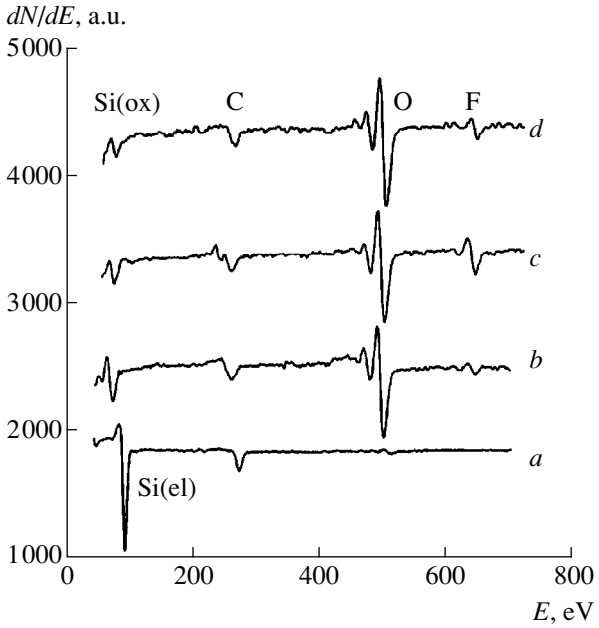

Fig. 1. Auger electron spectra of a silicon sample with a 6-μm-thick porous layer in the (*a*) as-prepared (initial) state and upon the ion-plasma etching for (*b*) 1 and (*c*) 13 min. Spectrum (*d*) represents the surface of 32-μm–thick porous layer upon a 20-min ion-plasma etching. Si(el) and Si(ox) are the *LVV* Auger lines of elemental and oxidized silicon.

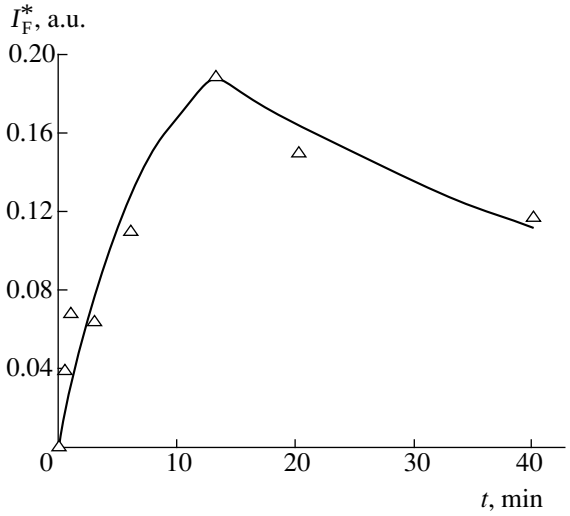

Fig. 2. Variation of the normalized intensity I_F^* of the Auger electron peak of fluorine with the duration *t* of the ion-plasma treatment of the por-Si sample surface. Triangles represent the experimental points, solid curve shows the approximation according to formulas (5).

in the course of the ion-plasma etching. The AES spectrum of the initial freshly-prepared por-Si (Fig. 1, curve *a*) shows the presence of elemental silicon Si(el) (manifested by the Si *LVV* Auger line at 91 eV) and surface contaminations (carbon and oxygen). The spectrum displays no peaks due to fluorine atoms, which indicates that fluorine may be contained on the por-Si surface only at a level below the sensitivity of the AES spectrometer employed (0.05 at. %). However, the AES spectrum measured immediately upon the first ion-plasma treatment cycle exhibits a shift of the silicon peak to 75 eV (Fig.1, curve *b*) evidencing effective oxidation of the sample surface and the formation of a SiO_x layer. It is important to note that the oxide is present in both the plasma-etched and masked areas. However, only the plasma-etched areas exhibit the fluorine peak with the intensity significantly depending on the treatment time (Fig. 2). The fluorine peak intensity was normalized to the total intensity of all peaks in the spectrum:

$$I_F^* = I_F / \sum_{i=1}^{n} I_i. \quad (1)$$

The AES line intensities were measured as peak-to-peak heights.

All changes observed during the experiment can be explained by the following sequence of processes and reactions in por-Si. In the first stage, the residual molecules of hydrofluoric acid (HF) retained upon the electrochemical etching in the region of pore vertices [11] are oxidized by oxygen radicals O* present in the plasma:

$$2HF + O^* = H_2O + F_2. \quad (2)$$

The oxygen radicals are also responsible for the rapid oxidation of the surface of quantum filaments. Indirect evidence of the fact that this oxidation is produced by electrically neutral species is provided by the frontal oxidation of a por-Si sample surface protected by the mask.

The oxidation of residual HF is accompanied by the formation of unsaturated (dangling) silicon bonds as a result of the por-Si surface sputtering with Ar ions. It is the presence of dangling bonds that allows fluorine radicals to passivate the sample surface. This is confirmed by the absence of fluorine peaks in the AES spectra of the sample areas masked in the course of the ion-plasma etching (where no ion bombardment and dangling bond formation took place).

The role of oxygen radicals in the formation of gaseous fluorine was checked by studying por-Si samples with a porous layer thickness of 32 μm. Apparently, the ion etching of thick porous layers did not lead to the ion-stimulated decomposition of the HF molecules retained in deep pores. However, even these samples show evidence of the ion-plasma-induced fluorination of the surface of quantum filaments (Fig. 1, curve *d*).

The amount of fluorine retained in the porous layer is limited, being dependent on the conditions of por-Si preparation and the sample prehistory. For this reason, the kinetics of variation of the fluorine concentration

N_{FS} on the por-Si surface can be described by the following equation:

$$dN_{FS}/dt = -\sigma j_{Ar} N_{FS} + k_C N_{DB} N_{FG}, \quad (3)$$

where j_{Ar} is the argon ion flux, σ is the cross section of the argon ion interaction with fluorine atoms on the sample surface, N_{DB} is the concentration of dangling bonds, N_{FG} is the fluorine concentration in the gas phase, and k_C is the coefficient characterizing the rate of fluorine passivation of the silicon dangling bonds.

Equation (3) cannot be solved exactly, because no reliable data are available on the process parameters entering into this expression. However, we may assume for the first approximation that a fluorine concentration in the gas phase varies in a nonmonotonic manner. Indeed, N_{FG} will grow during a certain period of time t_0 until the source of fluorine atoms in the bulk of pores is exhausted; this is followed by a decrease in N_{FG} at $t > t_0$. In order to verify the applicability of the above model to finding the analytical solution to Eq. (3), the second term can be selected in the following form:

$$k_C N_{DB} N_{FG} = \begin{cases} B(1 - \exp(-t/\tau_1)), & t \le t_0 \\ \exp[-(t - t_0)/\tau_2] B(1 - \exp(-t_0/\tau_1)), & t \ge t_0 \end{cases}, \quad (4)$$

where τ_1 and τ_2 are the characteristic times for the buildup and decay of fluorine concentration in the plasma, respectively. Taking into account expressions (4), a solution to Eq. (3) can be obtained in the following general form:

$$N_{FS} = \begin{cases} A_1 + A_2 \exp(-t/\tau_1) - A_3 \exp(-\sigma j_{Ar} t), & t \le t_0 \\ B_1 \exp[-(t - t_0)/\tau_2] + B_2 \exp(-\sigma j_{Ar} t), & t \ge t_0. \end{cases} \quad (5)$$

The preexponential factors in Eq. (5) depend on the parameters of Eqs. (3) and (4), as well as on the time t_0. To illustrate the applicability of the proposed model, a solid curve in Fig. 2 shows the approximation of the experimental data according to Eqs. (5) with the characteristic times $\tau_1 = 6.8$ min and $\tau_2 = 52$ min. As seen, the model provides a relatively good coincidence of calculated and experimental values.

Figure 3 shows the photoluminescence spectra of por-Si measured in the course of the ion-plasma treatment. An analysis of these spectra led us to the following conclusions concerning the role of fluorine in the light-emitting properties of porous silicon. An increase in the fluorine concentration in the plasma and fluorination of the surface of quantum filaments ($t < t_0$) is accompanied by the growth in intensity of the blue-green band (λ_{BG} = 480–490 nm) and by the quenching and broadening of the red band (λ_R = 670–680 nm) in the photoluminescence spectrum (Fig. 3, curves *1*–*3*).

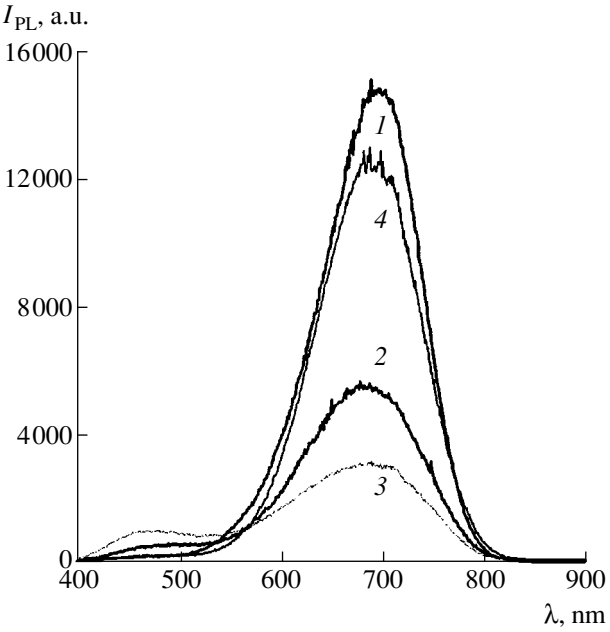

Fig. 3. Photoluminescence spectra of a por-Si sample in the (*1*) as-prepared (initial) state and upon the ion-plasma etching for (*2*) 3, (*3*) 6, and (*4*) 20 min.

Indeed, the ratio of intensities of the blue-green and red spectral lines was $I_{BG}/I_R = 0.04$ upon a 1-min ion-plasma etching in the argon-oxygen mixture and increased to $I_{BG}/I_R = 0.3$ upon a 6-min treatment. During the same time, the dispersion (width) of the red line increased by a factor of 1.5. Exhaustion of the fluorine source and a decrease in the fluorine content on the por-Si sample surface lead to the opposite changes in the photoluminescence spectrum (Fig. 3, curve *4*). Simultaneously, the red line in the spectrum acquires a Gaussian shape.

Thus, we have demonstrated that bombardment of a freshly prepared porous silicon sample by argon ions in the plasma containing oxygen radicals is accompanied by effective fluorination of the sample surface. The main conditions facilitating this process are the formation of free fluorine atoms as a result of oxidation of the residual HF molecules present in the pores and the appearance of dangling silicon bonds on the por-Si surface, which is caused by its sputtering with Ar^+ ions.

Fluorination of the surface of por-Si leads top the formation of radiative recombination centers with an energy of $E \approx 2.58$ eV. Upon the subsequent defluorination of the oxidized surface of quantum filaments in the course of the ion-plasma etching, the radiative recombination of electron–hole pairs occurs predominantly in a thin subsurface layer at the silicon–silicon oxide interface. In this case, the position and shape of bands in the photoluminescence spectrum are determined by characteristics of a nonstoichiometric oxide in this layer (in particular by the corresponding bandgap width [7])

rather than by the size and structure of the quantum-confined regions.

Acknowledgments. This work was supported by the Russian Foundation for Basic Research (project no. 99-02-17903), by a federal "Russian Universities–Fundamental Research" Program, and by a grant from the Ministry of Education of the Russian Federation.

REFERENCES

1. A. G. Cullis, L. T. Canham, and P. D. J. Calcott, J. Appl. Phys. **82** (3), 909 (1997).
2. C. Tsai, K.-H. Li, J. Sarathy, *et al.*, Appl. Phys. Lett. **59**, 2814 (1991).
3. C. Tsai, K.-H. Li, D. S. Kinosky, *et al.*, Appl. Phys. Lett. **60**, 1700 (1992).
4. L. T. Canham, Appl. Phys. Lett. **57**, 1046 (1990).
5. B. M. Kostishko, A. M. Orlov, S. N. Mikov, *et al.*, Izv. Ross. Akad. Nauk., Neorg. Mater. **31** (4), 444 (1995).
6. A. Nakajima, T. Itakura, S. Watanabe, *et al.*, Appl. Phys. Lett. **61** (1), 46 (1992).
7. K. Yoshishiko, O. Tetsuo, Sh. Kenji, *et al.*, Phys. Rev. B **48** (7), 4883 (1993).
8. P. K. Kashkarov, E. A. Konstantinova, and V. Yu. Timoshenko, Fiz. Tekh. Poluprovodn. (St. Petersburg) **30** (8), 1479 (1996) [Semiconductors **30**, 778 (1996)].
9. G. D. Sanders and Yia-Chung Chang, Phys. Rev. B **45** (16), 9202 (1992).
10. N. E. Korsunskaya, T. V. Torchinskaya, B. R. Dzhumaev, *et al.*, Fiz. Tekh. Poluprovodn. (St. Petersburg) **30** (8), 1507 (1996) [Semiconductors **30**, 792 (1996)].
11. M. E. Kompan and I. Yu. Shabanov, Fiz. Tekh. Poluprovodn. (St. Petersburg) **2** (10), 1250 (1995) [Semiconductors **29**, 971 (1995)].

Translated by P. Pozdeev

Technical Physics Letters, Vol. 26, No. 10, 2000, pp. 923–925. Translated from Pis'ma v Zhurnal Tekhnicheskoĭ Fiziki, Vol. 26, No. 20, 2000, pp. 67–74.

Dispersion Characteristics of Magnetostatic Waves Propagating at a Ferrite/Perovskite Interface

S. F. Karmanenko*, A. A. Semenov*, A. A. Melkov*, N. N. Isakov*, and Ya. Vas'kevich**

** University of Electrical Engineering, St. Petersburg, Russia*

*** Białystok College of Technology, Białystok, Poland*

Received May 29, 2000

Abstract—The propagation of magnetostatic waves at the interface between an yttrium–iron-garnet (YIG) film and a layer of perovskite compound $LaAlO_3$, $SrTiO_3$, or $YBa_2Cu_3O_{7-x}$ (YBCO) was experimentally studied. The microwave dispersion characteristics were measured at room temperature and at 77 K. An effective method for controlling the propagation speed and the phaseshift of magnetostatic waves in the YIG/YBCO structures is suggested. Specifically, the phaseshift at 3 GHz is changed by more than 1.5π by reducing the critical current density from 1 to 0.7×10^6 A/cm^2. © *2000 MAIK "Nauka/Interperiodica".*

Magnetostatic waves, also known as spin waves, are slow electromagnetic waves of a microwave frequency that are excited in low-loss ferromagnetic materials. In most cases, epitaxial films of an yttrium–iron garnet (YIG) with the composition $Y_3Fe_5O_{12}$ serve as the propagation medium.

Spin waves are excited in the presence of a magnetostatic field which magnetizes the ferromagnetic film to saturation, that is, makes elementary magnetic moments at the crystal lattice sites form a tightly bound chain. A local disturbance caused, for example, by a current through a conductor generates a spin wave propagating in the film. The reverse (wave-to-current) conversion occurs in a second conductor situated at a certain distance from the first one. This mechanism underlies the operation of many spin-wave devices. In the simplest case, the input transducer is a microstripline section. The magnitude of the wave vector **k** can be varied within a wide range, being determined by the input transducer geometry and the spin-wave structure configuration.

It is a novel concept in electronics to use devices in which the spin waves propagate along the interface between a YIG film and a layer possessing some other remarkable properties, the two layers being parts of a multilayer structure [1]. Encouraging possibilities were outlined for using the YIG/superconductor structures in microwave devices such as circulators, switches, and phaseshifters with wide dynamic range [2]. Today, the most frequently employed superconductor is the perovskite compound $YBa_2Cu_3O_{7-x}$ (YBCO). It was demonstrated that microwave bandpass filters built around a YIG/YBCO structure exhibit lower losses as compared to those employing copper microstrip lines [3]. In recent years, the growth of superconducting films on YIG-based heteroepitaxial layers [4, 5] has been extensively investigated. However, it may well be practical to employ structures comprising the YIG film in close contact with a superconducting film. An analysis of the spin-wave propagation in a multilayer structure with a ferroelectric (FE) showed that metal/FE/YIG/FE/metal structures could probably offer very good performance in the microwave band [1]. Thus, multilayer structures with a YIG/perovskite interface are interesting objects of research in microwave electronics.

This paper explores the possibilities for controlling spin-wave propagation at a YIG/perovskite interface, the perovskite being the superconductor YBCO, the ferroelectric $Ba_xSr_{1-x}TiO_3$ (BSTO), or the linear dielectric $LaAlO_3$ (LAO).

In our experiment, the waveguides for spin waves were YIG epitaxial films with a thickness of several micrometers, produced by liquid-phase epitaxy [6]. YBCO films were grown on LAO substrates [8] by the magnetron sputtering of a stoichiometric target [7].

Figure 1 shows a schematic diagram of an experimental guiding structure comprising the input and output microwave transducers, a perovskite film screen, and a YIG film waveguide. The transducers and the perovskite film lie in the same plane, and the YIG film is pressed against them from above. The distance L between the transducers is 7.25 mm. The guiding structure is fixed in an assembly containing miniature electromagnets, microwave coaxial connectors, and a metallic base, all of the parts being made of a nonmagnetic material. The assembly with the YIG film is placed into a uniform magnetostatic field directed parallel to the film and perpendicular to the direction of the spin wave propagation. The structure was cooled down to a cryogenic temperature by immersing the assembly into liquid nitrogen.

The dispersion characteristics of the sample structures were obtained with a measuring system built

1063-7850/00/2610-0923$20.00

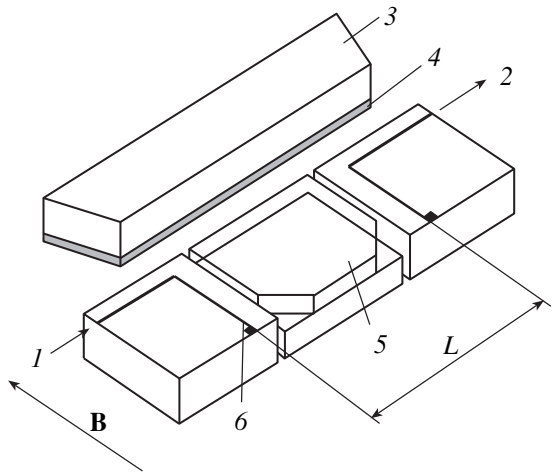

Fig. 1. Schematic diagram of a YIG/perovskite guiding structure: (*1*) input transducer; (*2*) output transducer; (*3*) metal base; (*4*) YIG film; (*5*) perovskite film; (*6*) microstrip line.

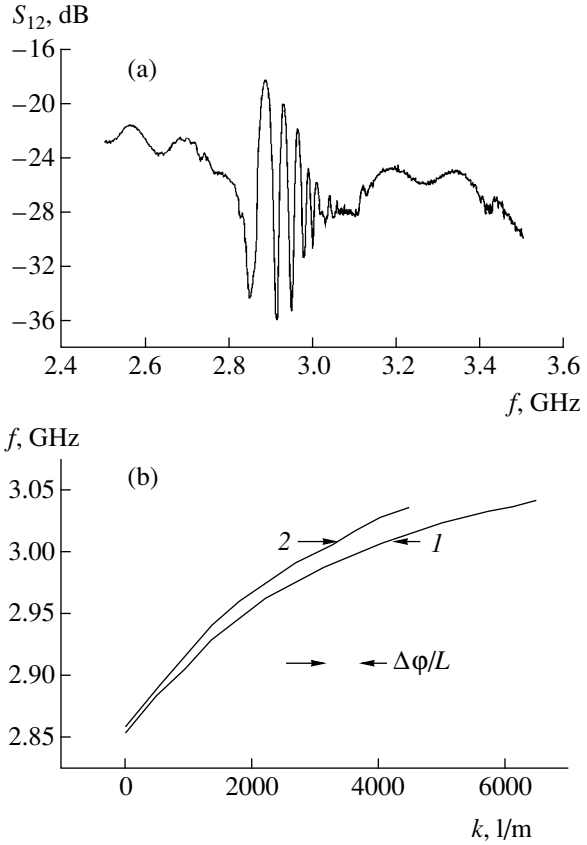

Fig. 2. Frequency characteristics of the YIG/YBCO structures representing (a) an interference pattern for sample 1 at 77 K and (b) dispersion characteristics for samples 1 and 2. Curve *1* in Fig. 2b is obtained from the pattern in Fig. 2a.

around an R2-54 panoramic meter of the voltage standing-wave ratio. The meter separately extracts signals proportional to the input and the output (transmitted) power. The two signals are added together in a directional coupler. The characteristics are stored and processed in a computer connected to the meter.

The YIG films had a thickness of about 8 μm and a saturation magnetization of 1400 Oe at 77 K, the bias field being about 566 Oe. The YBCO films had a thickness of about 0.6 μm.

The dispersion characteristics were reconstructed from the experimentally measured interference patterns. Figure 2a presents an interference pattern obtained at 77 K with a YBCO film (sample 1). The wavenumber was determined from the positions of peaks and valleys according to the formula $k = i\pi/L$, where i is the peak number. Figure 2b displays the dispersion characteristics corresponding to the pattern depicted in Fig. 2a in comparison with a pattern for another YBCO film (sample 2).

Having a rectangular shape of dimensions 6×5 mm, the two YBCO films were grown in the same, film 2 being subjected to additional short-time quenching in air. Film 1 possessed a critical temperature T_c of 90 K and a critical current density J_c of about 1×10^{10} A/m^2 (at 77 K). Film 2 was characterized by $T_c \approx 90$ K and $J_c \approx 7 \times 10^9$ A/m^2 (at 77 K).

The plots of the spin-wave group velocity V_{gr} versus wavenumber were obtained by graphical differentiation of the dispersion characteristics, since $V_{gr} = \dfrac{\partial\omega}{\partial k}$. Figure 3a depicts the spin-wave group velocity as a function of the frequency for the YIG/YBCO interfaces. Figure 3b shows analogous diagrams for the YIG/dielectric structures.

The dispersion characteristics (Fig. 2b) and the frequency dependences of the group velocity (Fig. 3) show that it is possible to effectively control the propagation speed and the phaseshift $\Delta\varphi$ of a microwave signal in the YIG/perovskite structures. For example, the phaseshift $[\Delta\varphi = (k_1 - k_2) \times L]$ in the YIG/YBCO structures is $\Delta\varphi = 1.75\pi$, which is a good result for controlled microwave devices. The properties of a superconducting film can be modified immediately during measurements by applying an electric bias or by irradiating the film. This offers additional means of controlling the spin-wave propagation in ferrite structures.

Electrical control can be implemented in YIG/ferroelectric structures, where the group velocity and the phaseshift can be changed by adjusting the electric bias and varying the permittivity of the ferroelectric layer [9]. A comparison of the group-velocity curves in Figs. 3a and 3b shows that the YIG/ferroelectric structure provides a steeper frequency dependence and fairly large phaseshifts.

In conclusion, note that the spin-wave devices using electrical or optical control seem to be far more practi-

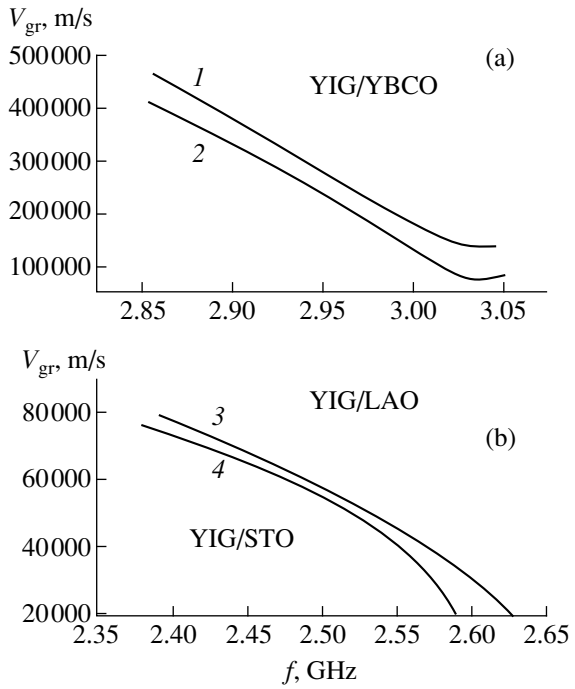

Fig. 3. Controlling the dispersion characteristics by modifying the properties of the perovskite film: (a) YIG/YBCO structures (at 77 K) representing (*1*) sample 1 ($j_c = 1 \times 10^{10}$ A/m^2, $T_c = 90$ K) and (*2*) sample 2 ($j_c = 7 \times 10^9$ A/m^2, $T_c = 90$ K); (b) YIG/dielectric structures (at 300 K), where the dielectric is (*3*) LAO ($\varepsilon = 22$) or (*4*) STO ($\varepsilon = 450$).

cal than those with a magnetic one, since the former would offer much higher operation speeds.

Acknowledgments. We are grateful to Prof. B.A. Kalinikos for his support and participation in related studies.

This study was conducted as part of the Interface Project (no. 98055) of the "Superconductivity" State Program and as part of a research project implemented at the St. Petersburg University of Electrical Engineering under the terms of the program "High-School Research Projects on Manufacturing Technologies: Electronics" supported by the Ministry of Education of the Russian Federation.

REFERENCES

1. V. E. Demidov and B. A. Kalinikos, Pis'ma Zh. Tekh. Fiz. **25** (21), 86 (1999) [Tech. Phys. Lett. **25**, 880 (1999)].
2. G. F. Dionne, D. E. Oates, D. H. Temme, and J. A. Weiss, IEEE Trans. Microwave Theory Tech. **44** (7), 1361 (1996).
3. S. F. Karmanenko and A. A. Semenov, Pis'ma Zh. Tekh. Fiz. **26** (3), 12 (2000) [Tech. Phys. Lett. **26**, 96 (2000)].
4. Q. X. Jia, A. T. Findikoglu, P. Arendt, *et al.*, Appl. Phys. Lett. **72** (14), 1763 (1998).
5. S. V. Yakovlev, L. A. Kalyuzhnaya, G. A. Nikolaĭchuk, *et al.*, Pis'ma Zh. Tekh. Fiz. **23** (12), 69 (1997) [Tech. Phys. Lett. **23**, 484 (1997)].
6. Yu. M. Yakovlev and S. Sh. Gendelev, in *Single Crystals of Ferrites in Radio Electronics* (Sov. Radio, Moscow, 1975).
7. S. F. Karmanenko, A. A. Semenov, A. A. Svishchev, *et al.*, Pis'ma Zh. Tekh. Fiz. **25** (15), 79 (1999) [Tech. Phys. Lett. **25**, 626 (1999)].
8. A. N. Morozov, O. K. Morozova, N. M. Ponomarev, and S. N. Knyazev, Sverkhprovodimost': Fiz., Khim., Tekh. **5** (2), 388 (1992).
9. O. G. Vendik, L. T. Ter-Martirosyan, S. F. Karmanenko, *et al.*, Ferroelectrics **144** (1–4), 33 (1993).

Translated by A. Sharshakov

Technical Physics Letters, Vol. 26, No. 10, 2000, pp. 926–928. Translated from Pis'ma v Zhurnal Tekhnicheskoĭ Fiziki, Vol. 26, No. 20, 2000, pp. 75–81.

A Comparative Study of the Atomic Hydrogen Penetration into Thin Vanadium Films and Silicon Oxide–Gallium Arsenide Structures

V. G. Bozhkov*, V. A. Kagadeĭ*, D. I. Proskurovskiĭ, and L. M. Romas'****

** Institute of Semiconductor Devices, State Research and Production Enterprise, Tomsk, Russia*

*** Institute of High-Current Electronics, Siberian Division, Russian Academy of Sciences, Tomsk, Russia*

e-mail: vak@lve.hcei.tsc.ru

Received May 19, 2000

Abstract—It was established that the laws of atomic hydrogen penetration from an arc reflection discharge gap with a hollow cathode and self-heating element into GaAs samples coated with a thin SiO_2 film differ significantly from the laws observed for the hydrogenation of thin vanadium films. The amount of hydrogen penetrating into the SiO_2/GaAs system decreases with increasing atomic hydrogen concentration in the gas phase. This is apparently related to a decrease in the probability of hydrogen atoms penetrating into the substrate, which is suggested to drop significantly with decreasing atomic energy and/or increasing hydrogen content in a thin subsurface layer. © *2000 MAIK "Nauka/Interperiodica".*

As is known, the hydrogen penetration under thermodynamical equilibrium conditions from a gas phase through a "real" (not atomically clean) surface into Ta, V, Nb, and Pd samples is a process of the activation type [1–3]. The probability of a hydrogen atom penetrating into the metal lattice is smaller than unity. A limiting stage in this process is either a dissociative adsorption of hydrogen molecules on the solid surface or the transition of atoms from the adsorbed state into the metal lattice. Under nonequilibrium conditions, when hydrogen may occur in the gas phase in the atomic form, hydrogen penetrates into transition metals in an activationless manner, whereby the probability of a hydrogen atom reaching the surface to enter the lattice is close to unity [3]. This is explained by the fact that hydrogen atoms, in contrast to molecules, possess an excess potential (chemical) energy (~2.25 eV) amounting to half of the dissociation energy of a hydrogen molecule.

Under thermodynamical equilibrium conditions, hydrogen hardly penetrates into semiconductor materials. For this reason, semiconductors are usually hydrogenated either in a hydrogen plasma or in the atmosphere of atomic hydrogen. However, the laws of hydrogen penetration into semiconductor materials under these conditions are still insufficiently studied. In this work, we have performed, for the first time, a comparative study of the laws of atomic hydrogen penetration from a low-pressure discharge into thin vanadium films and GaAs samples coated with thin SiO_2 films.

Vanadium films with a thickness of 50 nm were deposited onto 5×60 mm sitall (glass ceramic) substrates by thermal evaporation in vacuum in a setup described in [4]. Hydrogen was then admitted to the system (i.e., the samples did not contact with atmosphere) and the films were treated in a flow of atomic hydrogen. The semiconductor samples were prepared using n^+-GaAs(100) substrates carrying a 500-nm-thick epitaxial film of the *n*-type with a charge carrier concentration of 5×10^{16} cm^{-3}. In order to eliminate chemical interaction of the GaAs surface with atomic hydrogen, the samples were coated by a plasmachemical deposition method with a 5-nm-thick protective SiO_2 film. These samples were treated in a flow of atomic hydrogen in the same setup for 5 min at T = 200°C.

The flux containing both atomic and molecular hydrogen was formed by a source based on an arc reflection discharge gap with a hollow cathode and self-heating element [5]. The fraction of charged particles escaping from the output hole of the source did not exceed 10^{-4}% of the discharge current. The partial hydrogen pressure in the region of sample treatment was $p = 10^{-2}$ Pa. The fraction of hydrogen atoms in the flux (the concentration of atomic hydrogen in the gas phase) could be controlled by changing the discharge current.

A change in the atomic hydrogen concentration in the gas phase was determined by a method based on the optical spectroscopy of the gas discharge plasma and estimated by the intensity of the hydrogen line in the Balmer series. The amount of hydrogen penetrating into a vanadium film was evaluated by the change in the sample resistance in the course of hydrogenation. It was assumed that the relative change in the sample resistance in the initial hydrogenation stage (t = 1.5 min),

1063-7850/00/2610-0926$20.00 © 2000 MAIK "Nauka/Interperiodica"

where the hydrogen content in the metal is small, is proportional to the hydrogen concentration [1, 2]. In semiconductor samples, the hydrogen concentration in GaAs was evaluated by determining the concentration N_{pass} of a dopant passivated by atomic hydrogen. For this purpose, the concentration of the electrically active impurity at a depth of 250 nm was determined by the capacitance–voltage (C–U) technique before (N_0) and after (N) hydrogenation and the concentration of hydrogen–dopant complexes was calculated as $N_{pass} = N_0 - N$. It was assumed [6, 7] that N_{pass} is proportional to the total hydrogen concentration in GaAs.

Figure 1 shows the plots of the relative intensity $I(H_\beta)$ of the hydrogen β-line in the Balmer series and a relative change in the sample resistance $\Delta R/R_0$ (for the hydrogenation time t = 1.5 min) versus discharge current of the hydrogen source. As the discharge current is increased, $I(H_\beta)$ grows to indicate increasing concentration of atomic hydrogen in the gas discharge plasma and, hence, in the region of sample treatment. Note that the atomic hydrogen concentration increases despite a monotonic decrease in the discharge voltage accompanying the increase in the discharge current (Fig. 1a, curve *2*). This indicates that the growth in the rate of atomic hydrogen production (caused by increasing discharge current) markedly exceeds the drop in the hydrogen production rate related to the discharge voltage drop.

The growth in the partial pressure of atomic hydrogen in the gas phase leads to an increase in $\Delta R/R_0$, which is evidence that a growing amount of hydrogen atoms penetrate into the vanadium film (Fig. 1b). Thus, an increase in the concentration of atomic hydrogen in the gas phase is accompanied by a proportional growth in the flux of hydrogen penetrating into the metal. This result can be readily explained based on the mechanism of hydrogen atom incorporation into the lattice of transition metals [3]. Indeed, since the probability of hydrogen atoms entering the metal lattice is close to unity, the increase in the supply of these atoms to the vanadium film surface must naturally result in the proportional growth of the amount of hydrogen incorporated into the metal.

A different situation is observed for the SiO_2/GaAs samples treated with atomic hydrogen. Figure 2 shows the plot of the hydrogen–dopant complex concentration N_{pass} in GaAs versus the discharge current. As seen, an increase in the atomic hydrogen concentration in the gas phase leads to a monotonic decrease in the content of hydrogen bound in the complex, which is evidence of the corresponding decrease in the amount of hydrogen atoms incorporated into the SiO_2/GaAs sample. This result can be explained by assuming that the growth of discharge current is accompanied by a decrease in the probability of hydrogen atoms penetrating into the semiconductor structure. This decrease is so large that it cannot be compensated even by a growth in the concentration of atomic hydrogen in the gas phase.

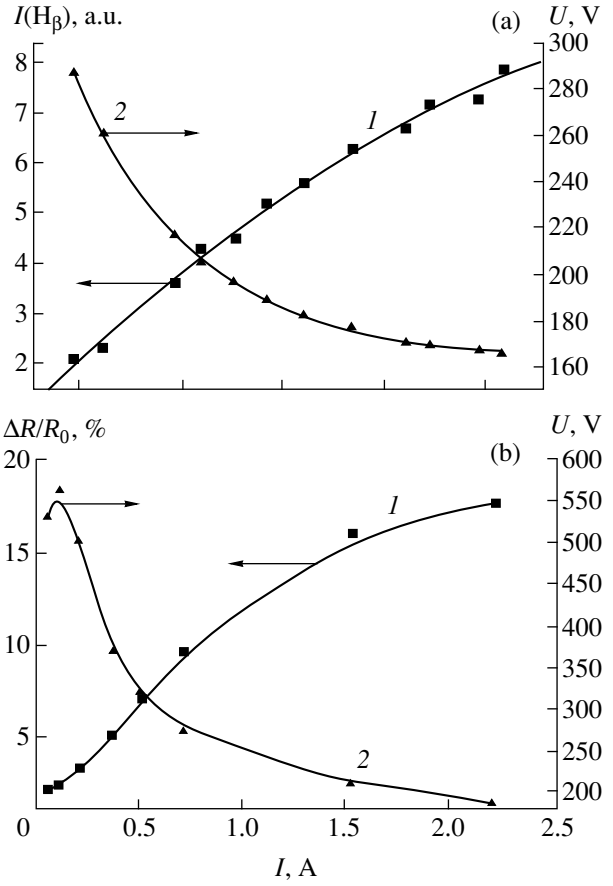

Fig. 1. Plots of (a) the relative intensity $I(H_\beta)$ of the hydrogen β-line in the Balmer series (curve *1*) and the discharge voltage U (curve *2*) and (b) the relative change in the sample resistance $\Delta R/R_0$ for the hydrogenation time t = 1.5 min (curve *1*) and the corresponding discharge voltage U (curve *2*) versus discharge current.

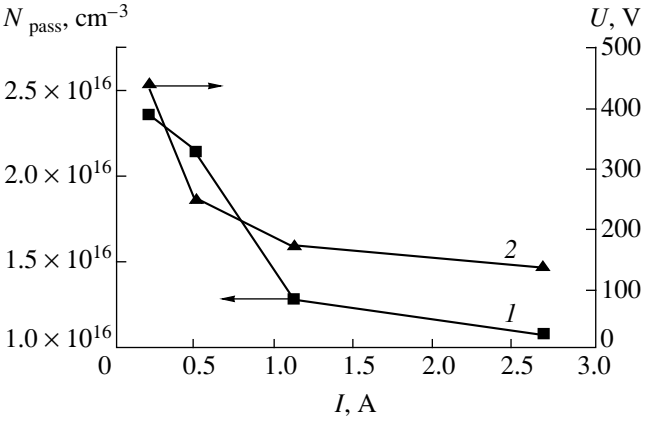

Fig. 2. Plots of (*1*) the hydrogen–dopant complex concentration N_{pass} in GaAs and (*2*) the discharge voltage U versus the discharge current.

We believe that the decrease in the probability of atomic hydrogen penetrating into the SiO_2/GaAs system can be related to a decrease in the energy of atoms leaving the discharge and reaching the sample surface. It was demonstrated [8] that the energy of hydrogen atoms in a gas discharge drops on decreasing the temperature of electrons producing dissociation of hydrogen molecules. It is also known [9] that the electron temperature in the discharge plasma decreases with decreasing discharge voltage. The plots of the discharge voltage versus discharge current presented in Figs. 1 and 2 (curves *2*) show that the voltage significantly decreases when the current is increased (this behavior is typical of the given form of discharge [5]). All these data indicate that the growth of the discharge current may be really accompanied by a decrease in the energy of hydrogen atoms produced by the source.

According to the results of measurements reported in [8, 10], the mean kinetic energy of atoms produced in an arc discharge in the gas phase by electron impact dissociation is $E = 0.2$–1.5 eV. Therefore, penetration of even the most energetic atoms ($E = 4$–8 eV [8, 10]) into the solid lattice cannot be considered as a direct implantation (or kinetic incorporation). The kinetic energy of hydrogen atoms produced in the discharge under these conditions is comparable with their potential (chemical) energy and, hence, may enhance the adsorption (increase the sticking coefficient) and/or facilitate overcoming the surface potential barrier and entering into the uppermost surface layers of SiO_2. Nor can we exclude that more energetic atoms ($E < 400$–150 eV) formed as a result of the ion recharge process, dissociative recombination, or ion neutralization upon reflection from the discharge gap walls [11], as well as ions (the energies of all these species being proportional to the discharge voltage) may affect the atomic hydrogen penetration process. Although the concentration of these species is lower by several order of magnitude than the concentration of low-energy hydrogen atoms, the energy delivered to the surface may be sufficient to stimulate the atomic hydrogen penetration into the SiO_2/GaAs system.

The obtained results can be also explained by the formation of a surface and/or subsurface diffusion barrier for the hydrogen atoms penetrating into the SiO_2/GaAs structure. This barrier may be composed, for example, of interstitial hydrogen molecules formed as a result of association of the diffusing hydrogen atoms. This barrier appears when the flux of atoms entering the system is so large that the rate of their association into molecules becomes sufficiently high to yield $\cong 10^{21}$–10^{22} cm^{-3} hydrogen molecules in a thin subsurface layer during the experiment. As a result, the interstitial positions in the lattice are occupied by immobile hydrogen molecules hindering the further surface penetration by atomic hydrogen arriving from the gas phase.

Acknowledgments. The authors are grateful to A.V. Kozyrev and A.A. Samartsev for fruitful discussions.

REFERENCES

1. *Hydrogen in Metals*, Ed. by G. Alefeld and J. Voekl (Springer-Verlag, New York, 1978; Mir, Moscow, 1981).
2. E. Fromm and E. Gebhardt, *Gase und Kohlenstoff in Metallen* (Springer-Verlag, Berlin, 1976; Metallurgiya, Moscow, 1980).
3. *Interaction of Hydrogen with Metals*, Ed. by A. P. Zakharov (Nauka, Moscow, 1987).
4. A. Y. Polyakov, N. B. Smirnov, A. A. Chelniy, *et al.*, Solid-State Electron. **38** (4), 771 (1995).
5. V. A. Kagadei and D. I. Proskurovsky, J. Vac. Sci. Technol. A **16** (4), 2556 (1998).
6. R. Morrow, J. Appl. Phys. **66** (7), 2973 (1989).
7. N. Watanabe, T. Nittono, I. Hirishi, *et al.*, J. Appl. Phys. **73** (12), 8146 (1993).
8. A. M. Bruneteau, G. Hollos, M. Bacal, and J. Bretagne, J. Appl. Phys. **67** (12), 7254 (1990).
9. Yu. P. Raĭzer, *The Physics of Gas Discharge* (Nauka, Moscow, 1987).
10. E. C. Samano, W. E. Carr, M. Siedl, and B. S. Lee, Rev. Sci. Instrum. **64** (10), 2746 (1993).
11. T. J. Sommerer and M. J. Kushner, J. Appl. Phys. **70** (3), 1240 (1991).

Translated by P. Pozdeev

Technical Physics Letters, Vol. 26, No. 10, 2000, pp. 929–931. Translated from Pis'ma v Zhurnal Tekhnicheskoĭ Fiziki, Vol. 26, No. 20, 2000, pp. 82–88.

Laser-induced Thermal Breakdown of a Semiconductor in the Presence of Mutually Correlated Noises

Yu. V. Gudyma

Chernovtsy State University, Chernovtsy, Ukraine

Received April 4, 2000

Abstract—The laser-induced thermal breakdown in a semiconductor plate under the joint action of an external multiplicative noise (laser radiation energy density fluctuations) correlated with an internal additive noise is studied theoretically. The correlated additive noise is demonstrated to increase the degree of bistability of the crystal temperature hysteresis. © *2000 MAIK "Nauka/Interperiodica".*

1. Laser-induced thermal breakdown exemplifies nonlinear phenomena in multistable systems without external feedback [1–3], where the stable states exist if the system parameters exceed certain critical levels. In semiconductors, the breakdown results from the exponential growth in the absorption of light by free charge carriers as the absorbed radiation heats the material (the photon energy being smaller than the energy bandgap). The effect is manifested by an avalanche-like rise in the semiconductor temperature beginning when the light intensity (an external parameter) is above the breakdown threshold. Since pulses produced by a continuously pumped laser follow at a limited repetition rate, the absorbed radiation energy intensity fluctuates from pulse to pulse [4]. According to the Lambert–Beer law, the light intensity is a multiplicative parameter. Also recall that the incident radiant flux intensity governs the deterministic nonequilibrium properties of the system. Consequently, the intensity fluctuations may well have a strong effect in the case under consideration. On the other hand, the essentially nonequilibrium character of the process leads to random fluctuations in the charge carrier velocity, manifested by additive noise in the thermal balance equation.

2. Consider a uniform semiconductor plate with a small Biot number $Bi = Hl/\lambda \ll 1$, where l is the plate thickness, λ is the thermal conductivity, and H is the heat transfer coefficient (equal to the ratio of the specific heat loss to the linear density of the material). The transverse thermal resistance of the plate is small compared with the thermal resistance of the contact between the plate and the heat bath (thermostat), so that the temperature becomes uniform across the plate thickness in a short time. Thus, a nonstationary thermal regime in the system can adequately be described by a single variable T representing the temperature averaged across the thickness of the plate. This variable can be found from the thermal balance equation

$$c\frac{dT}{dt} = G(x,t)\{1-\exp(-\alpha(T)l)\}/l - H(T-T_0), \quad (1)$$

where $G(x, t)$ is the intensity of the wide incident laser beam; c is the specific heat of the semiconductor; T_0 is the thermostat temperature;

$$\alpha(T) = \alpha_0\exp(-E_g/2kT) \quad (2)$$

is the optical absorption coefficient of free charge carriers; and E_g is the energy bandgap width.

Equation (1) can easily be rewritten in dimensionless variables with regard for the two types of noise mentioned above:

$$\frac{d\theta}{d\tau} = \beta(\tau)\{1-\exp[-\eta\exp(\gamma-\gamma/\theta)]\} - (\theta-1)+\gamma(\tau), \quad (3)$$

where

$$\theta = T/T_0, \quad \tau = tH/c, \quad \gamma = E_g/2kT_0,$$

$$\eta = \alpha(T_0)l, \quad \beta(\tau) = \beta+\xi(\tau), \quad \beta = cG/HT_0.$$

Below, we assume that the correlation times of the external multiplicative noise and the internal additive noise are negligibly small. Each noise can therefore be approximated by a zero-mean white Gaussian noise:

$$\langle\xi(t)\xi(t')\rangle = 2\sigma^2\delta(t-t'), \quad (4a)$$

$$\langle\gamma(t)\gamma(t')\rangle = 2\varepsilon^2\delta(t-t'), \quad (4b)$$

$$\langle\xi(t)\gamma(t')\rangle = 2\chi\sigma\varepsilon\delta(t-t'), \quad (4c)$$

where χ is the degree of the cross correlation between the multiplicative and the additive noise.

3. Since the Langevin stochastic equation (3) has a number of stationary solutions, we have to determine their probabilities.

This investigation is based on the pioneering study of Wu *et al.* [5], where an appropriate formalism and

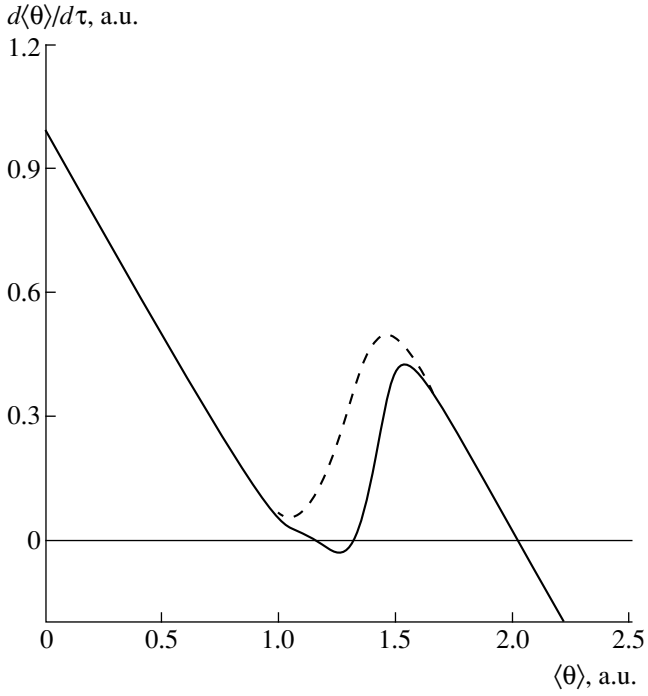

Fig. 1. Origination of a bistable temperature dependence under the action of a multiplicative noise ($\sigma = 0.2$).

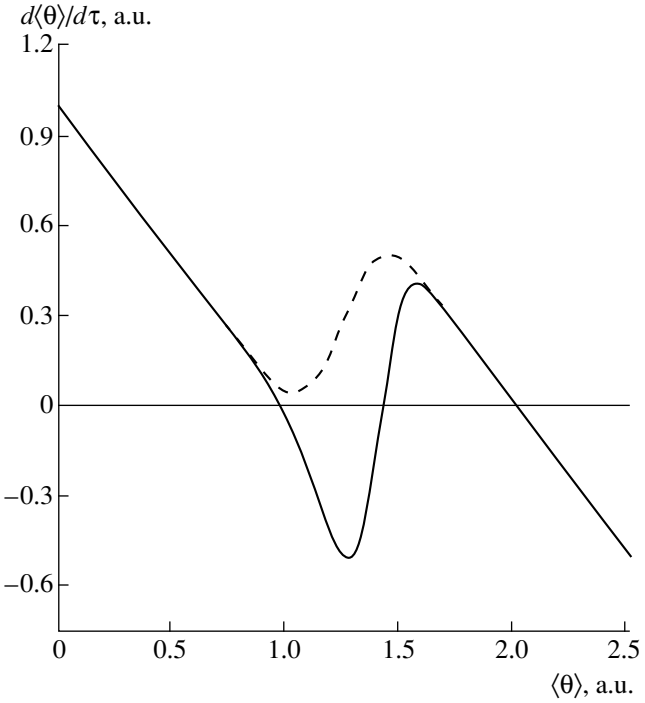

Fig. 2. Increase in the degree of system bistability under the correlated action of additive and multiplicative noise ($\sigma = 0.2$, $\varepsilon = 0.9$, $\chi = 0.9$).

basic relations for correlated noises were developed. Associated with Eq. (3) is the Fokker–Planck equation

$$\frac{\partial P(\theta,\tau)}{\partial\tau} = -\frac{\partial}{\partial\theta}A(\theta)P(\theta,\tau) + \frac{\partial^2}{\partial\theta^2}B(\theta)P(\theta,\tau), \quad (5)$$

where

$$A(\theta) = h(\theta) + G'(\theta)G(\theta), \quad (6a)$$

$$B(\theta) = [G(\theta)]^2 \quad (6b)$$

with

$$h(\theta) = \beta\{1 - \exp[-\eta\exp(\gamma - \gamma/\theta)]\} - (\theta - 1) \equiv \beta g(\theta) - (\theta - 1), \quad (7a)$$

$$G(\theta) = [\sigma g^2(\theta) + 2\chi\sigma\varepsilon g(\theta) + \varepsilon]^{1/2}. \quad (7b)$$

The stationary probability density function (pdf) obtained from Eq. (5) is

$$P_{st}(\theta) = NB^{-1}(\theta)\exp\left\{\int_0^\theta \frac{A(\theta')}{B(\theta')}d\theta'\right\}, \quad (8)$$

where N is a constant, which can be found from the normalization condition

$$\int_0^b P_{st}(\theta)d\theta = 1. \quad (9)$$

The upper limit of integration is dictated by physical restrictions (such as the melting point of the crystal).

The extrema of the stationary pdf are regarded as macroscopic stationary states of the system. Accordingly, an analysis of expression (8) leads to the transcendental equation

$$h(\theta) - \sigma g'(\theta)[g(\theta) + \chi\varepsilon] = 0, \quad (10)$$

whose roots determine the possible stationary states of the system. Indeed, note that the definition implies

$$P_{st}(\theta) = \delta(\theta - \langle\theta\rangle_{st}), \quad (11)$$

where

$$\langle\theta\rangle_{st} = \int_{-\infty}^{+\infty}\theta P_{st}(\theta)d\theta. \quad (12)$$

Expression (12) is simply a definition of the mean value. Averaging in Eq. (10) subject to (11) yields

$$h(\langle\theta\rangle_{st}) - \sigma g'(\langle\theta\rangle_{st})[g(\langle\theta\rangle_{st}) + \chi\varepsilon] = 0. \quad (13)$$

4. A numerical analysis of Eq. (13) was carried out for the case of a 6-mm-thick germanium plate irradiated by 10.6-μm continuously pumped CO_2 lasers, the corresponding parameter values being $\eta = 0.054$, $\gamma = 13$, and $\beta = 1$ [2]. Note that semiconductor plates serve as transparent components in far-infrared lasers. Their potential damage due to thermal breakdown sets a limit on the laser power; hence the interest in the problem under study [6, 7].

As is known, if a control (cooperative) parameter is below a critical level, a growth in a multiplicative noise may result in the reversible thermal breakdown of the semiconductor so that the temperature dependence exhibits hysteresis [8]. According to [9], a necessary condition for the temperature hysteresis is the existence of three stationary temperatures corresponding to two stable states and one unstable state of the system (Fig. 1). A number of new phenomena arise with an increasing level of the additive noise, which is correlated with laser-intensity fluctuations (Fig. 2). First, the low-temperature (ground) state of the bistable system moves toward lower temperatures. Second, the degree of system bistability goes up, the population probabilities of the stable states approaching each other. Consequently, the bistable system evolves from pronounced asymmetry toward symmetry. The times of spontaneous transitions between states become closer to each other.

This remarkable result of the bistability theory has the following implication for semiconductors. The stable stationary states represent the normal (stable) and the breakdown (metastable) states under reversible thermal breakdown conditions. The higher the level of an additive (thermal) noise correlated with the laser intensity fluctuations, the higher the probability of the breakdown state.

REFERENCES

1. V. L. Komolov, Izv. Ross. Akad. Nauk, Ser. Fiz. **61** (7), 1293 (1997).
2. É. M. Épshteĭn, Zh. Tekh. Fiz. **48** (8), 1733 (1978) [Sov. Phys. Tech. Phys. **23**, 983 (1978)].
3. N. N. Rozanov, Zh. Éksp. Teor. Fiz. **80** (1), 96 (1981) [Sov. Phys. JETP **53**, 47 (1981)].
4. E. V. Baklanov and A. K. Dmitriev, Kvantovaya Élektron. (Moscow) **29** (1), 35 (1999).
5. Wu Da-jin, Cao Li, and Ke Sheng-zhi, Phys. Rev. E **50** (4), 2496 (1994).
6. M. Lenzner, J. Krüger, S. Sartania, *et al.*, Phys. Rev. Lett. **80** (18), 4076 (1998).
7. M. Li, S. Menon, J. P. Nibarger, and G. N. Gibson, Phys. Rev. Lett. **82** (11), 2394 (1999).
8. Yu. V. Gudyma, Zh. Tekh. Fiz. **67** (9), 117 (1997) [Tech. Phys. **42**, 1088 (1997)].
9. N. N. Rozanov, *Optical Bistability and Hysteresis in Distributed Nonlinear Systems* (Nauka, Moscow, 1997).

Translated by A. Sharshakov

Technical Physics Letters, Vol. 26, No. 10, 2000, pp. 932–934. Translated from Pis'ma v Zhurnal Tekhnicheskoĭ Fiziki, Vol. 26, No. 20, 2000, pp. 89–94.

Coherent Oscillations Excited in Opposite Electron and Ion Beams of a Diaphragmed Discharge between Hollow Electrodes

A. E. Dubinov, E. E. Dubinov, V. S. Zhdanov, Yu. N. Lashmanov, I. L. L'vov, K. E. Mikheev, S. A. Sadovoĭ, V. D. Selemir, and A. V. Tsarev

Russian Federal Nuclear Center, All-Russia Research Institute of Experimental Physics, Sarov, Russia

e-mail: dubinov@ntc.vniief.ru

Received May 11, 2000

Abstract—We have experimentally studied the coherence of oscillations appearing, as a result of the Buneman instability, in a stationary regime of a diaphragmed discharge between hollow electrodes. The degree of coherence of the oscillations grows with the discharge current intensity, which is probably explained by an electrostatic coupling between discharge channels increasing with the amplitude of oscillations. © *2000 MAIK "Nauka/Interperiodica".*

Diaphragmed discharge gaps with hollow cathode and anode are extensively studied and widely employed. The applications include pseudospark dischargers [1], sources of visible and UV radiation [2], dense plasma jet generators [3], etc. The diaphragmed discharge phenomenon can be also used for the production of beams of charged particles, i.e., positive ions and electrons [4–6]. These beams, formed in the region of the diaphragm, may carry rather large current densities.

As is known, oppositely directed electron and ion beams with large current densities are subject to various instabilities, the majority of which can be of the Buneman type. As a rule, instabilities of this type lead either to attaining a saturation stage (featuring coherent oscillations manifested by a regular modulation of the electron beam) or to the development of a strongly turbulent state in the electron–ion plasma (without significant coherence).

The purpose of this work was to study the effect of the discharge current intensity on the degree of coherence of the oscillations appearing as a result of the Buneman instability development.

In order to study the collective processes taking place in the region of the diaphragm, we have designed and constructed a special spherical discharge chamber schematically depicted in Fig. 1. The device comprises two hemispherical steel electrodes with a diameter of 200 mm. The electrodes are separated by a flat caprolon insulator with a high-temperature ceramic cylindrical diaphragm with a diameter of 7 mm and a length of 10 mm, arranged at the center of the insulator.

A dc discharge was initiated in the chamber at a residual air pressure of P = 0.1–0.01 Torr and maintained in a stationary regime, whereby the discharge current acquired a value within the range I_{dis} = 100–250 mA and remained constant to within ±5 mA.

Operating in a stationary regime, the discharge generated intense oscillations in a range of frequencies from 0.2 to 2 MHz that could be detected by point filament probes situated in the vicinity of the diaphragm. The amplitude of oscillations was found to increase with the discharge current. It was established that oscillations appear as soon as the current density in the diaphragm exceeds a certain threshold level. An analysis of the measured threshold current densities and characteristic oscillation frequencies showed that the oscillations are due to the Buneman instability development.

The degree of coherence of the oscillations was determined by the following method. The diaphragm was divided into two parts by a 1-mm-thick longitudinal dielectric spacer, so that the two channels were insulated with respect to the fluxes of plasma particles but still coupled with respect to the microwave electric field (Fig. 1). Identical filament probes were placed into each channel, their measuring circuits being synchronized to within 40 ns. The signals from the probes were transmitted to a two-channel digital oscillograph and registered with a discretization time step of 40 ns to accumulate a data array of 10^4 points.

The pair of signals measured in this system was processed to calculate the signal coherence function $\gamma(f)$ of the frequency f according to the formula [7, 8]

$$\gamma(f) = \frac{C_{12}^2(f)}{C_{11}(f)C_{22}(f)}, \quad (1)$$

where $C_{ij}(f)$ is the autocorrelation function of the signals for $i = j$ and the mutual correlation function for $i \neq j$. Note that $0 \leq |\gamma(f)| \leq 1$, and the fact that the coher-

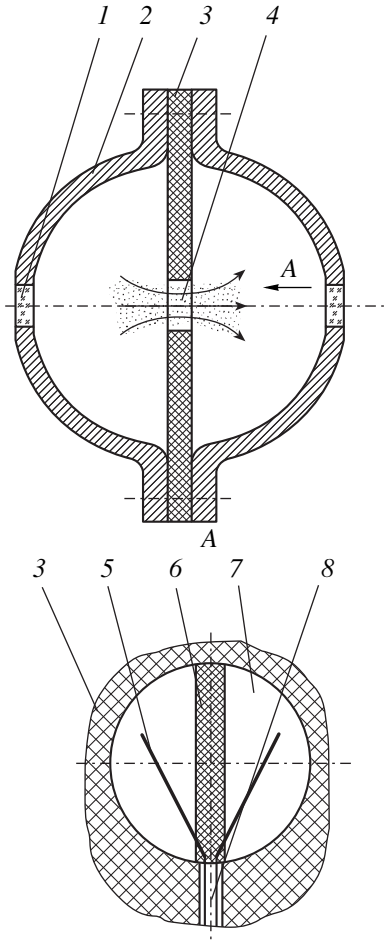

Fig. 1. Schematic diagrams of the discharge chamber and the diaphragm cross section: (*1*) observation window; (*2*) hemispherical electrodes; (*3*) insulating plate; (*4*) ceramic diaphragm; (*5*) filament probes; (*6*) insulating spacer; (*7*) plasma channel; (*8*) vacuum-tight feedthrough for the probes. Arrows indicate the directions of electron motion in the discharge plasma.

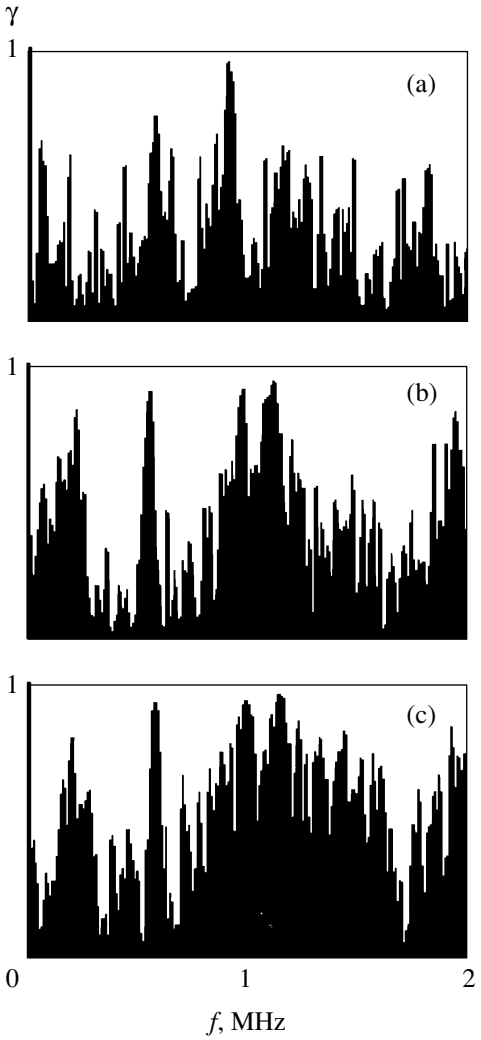

Fig. 2. Typical signal correlation functions $\gamma(f)$ measured at various discharge currents I_{dis} = 100 (a); 170 (b); 250 mA (c).

ence function at a given frequency is close to unity implies that the corresponding spectral components of the signals are synchronized and coherent. Should the coherence function be close to zero, the corresponding components are independent.

The degree of coherence in a frequency interval from f_0 to $f_0 + \Delta f$ can be quantitatively characterized by the quantity

$$\Theta = \frac{1}{\Delta f} \int_{f_0}^{f_0 + \Delta f} \gamma(f) df. \qquad (2)$$

Let us consider the results of measurements in the discharge operating at a gas pressure of $P = 0.1$ Torr.

Figure 2 shows the signal coherence functions $\gamma(f)$ calculated for various discharge currents I_{dis}. As can be seen, the degree of coherence of the oscillations grows with the I_{dis} value.

We have also evaluated the degree of coherence in the frequency range $(f_0–f_0 + \Delta f) = 0–2$ MHz by formula (2). The results of these calculations are presented in Fig. 3, where the horizontal error bars correspond to the accuracy of discharge current measurements and the vertical bars represent the statistical scatter in a set of time realizations for signal pairs measured and processed at each point. The data in Fig. 3 unambiguously confirm that an increase in the discharge current is accompanied by growing synchronization of the plasma oscillations in the frequency range studied. This can be explained by the electric interaction between discharge channels in the diaphragm increasing with the oscillation amplitude.

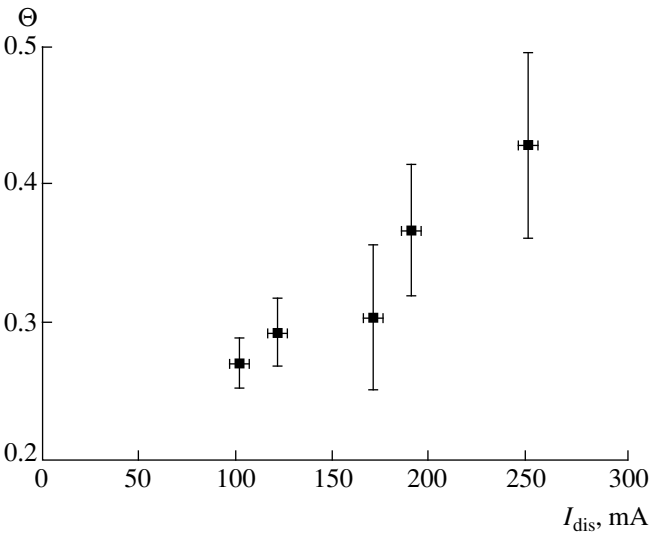

Fig. 3. A plot of the degree of correlation Θ versus discharge current I_{dis}.

Thus, we have demonstrated that a growth in the discharge current leads to increase in the degree of coherence between the discharge channels.

REFERENCES

1. R. Tkotz, A. Görtler, J. Christiansen, *et al.*, IEEE Trans. Plasma Sci. **23** (3), 309 (1995).
2. M. F. Danilov and E. V. Kalashnikov, Teplofiz. Vys. Temp. **33** (5), 663 (1995).
3. E. V. Kalashnikov, Teplofiz. Vys. Temp. **33** (3), 339 (1995).
4. L. C. Pitchford, IEEE Trans. Plasma Sci. **23** (3), 243 (1995).
5. J. Westheide, IEEE Trans. Plasma Sci. **23** (3), 254 (1995).
6. R. Stark, J. Christiansen, K. Frank, *et al.*, IEEE Trans. Plasma Sci. **23** (3), 258 (1995).
7. J. S. Bendat and A. G. Piersol, *Engineering Applications of Correlation and Spectral Analysis* (Wiley, New York, 1980; Mir, Moscow, 1983).
8. G. C. Carter, Proc. IEEE **75** (2), 236 (1987).

Translated by P. Pozdeev